STUDY OF DROPLET DYNAMICS IN TRANSCRITICAL ENVIRONMENTS

R. Raman

Supervisors
Prof. Stefan Hickel
Mr. Mohamad Fathi, M.Sc
Department of Aerospace Engineering
Delft University of Technology

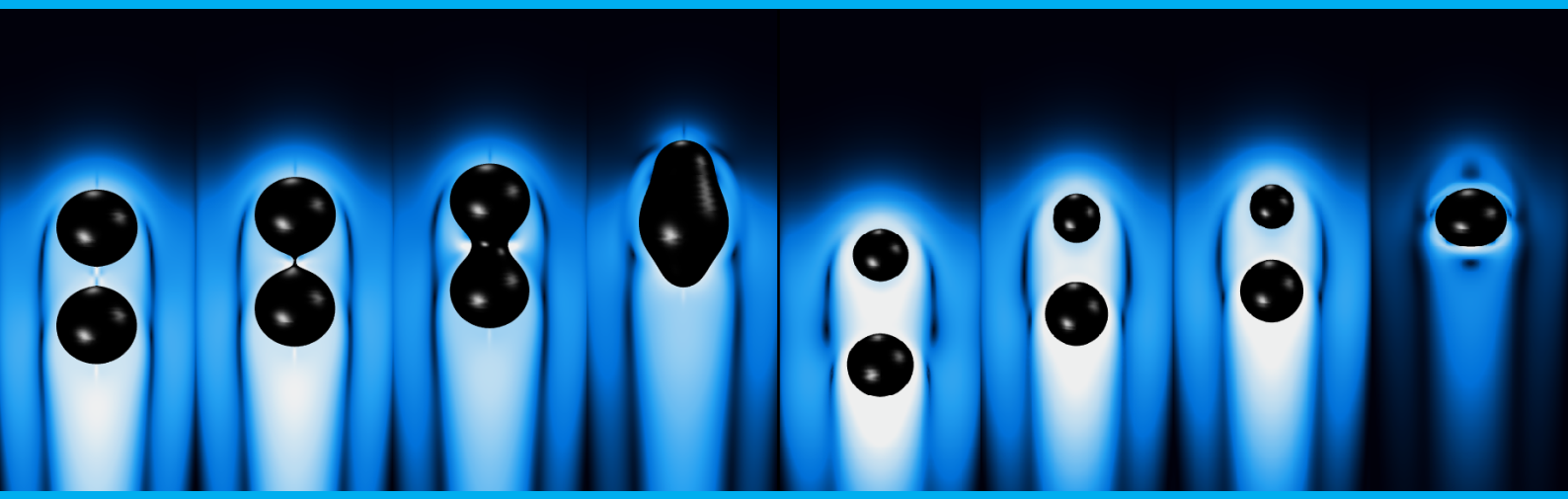

TU Delft

STUDY OF DROPLET DYNAMICS IN TRANSCRITICAL ENVIRONMENTS

by

R. Raman

for partial requirement to obtain the degree of Master of Science
at the Delft University of Technology,
to be defended publicly on Monday March 22, 2021.

Student number: 4718526

Thesis committee:	Prof. dr. Stefan Hickel,	TU Delft, supervisor
	Ir. Mohamad Fathi,	TU Delft, daily supervisor
	Prof. dr. D.J.E.M Roekaerts,	TU Delft
	Dr. Steven Hulshoff,	TU Delft

An electronic version of this thesis is available at `http://repository.tudelft.nl/`.

Cover picture: From left to right, oil droplets in water using level-set (figure 1- 4) and phase-field methods (figure 5-8)

TU Delft

Preface

I would like to place it on record that it would be near to impossible to complete the course without the constant support of my friend Rayaru. I would also like to place my heartfelt gratitude to my supervisor Prof. Hickel and Mr. Fathi, for their constant support, guidance throughout the process of the thesis, and, more importantly to for permitting me to work on this amazing topic. Also, special thanks to late Prof. R.B. Bird for helping me with the basics of diffusivities. Special thanks to my graduation committee for being a part of the committee during these extraordinary circumstances. Preface would be not justified if I don't thank Praveen and Sid from the bottom of my heart for all the support and dinners, which helped me to take some work off my plate :). To Naveen for all the weekend trips, doses of reality check and so-called philosophical discussions ranging from Nietzsche to Buddha. Finally, sincere thanks to Vishnu, Seshsashayee, and Rahul for all the updates and support from India.
Once again, this entire three odd years would be too insipid if not for you guys...

My heartfelt thanks to Ms. Jamali Asma for helping me out with the PC-SAFT and Dr. Ian, for the substantial help with thermal conductivity computation. Also, to my flat-mates, Ir. Sandhya, Ir. Vidhya, and Ir. Anshula for tolerating my nonsensical blabbering. Preface will be incomplete if I don't thank Dr. Bellan, Dr. Sazhin, Dr. Sun, Dr. Lamanna, Dr. Helena Nowakowska, Prof. Mauri, Dr. Cyril and COMSOL support team for their immense help during the work. Finally, Sampath and Athreya for all the help and support in all the "group works". In closing, the eyacha naigal namely Ir. Manoj, Ir. Arvind, Ir. Aravind, Ir. Mano, and Ir. Karishma for no particular reason :). This journey wouldn't be possible without the moral and financial backing of my dad, mom, sister, brother-in-law, and my dear nephews Vishak and Harish. Also, for believing that I would graduate one day :).

Finally, I would like to dedicate this thesis to Parabrahman, kanchi periyava, Muthumari Amman and Shevapet Kaliamman.

र्वधर्मान् परित्यज्य मामेकं शरणं व्रज ।
अहं त्वां सर्वपापेभ्यो मोक्षयिष्यामि मा शुचः ॥ ६६ ॥

R. Raman
Delft, March 2021

Abstract

EFFICIENT combustion processes are indispensable in limiting the temperature increase to 1.5° C as set by Intergovernmental Panel on Climate Change (IPCC) before 2030 to curtail the effects of global warming. As for the emissions, the main task lies in controlling the air-fuel ratio in the lean regime as to control the emissions of NO_x since they reach maximum discharge at the stoichiometric ratio whereas improper mixing can lead to an increase in CO emissions. Thus, the air and fuel interactions need to be studied to achieve control over emissions. To that end, good computational models are necessary to supplement the design process to control both the emissions and combustion instabilities. The latter can severely damage the combustion chamber. Therefore, the proper modeling of the fuel-air interfaces in high-pressures is pivotal as they differ significantly from the low-pressure injection.

Various numerical droplet evaporation models are studied in trans/supercritical environments, the fluid is called supercritical when its above the critical states whereas it is called transcritical when it passes the critical state. As for the droplets, two components were selected namely n-heptane and n-dodecane. The former for 0-D and 1-D models and the latter for 3-D models, the cases were dictated by the availability of experimental works. As for the 0-D and 1-D models, various correlations based on the Nusselt and Sherwood numbers were utilized. The Prandtl number and other non-dimensional numbers were computed by thermophysical property models based on the 1/3 rd rule rather than fixed values. In comparison, the developed 0-D and 1-D models conform to the experimental results and other computational studies ranging from perfect-gas to real-gas against the experimental work available in the literature. It is hypothesized that the differences in the computation of the latent heat of vaporization are more pronounced in the accuracy of the lifetime of the droplet rather than the density of the components.

In 3-D models, the liquid-vapor interface is modeled by level-set and phase-field methods. Thermodynamic closure is achieved by the Peng- Robinson equation of state. Prandtl number assumption model is invoked for the computation of the liquid thermal conductivity, Chung model for the calculation of viscosity of mixtures, and Firoozabadi model for the Maxwell-Stefan diffusion coefficient. A basic model is used for the computation of surface tension coefficient for the phase-field 3-D models. A qualitative agreement was observed between the 3D model under this study, numerical work and the experimental campaign of microscopic droplets for all the three vaporization regimes namely classical, translational and diffusive mixing. All the models yielded olive-shaped droplets. Effects of mesh resolution on the phase-field quantities were studied and contrasted with the same mesh size for the level set method in a 2-D configuration. Recommendations include better surface tension models, thermal conductivity for gaseous mixtures , the inclusion of PC-SAFT equation of state, cross-diffusion terms, and high mesh resolution of the O(-7) m in the droplet region coupled with adaptive meshing based on the gradient of the phase-field parameter.

Contents

List of Figures

List of Tables

Nomenclature

List of Abbreviations

Gr	Grasshof number
Nu	Nusselt number
Pr	Prandtl number
Re	Reynolds number
Sc	Schmidt number
Sh	Sherwood number

List of Acronyms

CSP	Corresponding States Principle
DIM	Diffuse Interface Methods
ECS	Extended Corresponding States
EoS	Equation of state
LBC	Lohrenz–Bray–Clark
LSM	Level Set Method
NSAC	Navier Stokes Allen Cahn
NSCH	Navier Stokes Cahn Hilliard
NSK	Navier Stokes Korteweg
PC-SAFT	Pertubed Chain - Statistical Associating Fluid Theory
PFM	Phase Field Methods
PR	Peng–Robinson
RK	Redlich-Kwong
SRK	Soave-Redlich-Kwong

List of Symbols

η	Viscosity
λ	Thermal conductivity
μ	Chemical potential
ω	Acentric factor
ρ	Density
σ	Surface tension coefficient
χ	Mobility tunning parameter

P	Pressure
T	Temperature

Subscripts

0	ideal contributions
c	Critical
cm	Mixtures critical properties
$disp$	Dispersion
ex	Excess
hc	Hard chain
l	Liquid
r	Reduced
ref	Reference
v	Vapor

1 Introduction

1.1. What is transcritical vaporization?

A process is termed as supercritical when its pressure and temperature are higher than the critical pressure P_c and temperature T_c of the component. It is termed as transcritical when it crosses subcritical to supercritical state. Vaporization in itself is a very transient process determining the air-fuel mixing in conventional combustors by aerodynamic shearing but as the operating pressure increases there is a paradigm shift in the physics governing the vaporization. Compressed liquids lose their identity at very high temperatures and pressures comparable to the operating conditions of a liquid rocket engine i.e. they have properties of both liquids and gases e.g. density is comparable to the liquids and the diffusivity comparable to the gases as evidenced in the fig.1.1. These phenomena occurs because the fluid has enough energy to escape the potential well of the neighboring particles. The critical pressure is the vapor pressure at the critical temperature. Surface tension plays no significant role in droplet shearing at trans/supercritical conditions as seen in the fig.1.2.

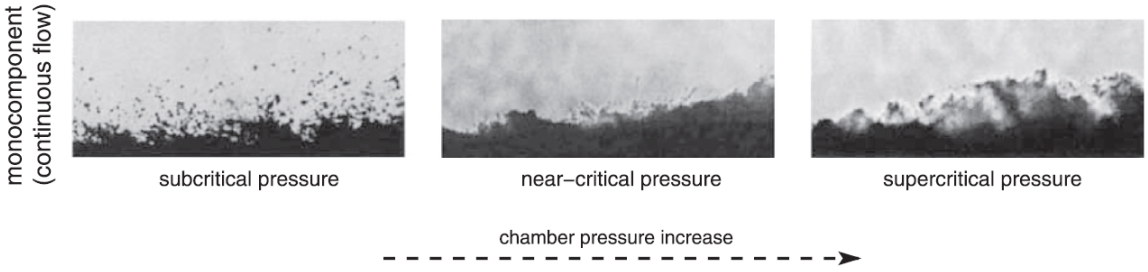

Figure 1.1: From left to right: Subcritical to supercritical states of nitrogen in its own vapour taken from Jofre and Urzay [2021]

1.2. Background

1.2.1. Real gas thermodynamics

There are no rigours definitions for the characterization of the supercritical state (Banuti et al. [2017]). It is commonly accepted that when the fluid has crossed both the critical temperature or critical pressure, it is called supercritical (Oefelein [2006]). Flows are categorized as transcritical when the temperature and pressure are lower and higher than their respective critical values. Transcritical and supercritical flows are the cornerstones for the implementation of the next generation of launchers and gas turbines. Supercritical flows are straightforward to model compared to the transcritical flows because of the single phase of the fluids. The main difficulty with simulating the transcritical flows is the transition where the properties become highly non-linear. Modeling of transcritical flows require real gas thermodynamics for the thermo-physical properties. In this work, an effort has been made to address this highly non-linear section by using a sophisticated Equation of States (EoS) such as Perturbed Chain - Statistical Associating Fluid Theory (PC-SAFT) and the cubic EoS.

In this study, two class of equations of states are employed. They are,

- Cubic EoS
- PC-SAFT EoS

Cubic EoS primarily consists of Redlich-Kwong (RK), Soave-Redlich-Kwong (SRK) and Peng Robinson (PR) EoS. SRK and PR both stems from RK (Elhawwari [2020]). Although, PR- EoS is similar to SRK- EoS in terms of the structure, PR-EoS performs better at the prediction of density at high pressures. SRK seems to perform better in terms of stability for VLE computations. PC-SAFT is one of the modern equations of state where the statistical mechanics, along with molecular physics, are employed to determine the Helmholtz energy, which in turn is used to obtain other properties. RK, SRK, PR, and PC-SAFT-EoS are described in detail in the third chapter.

1.2.2. Phase-field methods

In the study of multi-phase systems, there are two classes of models.

- Sharp interface methods
- Diffuse interface methods

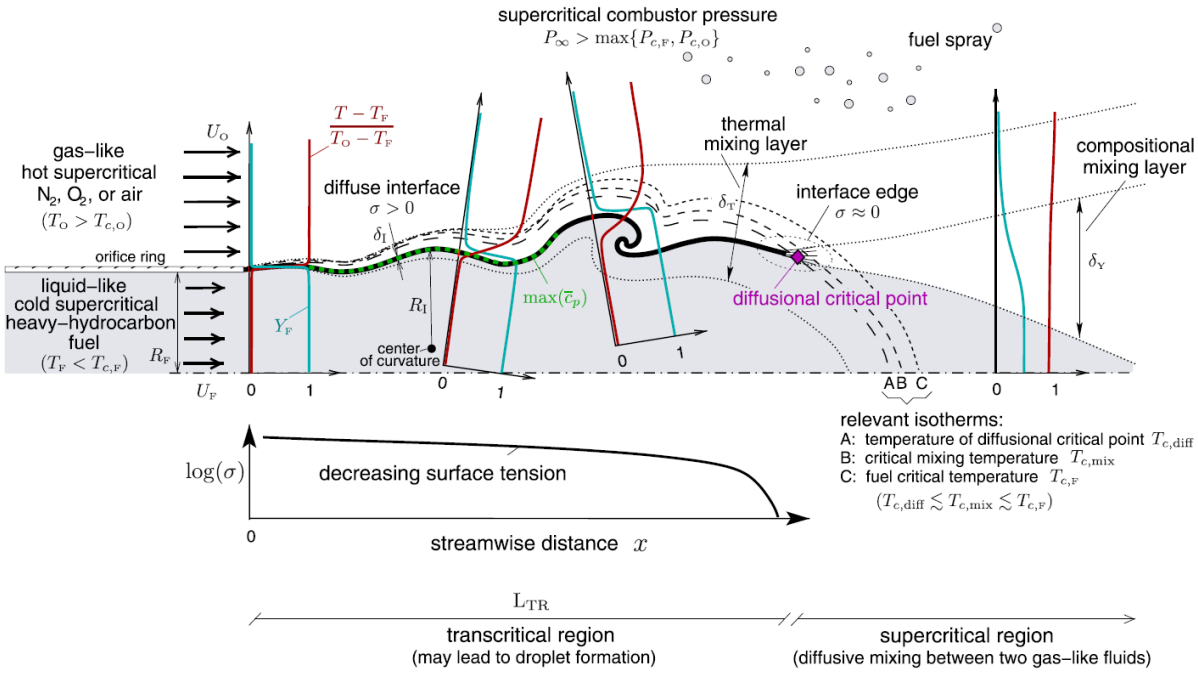

Figure 1.2: Pictorial representation of liquid stream in a high-pressure combustion chamber taken from Jofre and Urzay [2021]

As the name suggests, the sharp interface methods model the interface with zero thickness. In the conventional sharp interface methods, equations are solved for each phase, and the boundary conditions are imposed as jump conditions.

It is essential to distinguish the term diffuse interface models, conventionally it refers to the process of smearing/smoothing of the sharp interfaces, e.g., hyperbolic tangent level set (Moghadam et al. [2016]) or Baer-Nunziato (BN) mixture model (Baer and Nunziato [1986] and Saurel and Pantano [2018]). On the contrary, phase-field methods refers to a physically consistent method stemming from thermodynamics. van der Waals was the major proponent of the phase-field models where he concluded that when a component is tending to critical point from the lower environments the interface thickness becomes infinity (van der Waals [1893]). Hence, van der Waals suggested that the interfaces should also be described by non-local variables via the gradients of the variables. i.e.,

$$F = F^0(\rho, T) + F^{non}(\nabla\rho) \tag{1.1}$$

Where F^0 and F^{non} are the classical Helmholtz free energy and the non-local Helmholtz energy. In the above example, density is used as an order parameter.

The main distinguishing feature of the phase-field model compared to the sharp interface method is the definition of the order parameter. The order parameter is a scalar function which distinguishes the phases such that it experiences a rapid but continuous variations in the interface but a constant value in the bulk phases. Generally, for a single compressible component system, ρ can be used as an order parameter, while for binary mixtures, the mass/ molar fraction of one of the species is more suited.
Diffuse interface methods can be broadly classified into two types,

- Phase-field methods
- Numerically smeared interface e.g. mixture averaged models based on BN model

Phase-field methods are attracting a lot of attention due to their physical significance at the critical point. The other advantage of the phase-field methods is that interfaces are defined implicitly. As the system reaches the critical point from the lower limit, the interface thickness becomes of the same order of the bulk phases. Hence, it is imperative to consider an interface as a continuously varying region.
The significant divisions of phase-field methods are,

- Navier Stokes Cahn Hilliard equation (NCSH)
- Navier Stokes Korteweg equation (NSK)
- Navier Stokes Allen Cahn equation (NSAC)

In NSK, density is the order parameter and therefore there is no separate transport equation for the order parameter and the non-local interactions are reflected in the momentum equation. In NSCH, any relation can be used as the order parameter with the 4^{th} order Cahn-Hillard partial differential equation as the transport equation for the same. In NSAC, the 2^{nd} order Allen-Cahn partial differential equation is used as the transport equation for the order parameter. The other notable methods are, Density Functional Theory (DFT) and Density Gradient Theory (DGT) for modeling the interfaces. DGT is a version of DFT (via private communication to Prof. Shuyu Sun, KAUST).

BN model solves for each phase one momentum conservation, one mass conservation, one energy conservation, and finally one evolution equation for the volume fraction of the phase. The advantage of this model is that these classes of models don't require very fine grids for the simulation of the interface as opposed to the other models where they need a mesh size in the order of the interface width. In this category, they use a color function to capture the interface, and required physics can be added. A lot of work has been done regarding the applicability of the BN model to different systems. The striking characteristic of the BN method is that it allows the liquid and vapor phases to have different velocities, chemical potentials, and temperatures through relaxation terms. As for the numerical implementation, the pressure and temperature of the next iteration is chosen such that the difference between liquid and vapor fugacities is minimum.

1.3. Research questions

This work focuses on modeling of droplet vaporization in transcritical conditions. The vaporization at transcritical conditions has different facets such as,

1. Computation of the thermodynamic and derived thermodynamic properties
2. Computation of transport properties
3. Modeling of the interfacial dynamics

At the transcritical conditions, the thermo-physical properties are highly non-linear; therefore, robust models are required to model the dynamics. Hence in this work, few questions were addressed,

1. Which EoS is suitable for the conditions of interest? As a robust EoS is mandatory to capture the discontinuities during the transition and also to predict the properties such as density with minimal deviation.

2. Which transport property model can model the required property with permissible deviations? All transport property models have their basis in the kinetic theory but in the conditions of interest, mixing of dense fluids, there is a lack of transport property models for the conditions of interest.

3. How to realize the interfacial dynamics using level set and phase-field methods?

1.4. Outline of the report

This report is divided into nine chapters. Chapter 2 presents the literature review on the topic. In chapter 2, the literature review is presented on the various issues ranging from numerical modeling of transcritical flows to diffuse interface methods and at last the novelty of this work is discussed. In Chapter 3, the theory and performance of various EoS are discussed. Chapter 4 deals with the transport property models in the conditions of interest. Chapter 6 illustrates the performance of 0D models. Chapter 7 deals with 1D evaporation models with and without the classical Nusselt (Nu), and Sherwood (Sh) correlations. Chapter 8 deals with the modeling of droplets in 3D configuration. Finally, a summary and conclusion are presented in Chapter 9.

2

Literature review

2.1. Transcritical and supercritical combustion

Recently, the study of transcritical and supercritical combustion has received a lot of attention because of the need for fuel-efficient combustion systems. Matheis and Hickel [2016, 2018] developed a numerical framework for Eulerian large eddy simulation in transcritical and supercritical combustion. Comparisons between the conservative equations and quasi-conservative equations were made, the distinction being made by the conservation of the energy wherein the internal energy is replaced by the pressure evolution term in the quasi-conservative system. The work concluded that further research needs to be done with a sophisticated equation of state to improve the prediction of the liquid densities due to its pronounced effect of using a cubic equation of state. Also, the chemical reactions should be considered in the chemical sources in the conservation equations.

Banuti et al. [2017] studied the properties of supercritical fluids using molecular dynamics simulations. They observed that even after the fluid transients to a supercritical state, it is possible to distinguish gas-like and liquid-like states. This work helps in determining a genuinely supercritical state as a lot of definitions are available,

- Above either the critical temperature/ pressure or both
- Above the critical temperature

They characterized the transition line as the extension of the coexistence line, which is given by the maxima in the isothermal compressibility. If the fluid has passed the line, it is called a gas-like region else liquid-like region. From the density plots, they inferred that at low temperatures, the effect of pressure reduces, and it converges to the liquid state values. They proved that it is entirely within the realm of physics for a fluid to be supercritical and ideal concurrently. Therefore, it was concluded that supercritical fluids could be categorized as ideal gas if $T > 2T_{cr}$ and $p < 3p_{cr}$ (as seen in figure 2.1). Furthermore, they addressed various questions in properties of supercritical fluids such as differences between a liquid and a transcritical fluid, sensitivity to the changes in pressure and temperature, latent heat of vaporization and finally the necessity of pure fluid behaviours for combustion.

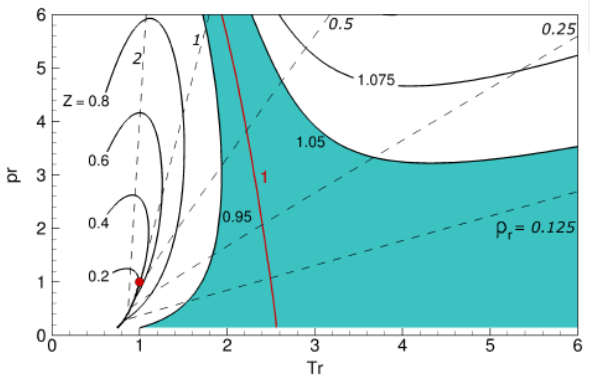

Figure 2.1: Z for various reduced conditions, shaded area includes 5% of deviations from the ideal gas (Z =1) Banuti et al. [2017]

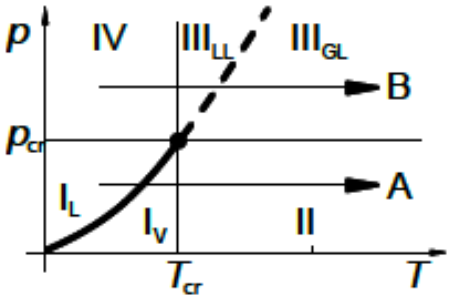

Figure 2.2: State diagram with pseudo-boiling line(dashed), LL and GL corresponds to liquid-like and gas-like, from Banuti et al. [2017]

The work on reacting transcritical flow modeling by Ma et al. [2017] used the classical Flamelet Progress Variable (FPV) to simulate the transcritical combustion. FPV uses the progress variable to compute from the previously calculated tables. They emphasized on the fact that the conventional look-up based on the mixture fraction and the variance are deficient in describing the state of the flames. This assumption particularly holds for the lifted flames, which have been consistently noted for high-pressure combustion systems. The Flamelet Progress Variable is a promising approach for transcritical and supercritical combustion systems. The authors used finite volume, fully compressible, explicit solvers, with particular reference to the pressure and temperature departures from the baseline configuration in a thermodynamically consistent manner. They used PR-EoS for the thermodynamic closure of the conservative equations. To compute the viscosity and the thermal conductivity, they employed Chung's high-pressure method but with a limitation of neglecting the negative acentric factors during the computation of the viscosity to avoid the numerical instability for multi-species. They discussed in detail the applicability of laminar flamelet combustion models for supercritical combustion. As observed in the supercritical combustion, a large Damkohler number indicates that the reaction region is laminar, and the diffusive transport equations are only relevant in the normal direction of the flame. They implemented the flamelet equations for counter-flow diffusion flames with modifications to ensure that the PR- EoS is consistently implemented in the flamelet equations. They also stressed on the importance of capturing the Pseudo-Boiling Point(PBP) since it is important for computing the real-gas properties from the ideal gas flamelet table, if not the peak in specific heat will be missed. Finally, they simulated the mixing case and the reacting case of `LOX/GH2`. They modeled with the following assumptions,

- The specific heat ratio is assumed as a constant to reduce the computational burden.
- Composition is the weak function of the reference conditions.
- The SGS terms for the cubic EoS are negligible.

They compared their results with AVBP and RAPTOR from the work of Ruiz et al. [2016].

Following this, the pioneering work of Cruanyes and Urzay [2016] is studied. This work is pioneering as previously not much importance was given to the description of the Navier-Stokes equations. They discussed the need for high-pressure combustion systems due to the demand for minimization of CO emissions and to increase the engine power. Unfortunately, in transcritical combustion, there is a paradigm shift of the physics governing the system. They emphasized the fundamental problems such as liquid breakup, dispersion, and vaporization. At the supercritical conditions, the liquid to gas density ratio increases, which causes the gas density to increase, and subsequently, the interface thickens due to the phenomena of liquid obtaining heat from the combustor environment. The significant change occurring during the supercritical combustion is the very low surface tension. They formulated the governing equations for transcritical equations based on the Navier-Stokes-Korteweg (NSK) model. They derived the conservation equations with terms from diffuse interface theory,

$$\frac{\partial \rho}{\partial t} + \nabla \cdot (\rho \mathbf{v}) = 0 \tag{2.1}$$

$$\frac{\partial \rho \mathbf{v}}{\partial t} + \nabla \cdot (\rho \mathbf{v} \otimes \mathbf{v}) = -\nabla \mathrm{P}_{NL} + \nabla \cdot (\tau + \mathscr{K}) \tag{2.2}$$

$$\frac{\partial \rho \mathrm{Y}_i}{\partial t} + \nabla \cdot (\rho \mathbf{v} \mathbf{Y}_i) = -\nabla \cdot (\mathbf{J}_i + \mathbf{J}_i) \tag{2.3}$$

$$\frac{\partial \rho E}{\partial t} + \nabla \cdot (\rho \mathbf{v} E) = -\nabla \cdot (\mathrm{P}_{NL} \mathbf{v}) - \nabla \cdot (\mathbf{q} + \mathscr{Q}) + \nabla \cdot [(\tau + \mathscr{K}) \cdot \mathbf{v}] \tag{2.4}$$

also, the non-local thermodynamic pressure used above is defined as,

$$P_{NL} = P - \frac{1}{2} \sum_{i=1}^{N} \sum_{j=1}^{N} \kappa_{ij} \nabla \rho_i \nabla \rho_j \tag{2.5}$$

The above set of equations describes the physics of a multi-phase, multi-component fluid of N species where ρ is the local density, E is total energy, $\mathbf{v}$ is the velocity of the system, Y_i is the mass fraction of the species i. The other terms τ, $\mathbf{q}$, $\mathbf{J}_i$ corresponds to the deviatoric stress tensor, heat, and species diffusion fluxes with $\mathscr{K}$, $\mathscr{Q}$, $\mathscr{J}_i$ as the corresponding terms stemming from the diffuse interface theory. They neglected the chemical source terms in this study as reactions are located spatially far from the interfaces. Finally, they closed the equations for the terms τ, $\mathscr{K}$, $\mathbf{q}_c$, $\mathscr{Q}$, $\mathbf{J}_i$, and $\mathscr{J}_i$ by specifying entropy production should be non-negative. It is important to note that the number of couplings between different fluxes was achieved through the Curie principle, i.e., the fluxes and thermodynamic forces don't couple each other.

The next work on diffusion flames in subcritical and supercritical systems by Huo et al. [2014] studied the extinction strain rate, which shows a quasi-linear relation regarding the pressure. It was stated that by co-relation of the flame solution with a standardized strain rate space if the extinction strain rate of the flame is not obtainable. Thereby improving the efficiency of the tabulation for methods such as `FGM, FPI` as they would allow interpolation/ extrapolation of the flame solutions from one pressure to other pressure conditions `a priori`. It should be noted that some disagreements that have been pointed out between the above-mentioned work and work by Zips et al. [2018]. The authors reported that the inlet cryogenic temperature affects the flame location but not the flame structure. Still, it is antithetical to the conclusion of work by Zips et al. [2018] which is mentioned in the following text. It would be of great interest to explore this further.

The next study on reactive modeling of combustion systems by Zips et al. [2018] studied the different flamelet configurations using the ideal EoS flamelet, and real-gas EoS. It was observed that 45% and 25% change in temperature and density predictions between the ideal-gas, and real-gas thermodynamics. The flow variables in the flamelet equations are solved by the ideal-gas equation and then enthalpy corrections are applied. The thermodynamic properties are obtained from the subsequent integration of the thermo-chemical properties, which are assembled in a library.

This work would be incomplete without discussing the work of Lacaze and Oefelein [2012] where they conducted a detailed analysis of the flamelet's assumptions and the sensitivity of the computed flamelet with respect to the pressure, temperature and then tested the sensitivity of the flame structure concerning pressure. They concluded their work by stating that future work should be done in various methods of closures in presumed- probability distribution functions.

The work done by Ribert et al. [2017] in the field of transcritical combustion is interesting. They discussed the SGS contributions to the EoS. It was concluded that the simple SGS models such wouldn't be able to model the system accurately; hence further study on SGS models for the EoS needs to be conducted.

2.2. Droplet dynamics

Bork et al. [2017] conducted an experimental campaign. They studied a free-falling single droplet in a nitrogen environment from subcritical to supercritical conditions. They employed Raman spectroscopy to measure the species concentration and post-processed using adiabatic mixing assumption along with virial equation (up to 3^{rd} virial coefficient) to compute the gas temperature. The authors generated droplets of size from 0.97 ±0.13 mm to 1.94 mm ±0.07 mm and finally concluded that during the free fall, the size of the droplets

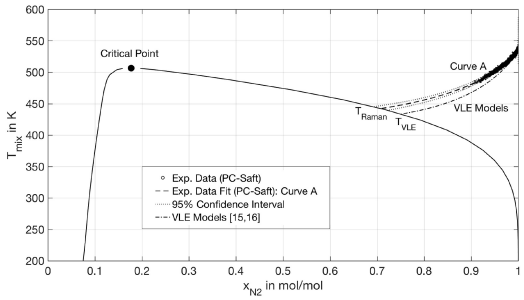

(a) Phase diagram for n-hexane/nitrogen mixture.

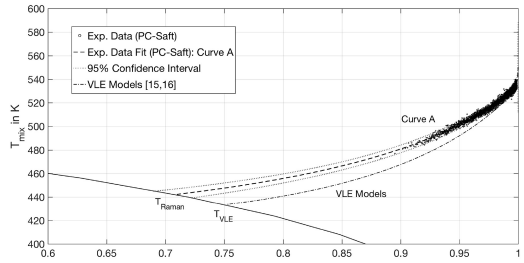

(b) Zoomed image of the comparison between experiments and VLE models.

Figure 2.3: Comparison between the experimental and equilibrium model, from Lamanna et al. [2018] where the role of diffusive fluxes are observed, here both the experimental and theoretical models use PC-SAFT hence the role of diffusive fluxes is highlighted.

didn't vary significantly. The droplets were identified using the n-heptane signals. It was calibrated by measuring the values at different mole fractions, different pressures, and temperatures. The average quantities were calculated from 200 images. The main reason for the implementation of the EoS being the calculation of the departure function of enthalpy to compute the mixture enthalpy for each T_F, x_f, and operating conditions. One of the base papers in the field of Lamanna et al. [2018] studied the effects and improvements in the accurate implementation of non-equilibrium thermodynamics rather than the vapor-liquid equilibrium (VLE). They observed that the VLE models consistently under predicted the surface temperature of the droplets, as seen in figure 2.3. The figure 2.3 illustrates the importance of utilizing NEQ for droplet vaporization. They compared three models namely,

- Abramzon and Sirignano
- Gyarmathy
- Young (linearized version)

Consecutively they scrutinized the probability of the disintegration of an interface. An interface is more prone to disintegration when the interface thickness exceeds the characteristic length of thermal diffusion. They also discussed the other quantities which deviates from the global thermodynamic equilibrium. They utilized DFT to compute the global resistivity of the interface. Finally, they discussed the certain discrepancies observed in the results; namely, the Knudsen number predicted a probability of disintegration of 90%, but in the experimental visualization, the droplet was intact. They reported results consistent with Onishi's theoretical analysis, which states that kinetic effects increase with an increase in temperature and a decrease in droplet size. It was concluded that the local equilibrium assumption does limit the accuracy in the presence of large temperature jumps.

The experimental work used in this validating this work was published by Crua et al. [2017] in high-pressure and high-temperature environments. In this work, they investigated the transcritical droplet dynamics thanks to high-speed visualizations for three fuels,

- n-Heptane
- n-Dodecane
- n-Hexadecane

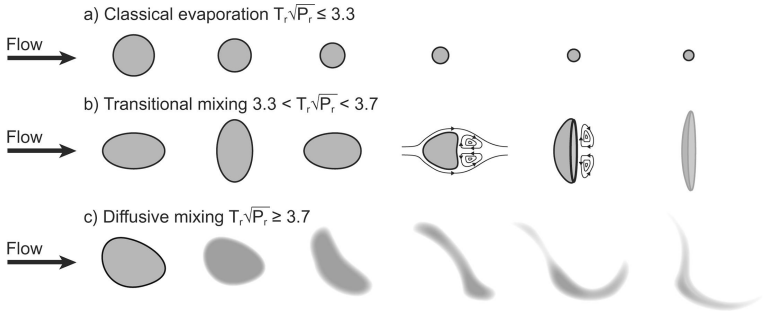

Figure 2.4: Various droplet evaporation mechanisms, from Crua et al. [2017]

They discussed the various difficulties in creating microscopic droplets at transcritical and supercritical conditions owing to the reduction of surface tension, which is the cardinal principle used to create droplets. These are in addition to the visualization challenges due to the dense fuel vapor. The experimental setup is a cubical shape with sapphire windows with the capability to reach 1400 K and 35 MPa. The spray is illuminated from one sapphire window while it is visualized from the other. The injection pressure between 50 and 150 MPa was used.

1. Boundary conditions were set between 700 - 1200 K with pressure between 2- 10 MPa
2. The control volume is a pre-burn type and hence the following products namely N_2, CO_2, and H_2O are present with the respective volume fractions being 89.71%, 6.52% and 3.77%

The significance of the optical system is that it is custom-built illumination where diffuse lighting is used to overcome the effects of beam steering. The other significant effects to be mitigated were, the degradation of the focus and the local density fluctuations due to the evaporation. Consecutively, the presence of surface tension and primary atomization were observed initially at least until 1200 K and 10 MPa.
They obtained a phenomenological model for all the three fuels and concluded the following that on plotting the different mechanisms on the P_r and T_r map, it was evident that the fuel properties do not affect where the diffusive mixing occurs. The fuel properties do affect the timescales and the shape of droplet disintegration. They classified the various regimes of droplet evaporation,

- Classical evaporation: the turbulence can deform and change the trajectory of the droplet. The droplets mostly retain their spherical shape.
- Translational mixing: Initially, the droplets exhibit classical evaporation, but soon, they follow rapid vaporization. The deformation of the droplets and continuous oscillation are the characteristics of translational evaporation.
- Diffusive mixing: There is surface tension, but the magnitude is very low such that the droplets can't be assumed to be spherical. It is governed by a single-phase mixing regime with inter-diffusion and convection.

The figure 2.4 illustrates the three different droplet vaporization regimes that are of interest to this study.

The next study in the experimental is by Manin et al. [2014]. This work was the first to describe the microscopic information at temperatures higher than 800 K. They captured the flow of n-dodecane sprays using long-distance optical microscopy at engine-related conditions. They utilized a preburn type combustion chamber with maximum pressure and temperature of 35 MPa and 1400 K. During this experimental campaign, the tip of the injector is maintained at 363 K. The operating conditions vary from 440 K to 1200 K with pressure from 0.5 to 7.9 MPa. The optical system is composed of three main parts,

- Illumination system: Diffused back- illumination
- A long-distance microscopic lens
- High-speed camera

For a more detailed representation of the setting up of the camera and quantifying the image quality, the reader is suggested to refer the article by Manin et al. [2014]. Finally, they described evaporation at various regimes.

1. Ambient pressure influence at low temperature: Microscopic details were observed at 440 K and pressures ranging from 0.5 MPa to 3.0 MPa at the end of the injection, which is easier compared to the continuous operation due to the turbulence. The end of injection provides slower velocities where the liquid structures are relatively larger while being operated at the same timescale. It was observed that due to the low-temperature difference between the liquid and the combustion chamber, the surface tension is quite significant and holds the droplets and ligaments together. As the pressure is increased, the size of the liquid packets reduces.

2. Ambient pressure at high temperature: Temperature of 900 K was used with an operating pressure of 1.0 MPa and 6.0 MPa. The operating conditions correspond to ECN spray condition A. Till 2.0 MPa, the droplets, and ligaments are quite evident. From 4.0 MPa, the distinction becomes challenging to conclude since the high pressure also affects the optical phenomena associated due to the high pressure. The authors emphasized the fact that the presence of the dark spots doesn't translate into droplets as it can be attributed to the refraction of the high-density gradients between the spray and the ambient conditions. The ambient density can be decreased by reducing the temperature. It was observed that on contrary to the previous conclusion, the surface tension is present in the flow field even though it is considerably less.

3. High-temperature and high-pressure injection: In this regime, they employed a different optical magnification and injector. The same inconsistency was observed. It was seen that droplets do exist for almost a millisecond. This implies that the surface tension does exist during the injection. Hence, even though the temperature and pressure loci are in supercritical regimes, surface tension does exist, but its magnitude is diminished.

A transcritical droplet in micro-gravity was experimentally studied by Segawa et al. [2005]. In this study, the droplets were generated by the fiber suspended droplet technique. As for the realization of the micro-gravity, two different approaches were followed,

- drop shaft
- parabolic flight of the aircraft with micro-gravity of 4.5 s and 20 s respectively

In this study, the ambient temperature was set at 820 K. 1-Octadecanol, with a droplet diameter of 1.0 mm is utilized. The droplets were generated from solidified fuel. The experiments were carried out to study ignition delay and temperature's temporal variations for a range of reduced pressures from 0.3 to 2.4. As for the issue of ignition delay, the reduced pressure was increased till 1.5, the ignition delay increased, but the ignition delay started decreasing after the maxima. They largely attributed it as an unexplained process.

Similarly, they investigated the burning time, which was favorably affected by the reduced pressure, i.e., as reduced pressure increased, the burning time also increased. They reported a distinction between the supercritical and subcritical droplets' temperature's temporal variation. For the subcritical droplets, after the temperature crossed an inflection point, it became a plateau. In contrast, for the supercritical, the temperature's temporal variations were increasing with two inflection points and finally decreasing. Finally, they studied the effect of the reduced pressure on the time it takes for the surface temperature to reach a critical state. They concluded the study stating that more non-intrusive methods are required for the acquisition of the droplet temperature.

The work published by Chauveau et al. [2008] is also utilized in this thesis in validating the 1-D models. They conducted an experimental campaign on the droplet vaporization as to ascertain the three fundamental assumptions on the droplet vaporization,

- Constant and uniform droplet temperature which is complicated due to the initial heat-up period to its wet-bulb temperature
- Spherical symmetry's physical justification by comparing the results in normal gravity and micro-gravity
- Gas-phase quasi-steadiness, this phenomenon has garnered recent attention due to the deficiency of the d^2 law

They investigated the effect of the fibers by,

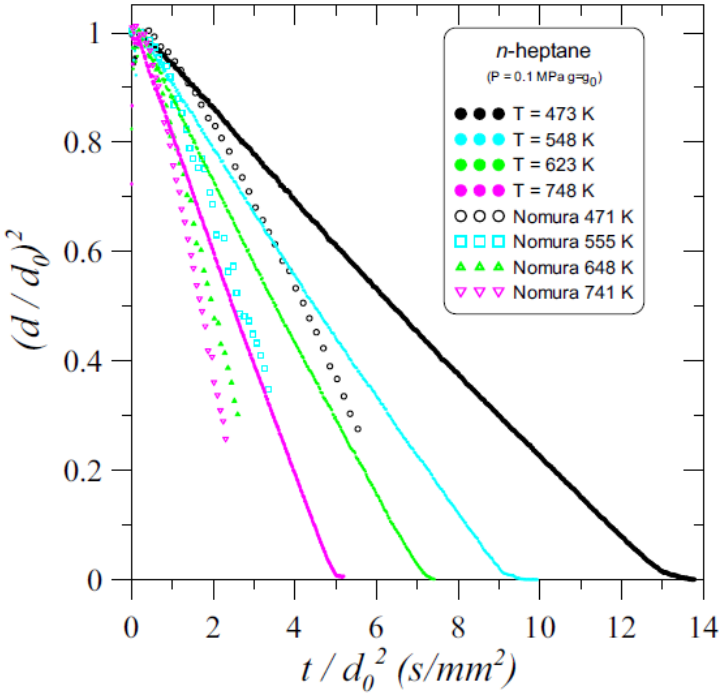

Figure 2.5: Collation of droplets in various ambient temperatures at P = 1 bar and normal gravity, the line corresponds to Chauveau et al. [2008]

- Using classical fiber
- A novel cross fiber technique

They noticed that the data they obtained were of lower vaporization rate compared to the other works. On detailed investigation, it was found that the fiber plays a significant role in the vaporization rate of the droplet due to the heat conduction through the support fiber. They also determined a new vaporization rate to support the observed data as the previous data used a larger support fiber, e.g., the diameter of the cross-fit fiber is $14\mu m$, whereas the conventional fibers have a diameter of $120\mu m$. The data from this study are used to validate the 0D model in this study. The figure 2.5 shows the droplet lifetime of n-heptane at different temperatures under low-pressure under the influence of gravity.

The following section deals with the Computational studies on droplet dynamics. Rainer et al. [2013] published a work on the implementation of diffuse interface models for transcritical conditions. They validated the model with the Sandia n-dodecane non-reacting test case obtained using high-speed imaging. They exclusively investigated the transition of classical jump to the diffusion dominated process. They utilized a 32-term BWR equation coupled with non-linear mixing rules. For the computation of the mixture states, they employed the extended corresponding states (ECS). They utilized the following models,

- The individual properties are combined at the required temperature using ECS
- A pressure correction term is applied

The same procedure is followed to compute the viscosity and thermal conductivity. Since they computed the interfacial profile in equilibrium conditions hence, they utilized the minimization of the Helmholtz energy,

$$\sum_i \sum_j \frac{1}{2} \kappa_{i,j} \frac{d\rho_{M,i}}{dn} \frac{d\rho_{M,j}}{db} = \omega(\rho_M) - \omega_s \tag{2.6}$$

where $\kappa_{i,j}$ is the influence parameter, ρ_M is the molar density and n is the normal interface direction, $\omega_s = -p_s$ is the equilibrium and $\omega(\rho_M)$ is the grand thermodynamic potential energy density. They obtained the surface tension and interface width after determining the species density profiles.

They have complimented the numerical work with the experimental observations of n-dodecane jets at the conditions comparable to diesel engine operation, namely T1 = 400 K, p1 = 29 bar, and T2= 900 K, p2 = 60 bar. They made sure that the ambient density was constant at $22.8 \frac{kg}{m^3}$ to ensure similar jet penetration and gas-liquid interactions. The surface tension was quite evident in the former case, while the droplets or ligaments seem to be absent in the latter's operating conditions. To supplement the above study, they studied the effects of the mixture fraction using a numerical framework and computed the Knudsen number as well. Based on the Knudsen number, they considered the applicability of the diffuse interfaces. On the contrary to popular understanding, they postulated that the diffuse interfaces are developed not because of the vanishing surface tension but because of the combination of the broad interface and reduction in free mean path, which results in continuum regime. They also advised to utilize two-phase models for low-temperature systems as the Knudsen number was found to be high.

In the study by Lafon et al. [2008], they extensively described the simulation of liquid oxygen droplets in the environment of hydrogen. They paid particular emphasis on the water-vapor condensation in LOx droplet. The authors included Dufour and Soret's cross-diffusion terms, but forced convection and buoyancy were neglected. It is interesting to note that the formulations used for the droplet vaporization rate were also based on Onsager's irreversible thermodynamics, $\dot{m}_i = K_{vap,i}(\mu_i^l - \mu_i^g)$. The numerical model does allow the system to deviate slightly from the thermodynamic equilibrium, but the pressure equilibrium was instated via the momentum equation, $\nabla p = 0$. They also noted that the value of $K_{vap,i}$ has a negligible effect on the results. As soon as the system reaches the critical mixing state, the single-phase supercritical fluid is used. Special treatment was given to the water condensation when the water's partial pressure is higher than the saturation pressure leading to the condensation of the water droplets. They laid pronounced emphasis on water droplet formations in determining the critical droplet radius and also for the mass condensation rate of the water droplets. As for the evaluation of the viscosity and thermal conductivity, the ECS model was utilized. The grid was modified as the droplet surface regresses due to the vaporization. The equilibrium conditions from the phenomenological relations are applied to the droplet before it attains a single phase. In this work, they studied the characterization of the droplet at supercritical conditions. They proposed two methods namely,

- Definition based on the critical mixing temperature: More suited for experimental characterization
- Definition based on the critical mixing composition at a given pressure: More suited for the spray analysis of mixtures

The simulations conducted were conducted both in subcritical and supercritical conditions. In subcritical conditions (p = 10 atm), the droplet reaches its pseudo-wet-bulb temperature very soon and then flattens out while in near-critical conditions (p = 100 atm), the temperature is continuously increasing throughout the time interval. As for the very high pressures (> 100 atm), the critical mixing state was reached very soon. They also studied the droplet lifetimes for a range of temperatures and pressures. In subcritical vaporization, the process is influenced by the enthalpy of vaporization. In contrast, it is by thermal diffusion in supercritical conditions. They noticed that the divergence in the specific heat balances out the vanishing enthalpy, thereby leading to smooth change. Numerical models with and without the Soret and Dufour terms were conducted. They formulated an analytical method for the determination of the lifetime of the droplets, and an excellent correlation was obtained. They concluded the studies that the condensation of water does affect the lifetime of the droplets, adding that the size of the water droplets doesn't affect the droplet lifetime.

Yang et al. [2014] was studied the evaporation and the aerodynamic interaction of droplets with strong convective environments at transcritical conditions. They also validated the numerical framework qualitatively with the experimental data. As for the validation, they utilized a high-speed photography. The properties at different velocities were validated with 48 m/s, and the thermodynamic property variations were studied at 75 m/s. The gist of the study was that the ambient temperature and pressure affect the heat and mass transfer coefficients, but in the initial stages, the temperature doesn't affect the heat transfer and mass diffusion. As for the drag force, an opposite trend was observed. Initially, the decrease in drag force was significant in the high pressure, but slowly the effects were reduced as time progresses. It is important to note that the droplets used in this study were quite big (1 mm) compared to the ones in practical conditions.

Balaji et al. [2011] studied simulation of stagnant and convective droplets of n-dodecane. They considered a spherical system (r, θ) in an infinite expanse of high-pressure nitrogen. The numerical method is capable

of modeling the dissolution of gas into the liquid phase. The VLE framework was easily validated with the existing works. The model was modified by including buoyancy due to the normal gravity in the momentum equations. The zero-gravity and the conventional flows were simulated and validated with the available experimental results. The conventional flows had a better correlation, and the errors increased as the ambient temperature increased. The authors attributed the same to the inconsistency in the administration of the experiments.

As a first step, they studied stagnant droplets: They concluded that the droplets in subcritical conditions have higher lifetimes as the pressure increases ($p_r < 6$). In supercritical conditions, the evaporation is entirely transient. In critical conditions, the evaporation initially increases then it flattens out. They also reported that in the vicinity of the critical temperature, the ambient pressure has little effect on the evaporation constant. On comparing the evaporation rates in different regimes, it was observed that the supercritical condition has a local maximum, which was attributed to the controlling process, the mass diffusion. On the contrary, in subcritical conditions, the evaporation reduced with an increase in pressure. They studied the evaporation characteristics of moving droplets with a velocity of 0, 0.5, and 1.5 m/s. One of the significant assumptions they employed was that the droplet is spherical, and they justified it by stating that the droplet deformations occur after it is heated to the critical temperature. They studied the isotherms of the droplet as to visualize the variations in time. It was noted that as time increases, the droplet becomes asymmetric due to the unsymmetrical evaporation because of the stagnation point located in the front. It was concluded that as the velocity increases, the lifetime of the droplet reduces due to the increased heat and mass transfer. The penetration distance is defined as" the distance till which the droplet can travel without disintegrating." It was seen that as the initial droplet velocity is increased, the penetration length increases.

So far, only single droplets have been studied. Regarding the multiple droplets, the following two works hold prominence. The recent work by Duwig et al. [2018] on DNS and LES models for 14,000 droplets of n-heptane in nitrogen in hot turbulent flows is fascinating. The work was aimed at shedding light on the potential avenues for future research in droplet dynamics. For DNS, the interface was resolved, whereas, for the LES, Lagrangian particle tracking (LPT) was utilized to ascertain the potential loss of physics. As for the DNS, the immersed boundary method is used. For the LES, 3DA, a low Mach number code was utilized. The distinctive features of this study include, incompressibility assumption and Germano SGS model. The work illustrates the effect of the turbulence on evaporation dynamics. It was observed that once the centerline gets saturated with fuel vapor, it promotes condensation of the droplets. One-way coupling between the LES sub-grid and LPT was used. They concluded the study after calling for better closures for the LES and LPT since significant differences were observed between the diameter and the standard deviation of the droplets.

Meng and Yang [2014] combined two facets of droplets dynamics namely,

- Droplets in convective environment
- Droplets in tandem

They studied the vaporization of two LOX droplets ($50\mu m$) in supercritical hydrogen environments. The conditions were varying between 100 and 400 atm with initial droplet velocity being 2.5 to 20 m/s. They observed that,

- In the event of multiple droplets, the Marangoni force has more relevance rather than the viscous force.
- The distribution of the droplets in spanwise and streamwise directions has more consequence compared to the turbulence.

The model consists of two subcritical LOX in an atmosphere of hydrogen in supercritical conditions. The flow field is considered as a laminar, and SRK EoS is used for the thermodynamic closure. In this study, the velocity and the ratio of space between the droplets to the radius of the droplet (H/R ratio) is varied to quantify the various phenomena occurring at the droplets in tandem. The maximum freestream Reynolds number in this study was 300, and the droplets are considered to reach the supercritical state as soon as the droplet is released into the hydrogen environment. They concluded that,

- As the pressure increases, the effects of the droplet-droplet interactions reduce.
- As the H/R reduces, the leading droplet merges into the trailing droplet.
- The trailing droplet's lifetime is increased, but the converse is not valid.

- There's a threshold spacing ratio, after which the droplet acts independently.

Lamanna et al. [2007] and Miller et al. [1998] utilized NEQ to study the droplet vaporization. The former studied different models for vaporizing droplets in high-pressure environments. They employed,

- Three mass transfer analogy methods
- Two Langmuir–Knudsen models: one model with infinite liquid conductivity and one with finite conductivity

They observed that the LK models perform particularly well in the initial stages, where the classic D^2 wasn't satisfied. In the work of Miller et al. [1998], they investigated the effects of non-equilibrium thermodynamics. Diameter and temperatures were predicted for single-component fuels, namely, water, n-hexane, n-heptane, n-decane, and benzene. They reported that in low evaporation regimes, all models were consistent for but as the temperature begins to increase, the slip velocity increases, and the size of the droplet (diameter < $50\mu m$) is decreased the deviations between each model increased. In total they studied,

- Two transient classical model
- Four heat & mass transfer analogy models
- Two non-equilibrium models

They described the Lagrangian equations representing the position, velocity, temperature, and mass of a single droplet. f_1 represents the corrections to the stokes drag, Sh the Sherwood number, and Nu the Nusselt number. The following three variables are changed respectively for the different models,

- f_2, the correction to the heat transfer arising due to evaporation
- $H_{\Delta T}$, the non-uniform temperature effects
- H_M, the driving potential for mass transfer

As for the second item, it was used only in the last non-equilibrium model (M8). The non-equilibrium model is based on the Langmuir-Knudsen law. After the comprehensive study of the above-mentioned models, they concluded that both the non-equilibrium models gave good predictions of droplet size and temperature distributions, but the finite conductivity model over-predicted the initial temperature profile due to the inability to provide initial droplet temperature.

2.3. Phase-field methods

Phase-field methods started mainly with the work of van der Waals (van der Waals [1893]), who suggested that the description of an interface with local variables, namely density ρ and temperature T would lead to a very sharp interface and surface tension tends to zero.

NSCH is one of the most utilized models of phase-field methods, because of its applicability to binary mixtures.

Khatavkar et al. [2006] studied the scaling of diffuse-interface methods using non-dimensional equations for two immiscible fluids in a cavity flow. In the study, they highlighted the relative complexity of the scaling in the non-equilibrium conditions compared to the equilibrium model. They utilized Helmholtz energy for the mean-field theory with the mass fraction of one of the species as the order parameter. As for the classical part of the Helmholtz's energy they utilized Landau- Ginzburg free energy,

$$f_0(c) = \frac{1}{4}\beta c^4 - \frac{1}{2}\alpha c^2 \tag{2.7}$$

where the α and the β are the positive constants for an isothermal system. Also, it is important to note that the mass fraction should satisfy the Cahn-Hilliard equation,

$$\rho(\frac{\partial c}{\partial t} + \mathbf{v}\cdot\nabla c) = \nabla\cdot M\nabla\mu \tag{2.8}$$

where **v** is the velocity, and M is the mobility. Consecutively they studied the effects of the different scaling parameters and found the following relations, $Pe \propto 1/C_h$, $Pe \propto C_h$, and $Pe \propto 1/C_h^2$. In the study, it was quite evident that the scaled interface model resembles to the base case at least till the non-dimensional time of 15 units but soon they observed the agreement between the base case and the scaled case deteriorates as the Ca was set to O(1), the agreement between the cases is good till the non-dimensional time of 5 units. Following this, they investigated the effect on viscosity on the stretching of the mode where they noticed that as the viscosity ratio decreases, stretching is observed. They concluded that the above studies aren't able to emulate the topological changes observed in the base diffuse interface model and said that they need further research to develop a numerical framework to work on large scale diffuse interface methods.

In the work by Nayigizente et al. [2018] in the field of the interface thickening method, they investigated the suitability of canonical isothermal and non-isothermal cases using AVBP (CERFACS LES solver). They also discussed the existing methodologies in the field of interface thickening. They utilized the NSK method by neglecting the thermal conduction and the viscous constraints.

After plotting the density distribution and the interface width for different temperatures, they verified the previous statement made by Jamet [1999]," the saturation properties doesn't depend upon the capillary coefficient, but the width of the interface depends on the coefficient." The system reaches a constant value of density for all temperatures higher than the T_c due to the fact there are no heterogeneous systems in supercritical conditions. They suggested that for non-stationary systems, the equilibrium results can be used as an initialization, and the convection and deformation can be added subsequently. They also defined the dependency of the surface tension on the temperature and λ by,

$$\sigma = \int_{x_v}^{x_l} \Upsilon(\rho) dx \tag{2.9}$$

where the Υ depends on the λ, which is related to the shape of the interface. They studied the assumption of constant capillary coefficient. The interface thickness was defined as,

$$h = \frac{(\rho_l - \rho_v)}{max|\nabla\rho|} \tag{2.10}$$

the following relationship was established $h \propto \sqrt{\lambda} \propto \sigma^2$. They enumerated the two methods in the scaling of the interface,

- A previously discussed method in principle in the previous chapter stemming from the work of Jamet [1999]. They computed an analytical solution for the equation $(\mu^{EoS} - \mu^{sat})(x) = \lambda \frac{\partial^2 \rho}{\partial x^2}(x)$. The interface width and surface tension coefficient are given by, $h = \frac{4}{\rho_l - \rho_v}\sqrt{\frac{\lambda}{2A}}$ and $\sigma = \frac{(\rho_l - \rho_v)^3}{3}\sqrt{A\lambda}$. It is evident that any interface width can be obtained by varying σ and A, but as discussed, it leads to a change of compressibility coefficients in the bulk phases.
- The other scaling method based on the modification of the functional Ψ given by the relation $\Psi = \frac{\partial \rho}{\partial x}$

The authors then proposed the Thickened Interface Method (TIM), which is a combination of the above two models, i.e., the definition of new parameter for the capillary and surface tension along with the modification of the EoS. First, the chemical potential is accounted for the modifications, and the other thermodynamic properties are computed. The following protocol is observed for the TIM method,

- The TIM is observed only for the bi-nodal region.
- The modified chemical potential is computed from the EoS and the saturation properties.
- Consecutively, the free energy, pressure, specific entropy, and specific internal energy and other properties are computed.
- The system is complemented by including the modifications to the capillary coefficient.

The model reproduced the results without loss of accuracy, further TIM method was implemented for both 2-D isothermal and non-isothermal system. The errors obtained were significantly low, 5% for the isothermal case, and as for the non-isothermal case, the results matched with different scaling thickening coefficients (F) with slight damping of the interface oscillations. Finally, they simulated a liquid jet in its vapor and found

the results satisfactory. They concluded the study by citing the few singularities such as the damping of the fluctuations (as seen in figure 2.6), considering the fact the capillary terms are non-dissipative.

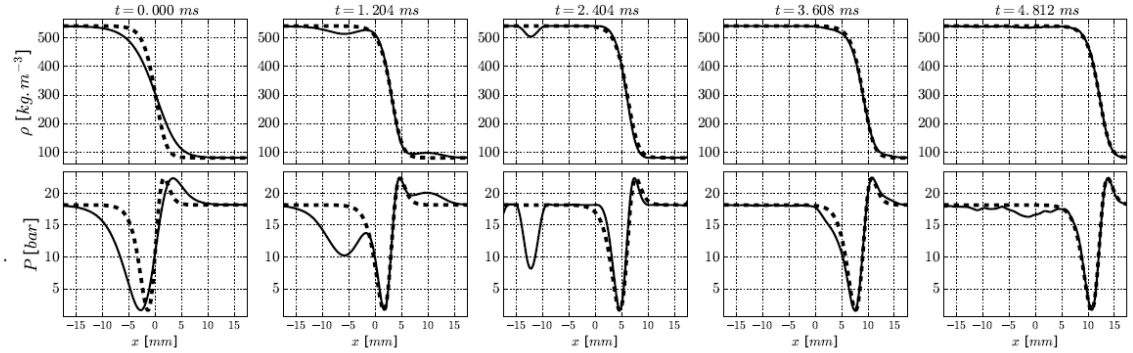

Figure 2.6: Spatial variation at various times of the density and pressure studied in the article Nayigizente et al. [2018], the dotted lines correspond to true diffuse interface model.

Gaillard et al. [2016] published a work on the modeling of the 1-D flame models using finite differences in a staggered grid. They studied a transcritical flame model using diffuse interface methods (NSK model) in low Mach number conditions. They used LOX/ Hydrogen system. As for the thermodynamic closure, they used SRK EoS. They used the small Mach number assumption to reduce the complexity in the momentum equation. Interestingly, when the small Mach number assumption is used, in the absence of the capillary, the gradient of bulk thermodynamic pressure goes to zero. Hence, to justify, a planar interface was assumed such that all the properties change concerning the normal coordinate. The planar interface is the characteristic of the stagnation point. The bulk thermodynamic pressure is given by the SRK EoS. During the study, they laid special emphasis on the gradient of the pressure in the computation of the specific enthalpy because of the presence of the singularities, such as mechanical critical points. They found out that the gradient overshoot decreases with the increase in ambient pressure. Therefore, they replaced the original equation with a smooth function. They particularly recommended formulations for the dissipative fluxes as to avoid the singularities. Following which they modeled Oxygen/ Hydrogen flames using ´O Conaire's mechanism and statistical thermodynamics for the computing the reaction rates. During the stability analysis, they observed that water does condense in flames consistent with the previous observation of Lafon et al. [2008], but water droplet dispersion wasn't included; hence they simplified the issue by including the water to the species list. Since the earlier studies showed that the water droplets are small, and they follow the local motion of the fluid.

An influential work in diffuse interface methods was published by Guo and Lin [2015]. This work extensively deals with the development of diffuse interface models for incompressible fluids. The authors describe the various NSCH models. They observed that at the time of their work, the majority of the studies utilized,

- Navier-Stokes equation with extra stress terms
- Phase-field, i.e., advective Cahn-Hilliard equations from free energy

They demonstrated that the previous studies utilized the classical equations were used for the energy or without the energy equation for an isothermal system thereby leading to inconsistencies. First, they derived, a binary compressible framework along with thermocapillary with mass concentration as the phase variable. Then the system was reduced to binary incompressible system with thermocapillary effects. They proved the thermodynamic consistency of the equations by obtaining the first law, the second law of thermodynamics, Onsager's reciprocal relations, and finally Galilean invariance. They suggested a range of phase variable depending on the application,

- Density for a single component compressible system

- Mass concentration for a binary compressible or incompressible system and
- Pressure for an isothermal incompressible system

The first case to be investigated was temperature-dependent, the non-classical terms were included both into the free energy functional and the entropy functional, i.e.,

$$\hat{u}(s,\rho,c,\nabla c) = u(s,\rho,c) + \lambda_u \frac{1}{2}|\nabla c|^2 \tag{2.11}$$

$$\hat{s}(T,\rho,c,\nabla c) = s(T,\rho,c) + \lambda_s \frac{1}{2}|\nabla c|^2 \tag{2.12}$$

$$\hat{f}(T,\rho,c,\nabla c) = f(T,\rho,c) + \lambda_f(T) \frac{1}{2}|\nabla c|^2 \tag{2.13}$$

where the additional terms in each equation corresponds to the diffuse interface. Here, u corresponds to the specific internal energy, s to the entropy, and f to the Helmholtz free energy. The relations that hold for the classical terms were assumed to be true for the non-classical coefficients terms as well, i.e.,

$$f^{grad} = u^{grad} - Ts^{grad}\Big(\frac{\partial \hat{f}}{\partial T}\Big)_{s,\rho,c,\nabla c} = -\hat{s} \tag{2.14}$$

2.4. Hard-sphere systems

Hard sphere systems form the foundation of thermodynamic models based on statistical thermodynamics. It stems from van der Waals EoS, through the term $v - b$. In this school of thought, it is postulated that all the physical bodies are the aggregate of bodies and space. Two length scales characterize the system, namely 1) average inter-particle space by the number density and the 2) particle diameter σ. As for the number density, it is computed from the mass density, and the σ is the characteristic of the particle, it can be temperature-dependent or independent term. A hard-sphere system is defined as the impenetrable sphere due tot infinitely repulsive force whenever the bodies' center comes within the particle diameter. Still, in some studies, other effects are also included, such as soft-repulsion and so on. Two significant interbody potentials (intermolecular potentials) are,
1) LJ potential : It consists of both attractive and repulsive forces and
2) WCA potential : it is a net repulsive force.

Although HS is a simplistic model of the actual system, the repulsive forces dominate the liquids and dense fluid's regime; hence it will be a reasonable assumption to consider just the repulsive forces. It is particularly relevant for the transport properties since a robust model isn't available for the computation of the diffusion coefficient, while concurrently, HS systems contribute to 70% of the viscosity and diffusion coefficient (Mulero [2008]).

2.5. Review of Advanced models of fuel droplet heating and evaporation

An exhaustive review on droplet evaporation and heating model was published by Sazhin [2006]. He elucidated various models and the reasoning behind them. He also distinguished kinetic models and hydrodynamic models. This article helps in identifying the term "Non-equilibrium" with respect to the droplet evaporation. As evidenced in the previous section, the term non-equilibrium thermodynamics denotes different phenomena, in conventional CFD it corresponds to the addition of various source terms to the fluxes. In droplet evaporation, NEQ refers to the procedure of accounting of the molecular distributions in the calculation of the properties.

This work categorically classified the droplet evaporation into the following classes,

- Uniform droplet temperature with respect to both time and spatial
- Infinite liquid conductivity models(no spatial gradients)
- Finite liquid thermal conductivity without accounting for re-circulation inside the droplet
- Finite and effective liquid thermal conductivity
- Vortex-based models for describing the re-circulation within the droplets

- Full solution of the Navier-Stokes equation

The author mainly describes the various methods of solving the droplet heating models like decoupling of the liquid and gas-phases due to the separation of the time scales, as utilized in the commercial CFD suites. One of the interesting models is the parabolic temperature model, where the temperature profile is assumed as a parabola inside the droplet. It was reported that this model worked well after the initial heat-up period and gave promising results when compared to the computationally intensive finite thermal conductivity model. The application of this model is based on the timescale separation, the liquid's thermal conductivity is higher than the gas thermal conductivity. Still, the liquid diffusivity is, on average, three orders less than the gas diffusivity. Therefore, they postulated solving the equation taking into account the liquid thermal conductivity. The equation is given by,

$$T(R,t) = T_c(t) + [T_s(t) - T_c(t)]\Big(\frac{R}{R_d}\Big)^2 \tag{2.15}$$

Where T_c and T_s correspond to the temperature of the droplet at the center and surface. R and R_d are the corresponding radius at the location under study and the radius of the droplet. The following protocol was utilized,

- The average droplet temperature was computed from the energy balance using the corrected heat transfer coefficient following which the center and surface temperature is computed
- Finally, the radial temperature distribution was computed

The author also discusses various Nusselt number correlations starting from Nu= 2, which corresponds to steady and stagnant droplet heating to more complex Nu correlation based on the viscosities, Re and Pr for large Re. Finally, on droplet heating, he justifies the reason behind simplified models for radiation due to the very high characteristic speed of radiation. The droplet evaporation can be classified into two categories based on two processes that occur,

- Hydrodynamic models
- Kinematic models

These two process deals with the detachment of the fuel vapor molecules from the droplet surface and diffusion of the fuel vapor from the surface into the ambient gas. Usually, the computation of the former needs velocity distributions; hence it can be neglected when the droplet is assumed to evaporate under saturated conditions of the fuel vapor. The author discusses the Spalding heat and mass transfer computed from the conservation of energy and mass

Kinetic models play a vital role in describing the physics of droplets at low pressures and very small droplets where continuum assumption doesn't hold, and there is a jump in the temperature, species, and concentration. After approximation, the multi-particle distribution functions becomes a single Boltzmann equation. The author mainly dealt with fluxes of Maxwellian distribution leading to the famed Hertz-Knudsen-Langmuir formula namely,

$$j_{1g} = \frac{\beta_m}{\sqrt{2\times\pi R_g}}\Big(\frac{p_{vs}}{\sqrt{T_s}} - \frac{p_{v\infty}}{\sqrt{T_g}}\Big) \tag{2.16}$$

where β_m is the evaporation coefficient computed from experiments/ molecular dynamics simulations, R_g is the gas constant, p_{vs} and $p_{v\infty}$ are the saturated fuel vapor pressure at surface and infinity. After computing the jump in the species, velocity, temperature, the hydrodynamic models can be used to describe the evaporation process. The kinetic models are quite captivating in their ability to model even the initial dynamics of the droplets. Still, they are quite intensive, and there have been few works as discussed in the previous sections namely, Lamanna et al. [2007] and Miller et al. [1998] which uses empirical correlations to model the jumps in the properties of the droplets have been used.

2.6. Novelty

With this review of state of the art, it is evident that no droplet evaporation in 3-D using phase-field methods has been studied. This work has modeled the droplet vaporization in 3-D using phase-field methods.

3

Equation of State

EoS is a mathematical closure relating the thermodynamic properties namely, pressure, temperature, density, and composition. As for this study, two classes of EoS were studied. They are,

- Cubic equations and
- SAFT equations

Cubic equations are the most used EoS due to their versatility and relatively low computational expense. Any EoS which is cubic and has explicit pressure terms are called as cubic EoS. Cubic equations date from the work of Van der Waals. PR-EoS is the most popular equation of state. The cubic equations do have the disadvantage of under-predicting the liquid density near the transcritical region; hence more sophisticated equations of state stemming from the molecular thermodynamics, namely PC-SAFT is also used.

3.1. Cubic-EoS

Ideal gases have two main assumptions that need to be inspected,

- The gases have no volume
- The attractive forces are neglected

Cubic equations stems from the pioneering thesis of Van der Waals. He focused on including the attractive terms by the proportionality constant, namely "a" and the closest a molecule can come near each other as to avoid self-destruction "b". Many cubic equations were put to test by the passage of time. Two most successful cubic EoS are,

- SRK EoS and
- PR EoS.

van der Waals, during the development, postulated the principle of corresponding states, i.e., any substance at corresponding reduced state (concerning the respective critical properties, namely the critical temperature, critical pressure, and later the acentric factor). Redlich-Kwong was the first to modify the co-volume "b", the terms a and b were computed by applying the criticality conditions giving the Redlich-Kwong (RK)-EoS. Then came the Soave-Redlich-Kwong (SRK)-EoS, where the attraction parameter was formulated into a function of temperature and acentric factor (ω). SRK and Peng Robinson (PR)-EoS are quite similar in formulation except for the denominator of the attractive terms (which was optimized by comparing the Z_c and $\frac{b}{v_c}$ values) and the fitting data. For PR-EoS, vapor pressure data from normal boiling point to the critical temperature was used, whereas, for SRK, it was from T_R 0.7 to 1.0.
As for the values of a and b, they were obtained by the critical criteria, which states that at T_c, the first and second derivative with respect to volume is equal to zero stemming from the fact that the PV isotherm is maximum at T_c.

$$P = \frac{RT}{\tilde{v} - b} + \frac{\alpha a}{T^{0.5}\,\tilde{v}(\tilde{v} + b)} \text{for RK and SRK} \tag{3.1}$$

$$P = \frac{RT}{\tilde{v}-b} - \frac{\alpha a}{\tilde{v}^2+2b\tilde{v}-b^2} \text{for PR} \tag{3.2}$$

EoS	α	a	b
PR	$(1+(0.37464+1.54226\omega-0.26992\omega^2)(1-\sqrt{T_R}))^2$	$\frac{0.45724R^2T_c^2}{P_c}$	$\frac{0.07780RT_c}{P_c}$
SRK	$(1+(0.48508+1.55171\omega-0.15613\omega^2)(1-\sqrt{T_R}))^2$	$\frac{0.427480R^2T_c^2}{P_c}$	$\frac{0.086640RT_c}{P_c}$
RK	1	$\frac{0.427480R^2T_c^{2.5}}{P_c}$	$\frac{0.086640RT_c}{P_c}$

Table 3.1: Equations of States

Figure shows the isothermal compression process. The point B represents the Dew point where small amount of liquid is formed on compressing the fluid. The A represents the bubble point where there is an sudden increase in pressure as liquids aren't that compressible compared to gases. The gradient of pressure with respect to the volume should be negative. Hence, in cubic equations, one section A'B' as seen in figure 3.1 is meaningless and should be neglected. Fig. 3.1 illustrates the conventional PV plot of a cubic EoS.

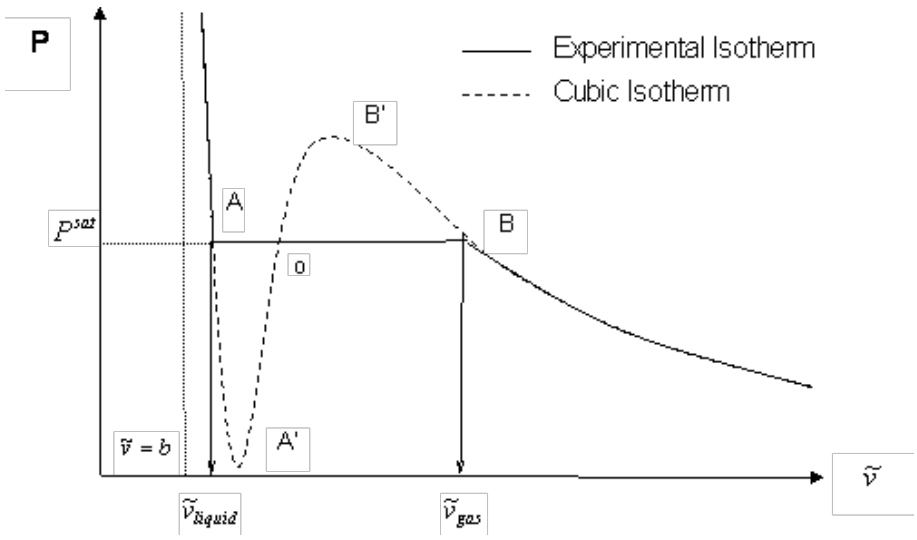

Figure 3.1: PV plot for different isotherms of cubic equations of state from Adewumi [Accessed on 3/31/2020]

3.2. PC-SAFT

The intermolecular forces (although a misnomer) determine the properties of the fluids. In SAFT based models, each force such as repulsion, dispersion (attraction), association, coulombic, and so on contribute to the Helmholtz energy. Once Helmholtz energy is computed, the compressibility factor is calculated by its derivative with respect to the density. Conventionally, contribution by the hard-sphere has strong analytical function whereas, for dispersion contributions, approximate functions are used in Barker and Henderson [1967].

PC-SAFT is one of the robust equations of states to describe the properties of the critical states. PC-SAFT is a version of SAFT where statistical thermodynamics serves as a bridge between the microscopic properties and the macroscopic properties.

In PC-SAFT, the molecules are built of spherical segments. The distinguishing feature of PC-SAFT is that it is a second-order perturbation theory, the first perturbation is for the formation of the chain molecules, and then second perturbation is made for the dispersion terms.

The parameters for the PC-SAFT are,

- Segment diameter (σ)
- Segment number (m) and
- Dispersion energy or potential depth (ϵ/k)

As for the SAFT based models, the perturbation theory is applied, and then the chains are formed, on the contrary, in PC-SAFT the hard spheres are connected to the hard chains using Wertheim´ s TPT1 and then the perturbation theory is applied to get the dispersion terms. The starting point of SAFT based models is the intermolecular potentials. Conventionally it has been regarded that when two hard spheres collide, then they repel each other. It is true, but only when molecules collide with each other at a very slow speed. In the real case scenario, soft repulsion takes place, i.e., it is possible to penetrate beyond a softcore when they collide. This is achieved through Lennard Jones potential.

The next important ingredient of the PC-SAFT is the radial distribution function, which computes the probability of finding another segment. Initially, it will be zero due to the repulsion and increase due to the attraction in the short-range and then approaches one in the far-field. The radial distribution function is used to compute the local density in each volume.

Perturbation theory divides the contributions into repulsive and attractive part. In PC-SAFT, hard chains are the reference, unlike other SAFT models where hard-sphere is the reference. Here the compressibility factor is given by,

$$Z = Z_{ref} + Z_{disp} \tag{3.3}$$

where,

$$Z_{ref} = Z_{ideal} + Z_{hc} \tag{3.4}$$

As for the dispersion contribution, a second-order formulation is used based on the theory by Barker and Henderson [1967]. It is the dispersion terms which gives rise to different classes of SAFT EoS. PC-SAFT attempts to model the dispersion between the whole chains rather than hard spheres hence we utilize inter-chain radial distribution function rather than the intersegment distribution function (Kontogeorgis and Folas [2009]).

In this EoS, an average radial distribution function is used instead of a unique radial distribution function, i.e., the radial distribution function of different segments is the same. As to strike a balance between the complexity and accuracy, a power series in terms of packing fraction is utilized. Hence, the coefficients were obtained by fitting the square-well potential using previously suggested RDF with the real substance data. It improves the EoS in threefold namely,

- It helps in placing confidence in the uncertainties in potentials
- Real substance data can play a mitigating role in the error in the reference EoS
- Spherical segments can be an oversimplification of the actual system

It is in the coefficients significant progress has been made between different PC-SAFT models e.g., some PC-SAFT models included specific heats in the real substance data in the computation of the coefficients. The dimensionless Helmholtz energy is given as,

$$a = a^0 + a^{hc} + a^{disp} + a^{asso} \tag{3.5}$$

corresponding to the ideal, hard chain, dispersion, and association contributions respectively. In PC-SAFT, the hard chains are taken as the reference fluid and dispersion terms are referred to as the perturbation terms. Contrary to the cubic equations, PC-SAFT isn't explicit in pressure, all the computations are done for the Helmholtz energy. The performance of PC-SAFT is tested against the PR-EoS in the upcoming subsection for accuracy of the calculations of density, specific heats, speed of sound, and enthalpy of n-dodecane.

3.3. Thermo-physical and VLE computations

In this section, various thermo-physical and VLE computations of the various EoS are assessed. Figure 3.2 shows the performance of different EoS in the computation of the density, specific heat, speed of sound and log of fugacity coefficient of n-dodecane at 6 MPa. From the figure it is clear that PC-SAFT shows excellent predictions for density and speed of sound in the region of interest. Regarding the specific heat capacity, the RKPR EoS shows good performance (Matheis [2018]). It was decided to decouple the VLE, and the droplet evaporation computation. Since, the system of equations were stiff and during the computation of the VLE in some instances, the COMSOL solver failed. Hence, the VLE was solved beforehand, and then an interpolation was utilized in the further computations. The PR, SRK and RKPR's thermophysical values were taken from Matheis [2018].

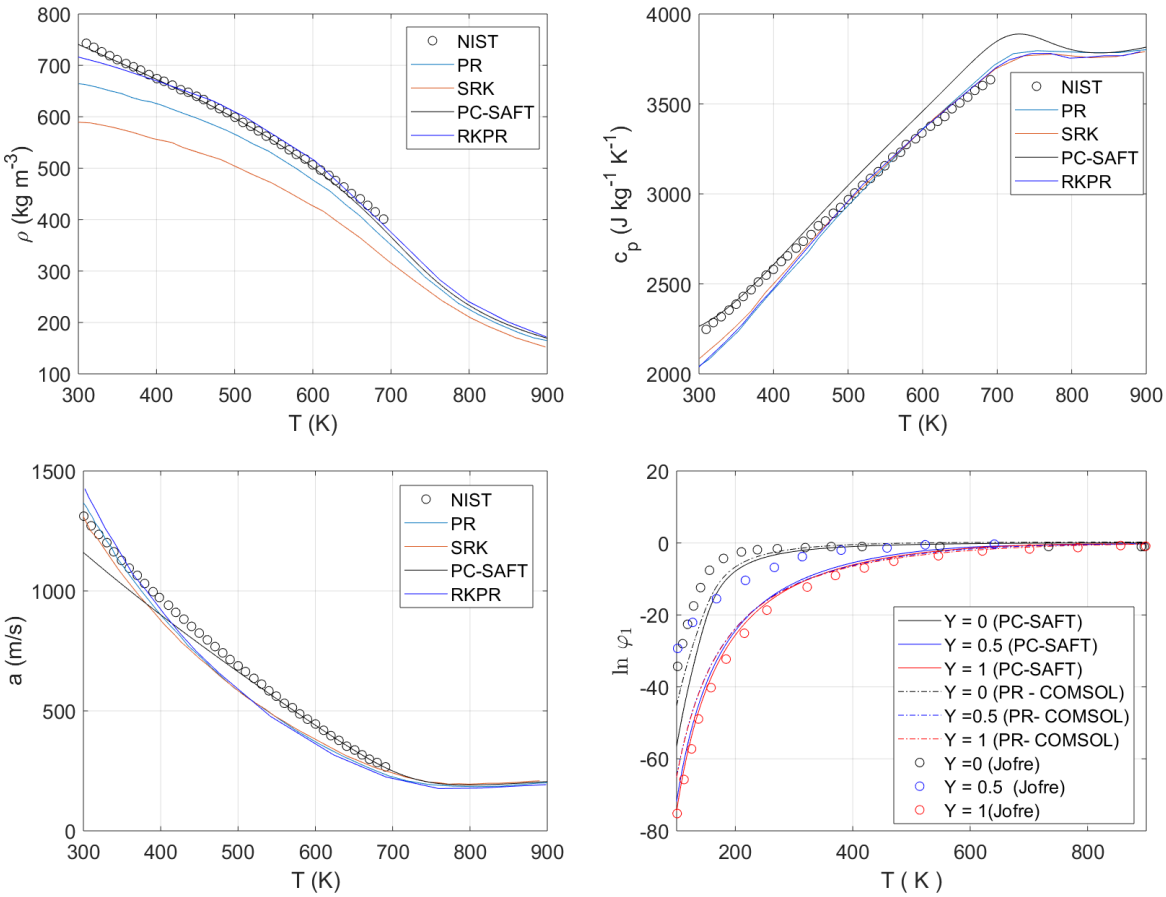

Figure 3.2: Top-left: Density of n-dodecane at P = 6E6 Pa; Top-right: Specific heat capacity of n-dodecane at P = 6E6 Pa, Bottom-left: speed of sound of n-dodecane at P = 6E6 Pa; Bottom-right: Logarithm of fugacity coefficient of n-dodecane/ nitrogen mixture at 1E7 bar with Y being the mole fraction of the n-dodecane.

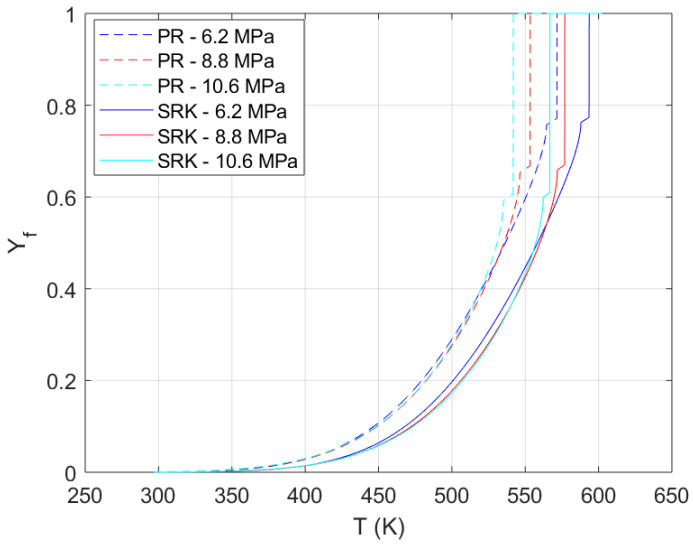

Figure 3.3: Mass fraction of the vapor at the interface computed for n-dodecane using the equality of fugacity for PR and SRK at different conditions

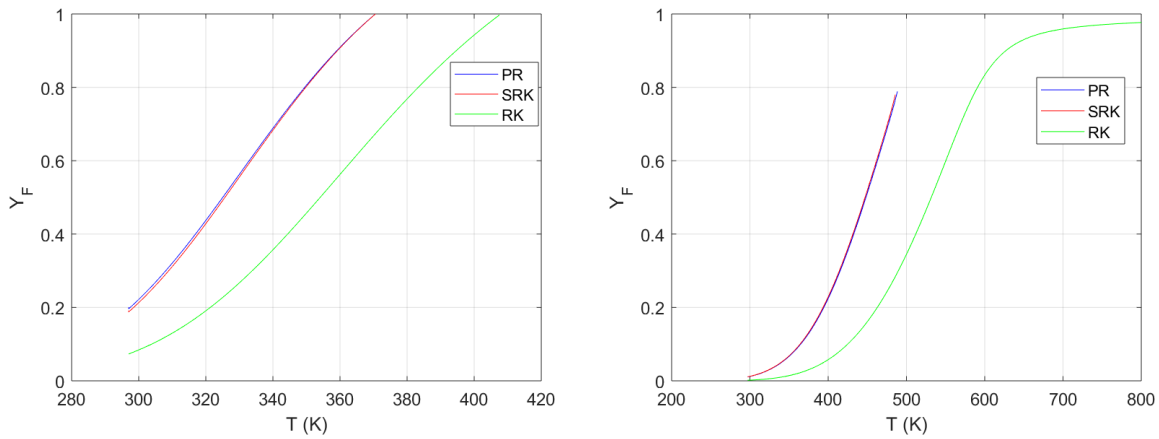

Figure 3.4: The mass fraction of the fuel vapor of n-heptane computed by assuming single component fuel at P = 0.1 MPa and 5.1 MPa

The figure 3.3 shows the mass fraction at the interface computed via equality of fugacity using PR and SRK. While solving for this setup the liquid mass fraction is taken as 1 and the vapour mass fraction is computed using the fsolve command. As for the evaporation models, PC-SAFT isn't utilized due to time constraints. PR-EoS is used for the 3D computations. Figure 3.4 shows the plots of the mass fraction of n-heptane in nitrogen for two pressures. The PR and SRK were obtained from COMSOL Multiphysics and as for the RK-EoS, it was obtained from a MATLAB script based on an optimization routine with fsolve. The obtained mole fractions are consistent with previously reported values for other species system as Octane/Nitrogen and Decane/Nitrogen system.

4

Transport properties

Transport models are an integral part of combustion modeling, transport properties include viscosity, thermal conductivity, diffusivity, and surface tension. Special emphasis in this work was laid on the computation of the diffusion coefficient and thermal conductivity. One main challenge encountered in this chapter was that some models work for specific regimes but do not in other regimes. In search of a utopian viscosity model, initially, Pedersen CSP for viscosity was favored, but soon due to issues in computing the methane's density, Chung's high-pressure viscosity is used for the 3D studies. As for the thermal conductivity, Chung's high-pressure model was shown to be more robust compared to the other models. Excess entropy model was also explored for thermal conductivity, which provides excellent results for moderate to high-pressures, but a mixing rule needs to be developed for the mixtures. The uncertainty in the low-pressures for the excess entropy model stems from the error in the equation of state as they aren't equipped to handle the transition from liquid to vapor. Lastly, the Firoozabadi model is used for the computation of the diffusion coefficient.

4.1. Viscosity

There are good viscosity models available in the literature for the conditions of interest as evidenced in the figure 4.1. In this work, Pedersen's corresponding states (Pedersen et al. [2006]) and Chung's model (Poling et al. [2001]) are studied. In Pedersen's CSP, the viscosity of mixture/ pure species is computed via a well-modeled reference substance in this work methane was used, but Poling et al. [2001] recommended propane.

$$\eta_{mix}(P,T) = \Big(\frac{T_{cmix}}{T_{cref}}\Big)^{-1/6}\Big(\frac{P_{cmix}}{P_{cref}}\Big)^{1/2}\Big(\frac{M_{mix}}{M_{ref}}\Big)^{1/2}\Big(\frac{\alpha_{mix}}{\alpha_{ref}}\Big)\eta_{ref}(P_{ref}T_{ref}) \tag{4.1}$$

η_{ref}, M_{mix}, P_{cmix} and T_{cmix} corresponds to the viscosity of the reference compound, molecular weight, mixture critical pressure, and mixture critical temperature respectively. The α terms are used to include heavy hydrocarbons. Finally, 32-BWR is used for the density computations due to its robustness in the conditions of interest. As for the mixing rules and coefficients, the reader is suggested to go through the chapter 10 of the book by Pedersen et al. [2006]. The viscosity by Chung, LBC, Mass mixing and Pedersesn CSP are shown against the NIST data for two pressures in figure 4.1. The CSP performs better but Chung model is more favored in this work because of its stability. The bottoms subplots shows the effects of mixing rule in viscosity computations. From the plots of the mixture's viscosity, it is found that the Zarzalis mixing rule is found to be predicting relatively more accurate values under these conditions compared to the other models.

Fig.4.1 illustrates the effects of various viscosity models and the mixing rules for the mixtures. Further improvements are required in mixing rules. The experimental/NIST aren't readily available hence they aren't plotted. The Zarzalis mixing rule is taken from the work of Zhang et al. [2015].

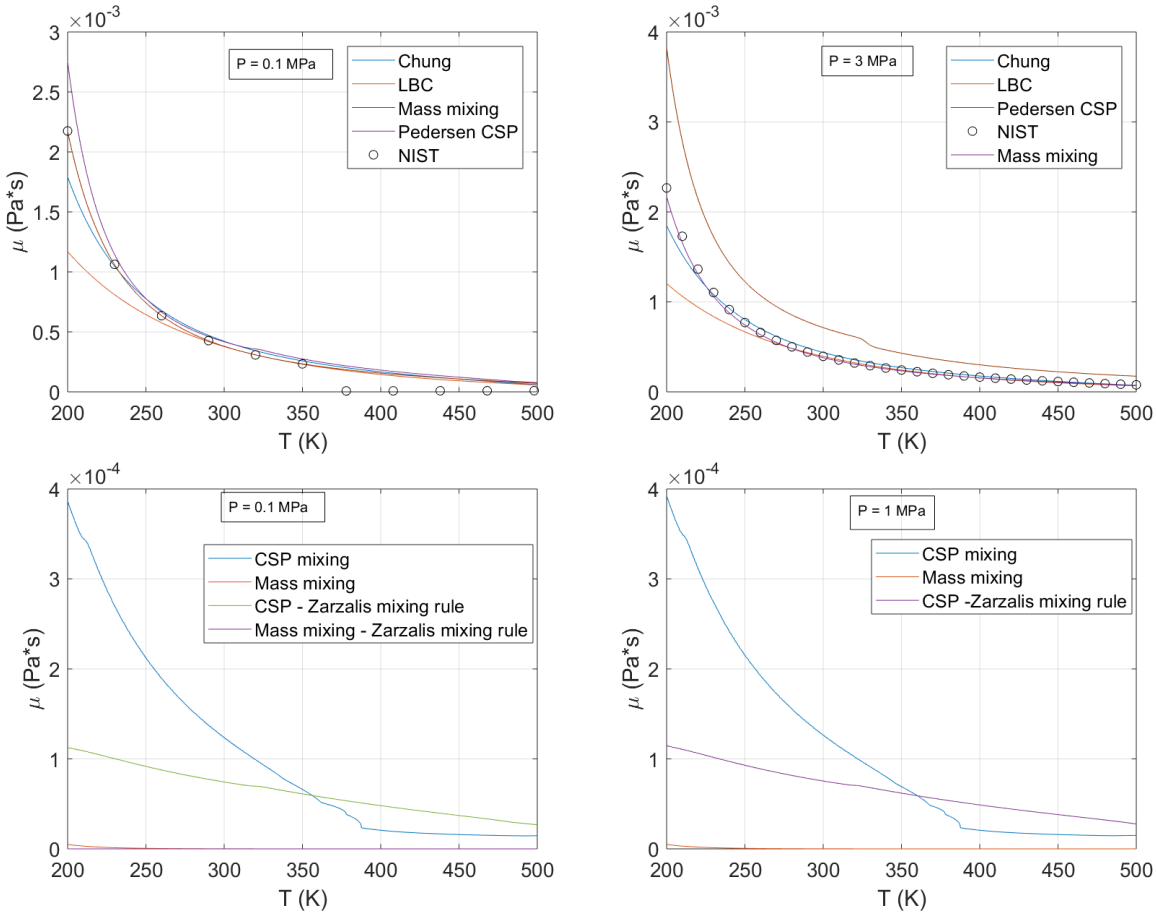

Figure 4.1: Top-left: Viscosity predictions of various models of n-Heptane at 0.1 MPa; Top-right: Viscosity predictions of various models of n-Heptane at 3 MPa; Bottom-left: different mixing rules of Mixture (0.5 N_2 and 0.5 C_7H_{16}) at 0.1 MPa; Bottom-right: different mixing rules of Mixture (0.5 N_2 and 0.5 C_7H_{16}) at 1 MPa.

4.2. Thermal Conductivity

One of the fundamental issues of transcritical flows are the computation of the thermal conductivity. A brief study was conducted to ascertain the various transport models for thermal conductivity. The thermal conductivity models studied in this work were,

- Chung
- Pedersen CSP
- LBC model and
- Thermal conductivity using entropy scaling

4.2.1. Chung model

Chung et al. [1988] developed a multiparameter empirical thermal conductivity model from Chapman-Enskog relation. Chung formulated the net thermal conductivity as the sum of two terms accounting for the low-pressure and high-pressure contributions,

$$\lambda = \frac{31.2\eta^0\Psi}{M'}\left((G2^{-1} + B6 \times y) + q \times B7\, y^2 T_r^{0.5} G2\right) \tag{4.2}$$

where η^0, M', T_c, T_r, and λ corresponds to the low-pressure viscosity, molecular weight, critical temperature, reduced temperature, and thermal conductivity respectively. Few correlations were developed for the computation of the number of collisions in terms of reduced temperature via β.

As for the high-pressure model, the high-pressure thermal conductivity was obtained from the empirically correlated function in terms of density (via the term y), as the reduced density reached 0, the value tends to the low-pressure thermal conductivity. The B7 terms correspond to the high pressure correction. For the complete expressions, Poling et al. [2001] is recommended.

4.2.2. Pedersen CSP

It is one of the most utilized thermal conductivity models formulated by Pedersen et al. [2006]; it is based on the corresponding states principle (CSP). In the original version, the total thermal conductivity is computed from the CSP, whereas in this method, only the translational thermal conductivity is computed using the CSP, and the internal energy contribution is computed separately. Since the internal contribution remains constant, the total thermal conductivity of the reference substance is subtracted from the internal energy contribution of the reference substance. This model requires good EoS for the density prediction. In this work, two EoS, Soave-BWR and 32-mBWR were used. It was found that the 32-mBWR was more suited to model the density of the reference species. There is also a drawback that the λ_{int} is computed using data fitting of methane, and this will be the source of discrepancy for the model as noted by the authors.

$$\lambda_{mix}(P,T) = \frac{(\frac{P_{cx}}{P_{co}})^{2/3}}{(\frac{T_{cx}}{T_{co}})^{1/6}(\frac{M_x}{M_o})^{1/2}}(\frac{\alpha_{mix}}{\alpha_o})(\lambda_o(P_o,T_o)-\lambda_{int,o})+\lambda_{int,mix}(T) \tag{4.3}$$

$$\lambda_{int} = \frac{1.18653\eta^*(C_P^{id}-2.5R)f(\rho_r)}{M} \tag{4.4}$$

The reference thermal conductivity is computed from the following relations,

$$\lambda = \lambda_0(T)+\lambda_1(T)\rho+\Delta\lambda'(\rho,T)+\Delta\lambda_c(\rho,T)$$

For the constants, the reader is directed to refer to the work of Pedersen et al. [2006].

4.2.3. LBC model

LBC method is an alternative to Pedersen corresponding states method. Thermal conductivity is represented as a fourth-degree polynomial in terms of reduced density (Pedersen et al. [2006]). This paradigm of thermal conductivity in terms of reduced density should be inspected. In this work, LBC was formulated based on the manual by Calsep [2011].

$$\lambda_{\text{Total}} = \lambda_{\text{Translatonic}} + \lambda_{\text{Internal}} \tag{4.5}$$

$$\lambda_{\text{Translatonic}} = \mathrm{C_1 T^{C_2} P^{C_3}}\left(\mathrm{a_1}+\mathrm{a_2}\rho+\mathrm{a_3}\rho_{\mathrm{r}}^2+\mathrm{a_4}\rho_{\mathrm{r}}^3+\mathrm{a_5}\rho_{\mathrm{s}}^4\right) \tag{4.6}$$

$$\lambda_{\text{Internal}} = 1.1865\xi\mathrm{C_v}\frac{\rho'_{\mathrm{r}}}{\mathrm{M_w}} \tag{4.7}$$

For further details on the equation, the reader is requested to refer the manual by Calsep [2011]

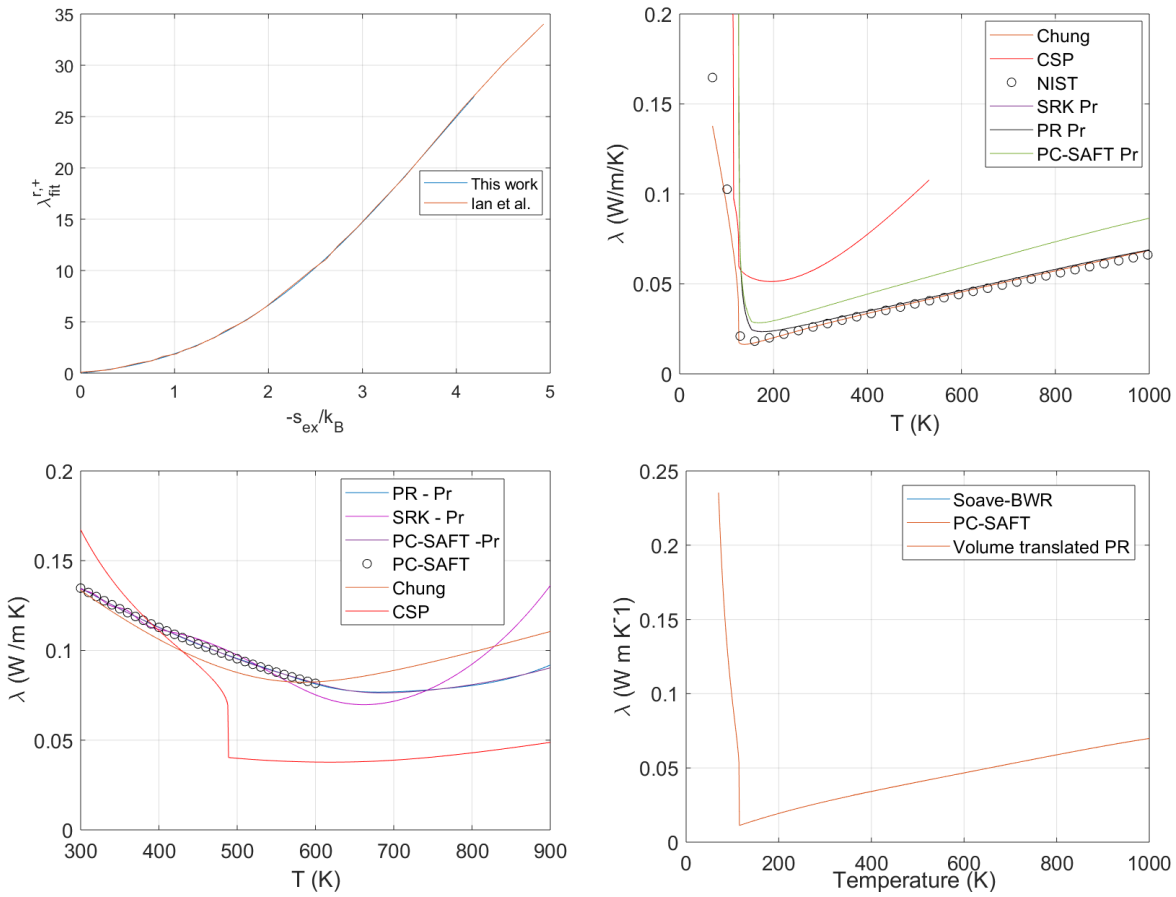

Figure 4.2: Top-left: Non-dimensional entropy vs. scaled λ of this work against the work of Bell et al. [2019]; Top-right: λ of N_2 using different models at 3 MPa; Bottom-left: λ of C_7H_{16} of select models at 10 MPa; Bottom-right: Thermal conductivity via Chung's model using different EoS (N_2 @ P = 10 MPa)

Figure 4.2 shows the various thermal conductivity models along with the influence of EoS on the thermal conductivity predictions. The subplot on the top-left corresponds to the excess entropy predictions in this work against the work of Bell et al. [2019]. Note that the term Pr corresponds to the thermal conductivity from the Prandtl number. It is interesting to gauge the performance of computing the thermal conductivity using Pr. Initial a single Pr number for n-dodecane was planned to use, but due to the varied range of Pr number's from liquid to gas/ dense-gas, a curve-fitted (Fourier series) Pr number was utilized. As for the Pr number fitting, Chung's viscosity and specific heats from EoS are used for the computation of the thermal conductivity ($\lambda = \frac{C_p \mu}{Pr}$) with PR from the NIST webbook's database. Figure 4.4 shows the Prandtl number using different viscosity models with the thermal conductivity from the NIST database. Similarly, the same procedure is followed for nitrogen but with a constant Prandtl number of 0.7. Also, The decrease in accuracy of Chung's model can be attributed to its very high reduced density as the classical high-pressure models are not developed for application in dense gas regime, although Chung's model performs better for N2 which can be observed from the above figure 4.2. For better comparisons, the reader is suggested to refer the appendix A.1.

4.2.4. Excess entropy models

Recently, the excess entropy model of thermal conductivity is getting more attention from the community. Its performance is excellent for single species, and with some effort, a mixing rule can be established. The performance of the excess entropy is particularly impressive for the transcritical conditions. The reader is recommended to refer the appendix-A.1. for the excess entropy results.

4.2.5. Influence of Density predictions in thermal conductivity

Chung and LBC are quite sensitive to the density predictions of the EoS. Hence, a short study was conducted to assess the reliability of the EoS. It was found that PR-EoS is quite unreliable for the density predictions as it gives physically inconsistent values; hence in those cases' volume translated PR was utilized (Abudour et al. [2012]). When volume translated PR, Soave-BWR, and PC-SAFT were used, no discernible changes (in the first two decimal places) were observed as seen in 4.2. In a separate assessment, it was noted that in low-pressure regimes, Soave-BWR's performance is slightly worse inherent due to its low-cost computing nature; hence its better to utilize PC-SAFT EoS.

4.2.6. Mixing rules for the properties

As seen from the previous plot 4.1, the mixing rules do play a pivotal role in the determination of the mixing properties. Hence, it would be advisable to utilize the most accurate mixing rule after comparing it with the NIST data. In this work, the viscosity models can be utilized using the default mixing rule and another mixing rule, as described in the work of Zhang et al. [2015]. It was found that the latter mixing rule is closer to the data in the literature. It is important to note that this rule might not be suitable for all the pairs. As for the thermal conductivity, a range of mixing rules were studied for the excess-entropy model, but it was concluded that the mixing rules that were employed were inferior to the COMSOL in-built modules. Hence, the excess entropy models were not used for the mixture computations. The figure 4.3 shows the performance of thermal conductivity and viscosity of n-dodecane at 6 MPa by various models. The figure 4.4 shows the performance of different viscosity models against the NIST data.

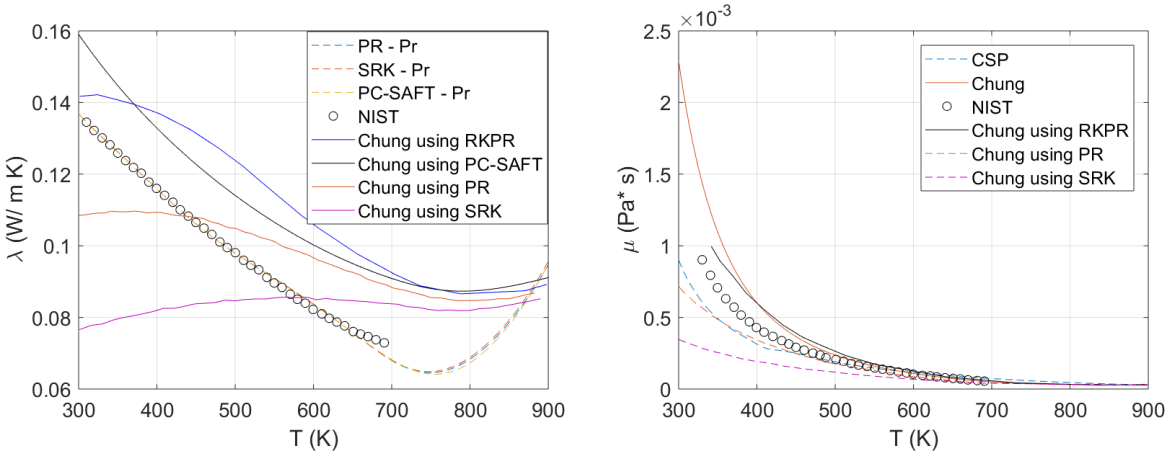

Figure 4.3: Left: Thermal conductivity of Chung's method (using PR, SRK, RKPR, and PC-SAFT), Pr (using PR, SRK, RKPR, and PC-SAFT) and NIST for n-dodecane at P = 6 MPa; Right: Viscosity using Chung's method (using PR, SRK, RKPR, and PC-SAFT) and NIST for the same species at the same condition

4.3. Diffusivity

It was quite evident in the initial phase of the study that there's a lack of diffusion coefficient models, as stated in Poling et al. [2001], especially for the liquid systems at high pressures (dense fluids). Previous studies have employed models such as Tyn—Calus, Hayduk—Minhas (Shuen et al. [1992]), Wilke—Chang (He et al. [2011]), and Chapman—Enskog (Matheis [2018]). These models are used without any corrections, with the Chapman being the most extensively used model. This work focuses on the following models,

- Chapman—Enskog
- Wilke and Lee
- Fuller
- Yale model (Firoozabadi model)
- Bellan's CSP model and

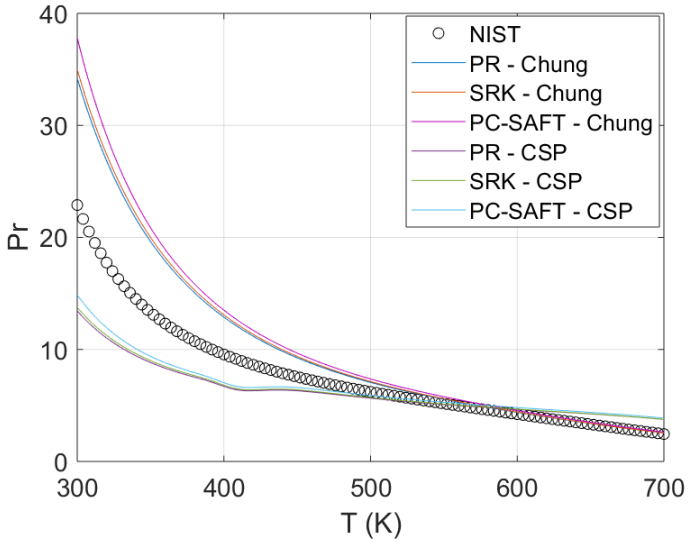

Figure 4.4: Prandtl number using different EoS and different viscosity models

The classical methods of modeling diffusion are: Fick's law, and Maxwell-Stefan law. Fick proposed the Fick's law in 1851, where the flux is driven by the concentration gradients.

$$J_1 = -\rho D_{12} Y_1 \tag{4.8}$$
$$\text{with} \sum_{\alpha=1}^{N} J_\alpha = 0$$

As for the Maxwell-Stefan (MS) form, it can be obtained from the entropy-balance equation. There are two formulations of MS diffusivity, namely Fick's form and MS form. MS's formulation is usually preferred. The most attractive feature of the Fickian model is that most of the experiments measure Fickian diffusion due to the ease of the setup. The MS formulation is given by,

$$\sum_{j\neq i} \frac{x_i x_j}{\mathscr{D}_{ij}} \left(\frac{J_j}{\rho y_j} - \frac{J_i}{\rho y_i} \right) = d_i - \sum_{j\neq i} \frac{x_i x_j}{\mathscr{D}_{ij}} \left(\frac{\mathscr{D}_j^T}{\rho y_j} - \frac{\mathscr{D}_i^T}{\rho y_i} \right) lnT \tag{4.9}$$

x_i, J_i, $\mathscr{D}_{ij}$, $\mathscr{D}_i^T$, and d_i corresponds to the mole fraction, mass flux vector, binary diffusion coefficient, thermal diffusion coefficient, and driving forces respectively. The community mainly uses the Fick's law but it has been observed that the Fick's accuracy is not right even for dilute gas mixtures (Bird and Klingenberg [2013]) and this becomes complicated in the region near the phase transition where sometimes Fick's law predicts diffusivity < 0 thereby making the physical interpretation of the diffusivity difficult. In these cases, Generalized Maxwell-Stefan equations would be of greater utility. Generalized Maxwell-Stephen equations consider the chemical potential gradients as the driving forces for diffusion, which would explain the process of uphill diffusion (Krishna [2019]).

The following subsections deals with the computation of the binary diffusion coefficient.

4.3.1. Chapman—Enskog

It is the classical model for the computation of the diffusion coefficient. It stems from kinetic theory by assuming empirical potential functions. In this work, the model is taken from Poling et al. [2001],

$$\mathscr{D}_{AB} = \frac{0.00266 T^{1.5}}{P M_{AB}^{0.5} \pi \sigma_{AB}^2 \Omega_D} f_D \tag{4.10}$$

$\mathscr{D}_{AB}$, P, T, σ_{AB}, Ω_D, and f_D are the diffusion coefficient in cm^2/s, pressure in bar, temperature in K, characteristic length in Å, collision integral, and correction factor. An ideal gas assumption is used in this model for the computation of the number density.

4.3.2. Wilke and Lee

This is one of the most classical models. It is a modification of the Chapman—Enskog relation, where the mutual diffusion ($\mathscr{D}_{AB}$) is again taken from Poling et al. [2001],

$$\mathscr{D}_{AB} = \frac{(3.03 - \frac{0.98}{M_{AB}^{0.5}})(10^{-3}T^{1.5})}{PM_{AB}^{0.5}\sigma_{AB}^{2}\Omega_D} \tag{4.11}$$

$\mathscr{D}_{AB}$, M_{AB}, P, T, σ_{AB}, and Ω_D are mutual binary diffusion coefficient cm^2/s, Molecular weight of the mixture in g/mol, Pressure in bar, temperature in K, characteristic length of the mixture in Å and collision integral.

4.3.3. Fuller

In comparison with the Brokaw's, Wilke-Lee, basic theoretical and Fuller's model. Fuller's model gave the least average error (Poling et al. [2001]). Fuller's diffusion in this work were taken from Poling et al. [2001],

$$\mathscr{D}_{AB} = \frac{0.00143T^{1.75}}{PM_{AB}^{0.5}[(\Sigma_v)_A^{1/3} + (\Sigma_v)_B^{1/3}]^2} \tag{4.12}$$

Σ_v's are found from summing the atomic diffusion volumes. The atomic diffusion volumes for this study has been obtained from the COMSOL thermodynamic database. The significance of the Fuller's model is that before 1965 there were two classes of diffusion models namely,

- Models which require atomic constants along with group constants such as atomic weight, volume and so, e.g., Gilliland's model
- The next class of models which require supplemental data from the experiments for different groups of molecules, e.g., Hirschfelder-Bird-Spotz method

The Fuller's method combines both the classes, thereby leading to simplicity without reducing the accuracy of the model. Fuller used the atomic and group constants where the constants were obtained from the regression analysis of hundreds of experimental values. It is one of the most robust methods available to compute the diffusivity. Later, Takahashi's correction was also formulated for high-pressure conditions. As noted earlier, the difference between the predicted and observed values are high in high pressures. Takahashi [1975] defined a new correlation based on the reduced pressures and temperatures. It showed good agreement (at that time), with an average deviation of 4.1%, whereas the Slattery Bird (SB) model showed 7.9 %. The DP_R was plotted against P_r with T_r as the parameter.

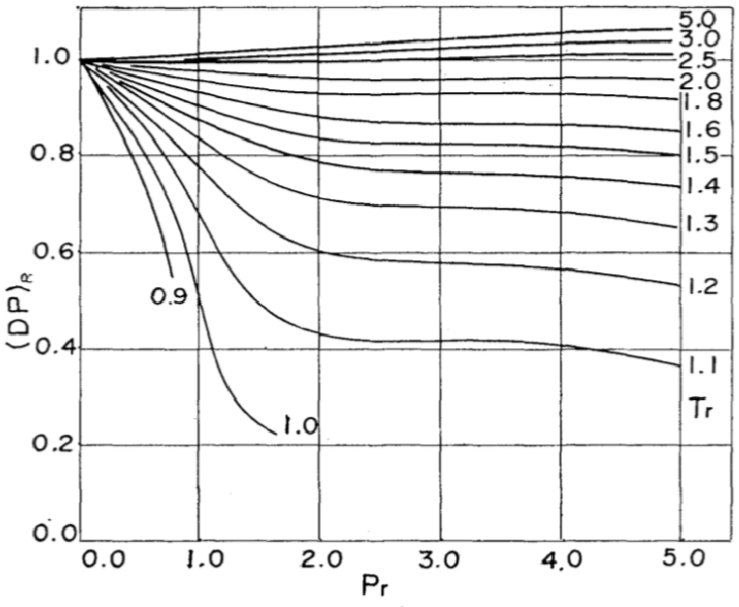

Figure 4.5: Takahashi correction for binary diffusivity from the work of Takahashi [1975]

The figure 4.5 shows the curve fit that Takahashi used to compute the reduced diffusion coefficient and finally the corrected diffusion coefficient. As Takahashi used curve fitting, therefore, as to minimize the error, a correlation-based on curve fitting was utilized from the pioneering work of Palle et al. [2005] for this task.

$$\begin{aligned} &\text{if} \quad T_r < 2.4 \\ (T_r, P_r) &= \frac{exp(aP_r) + b}{1 + b} \\ &\text{if} T_r > 2.4 \\ f(T_r, P_r) &= 1 + cPr \end{aligned} \tag{4.13}$$

where,

$$\begin{aligned} a &= (T_r - 2.4)/1.5 \\ b &= 6.293T_r^2 - 9.0433T_r + 2.9334 \quad \text{and,} \\ c &= 0.015T_r - 0.036 \end{aligned}$$

Finally, corrected binary diffusivity is $\mathscr{D}_m^{ij} = f(T_r, P_r)\frac{P_{atm}}{P}\mathscr{D}_0^{ij}$. It is to be noted that this model fails in the low-temperature and leading to negative values since the experimental data of Takahashi didn't include the same. However, the low-pressure diffusion model doesn't give any nonphysical values, but it does over-predict the diffusion coefficient.

4.3.4. Firoozabadi model

The work by Leahy-Dios and Firoozabadi [2007] formulated a new correlation (also known as the Yale model based on the university affiliation in the plots for the sake of simplicity) based on 889 experimental data. It was tested against the available multi-component models, namely Wile-Chang, Kooijman, Hayduk-Minhas, and Sigmund. The other Riazi and Whitson were not considered due to their lack of ability to model the multicomponent mixtures. The advantage of the correlation was that it takes composition dependence for the computation of the coefficient. The procedure and method are described in the appendix A.1.

4.3.5. Bellan's CSP model

Bellan's CSP model postulated by Harstad and Bellan [2004b]. It is a seminal work in computation of diffusivity in dense fluids. The method is based on the principle of corresponding states by computing accurate diffusivity in the kinetic theory regime, then translating the infinite dilution of dense gases using the formulae given below (4.14). The authors do discuss the failure of the classical Stokes-Einstein (SE) formula which are due to the following reasons,

- For the low-pressure liquids and liquid-like fluids, the effect of high-pressure can be included via the pressure correction
- For the computation of the dense gas diffusivity, SE formula is generally used for the apparent overlap of the reduced density between liquid and dense gas is a questionable assumption

The SE is expressed as,

$$\mathscr{D}_{ij}^0 = \frac{kT}{\eta_j \lambda_{ij}} \tag{4.14}$$

λ_{ij} is the characteristic scattering length and the source of a lot of deliberations since it involves the computation of surface tension. Still, authors do suggest a relation in terms of critical properties and species-dependent constant. Now in mitigating the issues mentioned above, they indicated that viscosity depends on ρ at high-pressures, but at low-pressure, it is very much dependent on temperature alone. Besides, at low-pressures, the Schmidt number is constant, implying that the mass diffusivity is directly proportional to the viscosity, not otherwise as suggested by the SE formula.

$$(\mathscr{D}_{ij})_{KT} = 2.81 \times 10^{-5} V[(m_i^{-1} + m_j^{-1})T]^{1/2} \frac{(T/T_{c,ij})^s}{[r_D(V_{c,ij})^{2/3}]} \tag{4.15}$$

$$w_{D,ij} = \frac{(\mathscr{D}_{ij})_{KT}}{(\mathscr{D}_{ij}^0)_{bellan}} \quad \text{where,} \quad w_{D,ij} \quad \text{is given by} \quad \delta_D = w_D - 1 \tag{4.16}$$

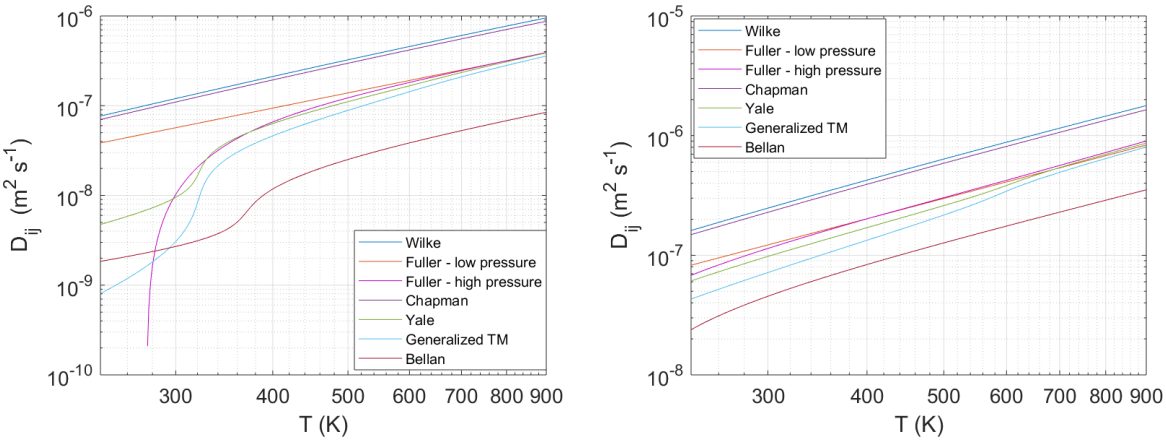

Figure 4.6: Left: diffusion coefficient of n-heptane in CO_2 at P = 1.05E7 Pa; Right: The diffusion coefficient of n-heptane in N_2 at P = 6E6 Pa.

The authors did emphasize on using kinetic theory diffusion formulae due to their high accuracy in low-pressure regimes. The δ_D is obtained from the relation $\delta_D = c\rho_r^b$, where c and b are obtained from the class of the solute and solvent. Also, except for the light gases, r_D can be taken as one, and this ansatz helps in assigning $w_D = 1$ at low pressures. The figure 4.6 shows the performance of various diffusion coefficient models of n-heptane in CO_2 at 1.05E7 and 6E6 Pa. The Generalized TM refers to Thermo-mechanical models of diffusion coefficient as in the work of Carreón-Calderón and Uribe-Vargas [2019], where the diffusion is computed via thermodynamic properties. In this work, the Yale model and Generalized TM model are preferred because of its convergence with the kinetic models in the high-temperature region.

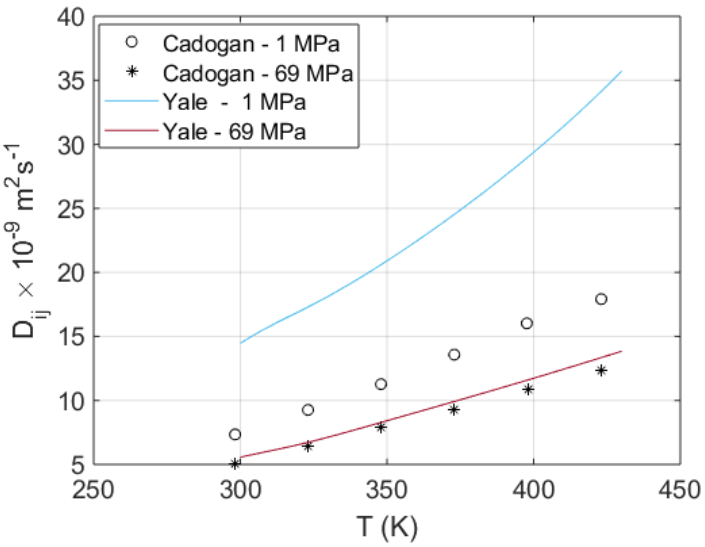

Figure 4.7: Diffusion coefficient of CO_2 in n-heptane

The Yale model shows good agreement with the experimental values as seen in figure 4.7. The experimental values of the diffusion coefficient CO_2 in n-heptane were obtained from the work of Cadogan et al. [2016].

4.4. Surface tension

As with the nature of this work, surface tension is an important aspect of the diffuse interface models, the common assumption of zero surface tension after the critical point as in the models of Bird (1955) and Sastri

(1995) from Poling et al. [2001] isn't reinforced in this work. The work of Crua et al. [2017] supplemented the idea of non-zero surface tension after the critical point. In this work, the surface tension model of Lee and Chien (1984) from the work of Pedersen et al. [2006] is utilized.

$$\sigma^{1/4} = P_L \rho_L - P_V \rho_V \tag{4.17}$$

where P_L, P_V, ρ_L, and ρ_V are the parachor of liquid, parachor of vapor, molar density (mol/cm^3) of liquid, and vapor. Parachor is a semi-empirical term that relates surface tension to the density of the species rather than the other conventional models where the surface tension is described with respect to the temperature. The idea of describing surface tension by density is more intuitive as the attractive force between the molecules decreases as the density reduces Macleod [1923]. Following the work of Macleod [1923], Sugden [1930] rearranged the terms and came to a derived function named parachor. Parachor's physical meaning has yet to be understood. Parachor has been conventionally defined as the molar volume of the component when the surface tension is 1. This term enables the comparison of the molecular volumes at constant surface tension instead of constant temperature. Interestingly, parachor is an additive component for most of the cases and weakly dependent on temperature. It is critical to note that the above-discussed model is quite efficient and precise but not as accurate as modules based on Linear Gradient Theory, Density Gradient Theory, and Density Functional Theory. From the figure 4.8, it clear that Lee and Chien does not give exact results but they tend follow the trend of the experimental values

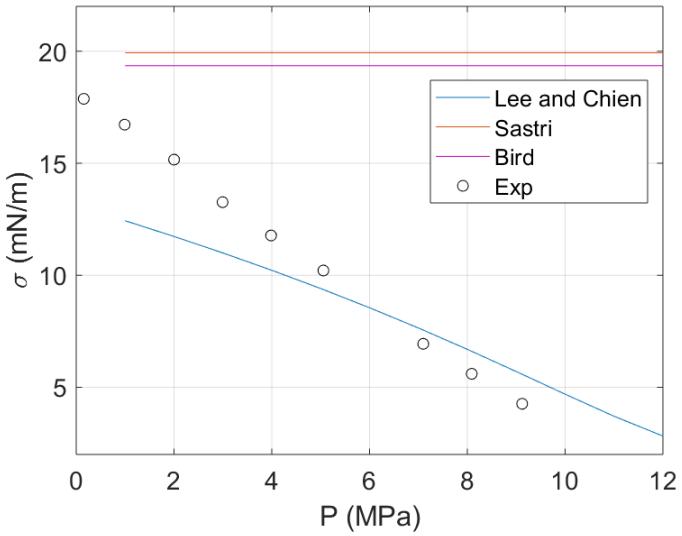

Figure 4.8: Interfacial tension values of n-decane CO_2 at 343.6 K, the experimental values are from Georgiadis et al. [2010]

4.5. Inferences

As discussed in previous sections, transport properties can be computed via three methods,

- Theoretical basis via kinetic theory e.g., Chapman-Enskog, Chung and so on.
- Corresponding states principle e.g., Pedersen CSP, TRAPP, entropy scaling and so on
- Link via thermodynamics e.g., Friction theory.

All the above methods use empirical data in one way or the other. The issue is at the dense fluid regime, the assumptions in the kinetic theory fails and hence better models for dense fluids are necessary. The shortcomings for the CSP model stems form the proper selection of the reference component e.g., few works recommend methane while other works recommend propane. This needs to be studied as the reference component needs to account for the translational and the internal modes of transfer. In conclusion, it can be said that there are specialized models for the viscosity and thermal conductivity, such as Pedersen's model and excess

entropy models. These models increase the computational load significantly, whereas the Chung's method for viscosity and thermal conductivity using PC-SAFT gives excellent results on par with the Pedersen's model and excess entropy model. As for the diffusivity models, any model that converges with the low-pressure fuller model in the kinetic region is advisable such as Firoozabadi model or Generalized thermo-mechanical model.

4.6. Recommendations

It would be interesting to observe the performance of viscosity and diffusivity using excess entropy models against these respective classical models and also the implementation of surface tension modules using LGT. As for the thermal conductivity of heptane, the work of Assael et al. [2013] is recommended as it has the most accurate model for the thermal conductivity of n-heptane for a wide range of conditions (182.56 K to 600 K up to 250 MPa). It certainly would be interesting to have corresponding states principle based on n-heptane (with the above model) as the reference component with residual entropy as the scaled property. Finally, the inclusion of bulk viscosity based on Boukharfane et al. [2019], Jaeger et al. [2018], and Billet et al. [2008] would certainly be of significant interest.

5

Interface Modeling

5.1. Level set method (LSM)

In level set methods, the interface is represented by the zero level function of the globally defined signed distance function (dist). They belong to implicit sharp interface class. The level set method takes the original interface and builds it into a surface. The shape of the interface (Γ) at that time is given by slicing the curve at zero height or at the zero-level set.

$$\phi = \begin{cases} dist(x,\Gamma), & \text{inside} \quad \Gamma \\ -dist(x,\Gamma), & \text{outside} \quad \Gamma \end{cases} \tag{5.1}$$

The conventional level set function without re-initialization advected by the velocity field is given by,

$$\frac{\partial \phi}{\partial t} + \mathbf{u} \cdot (\nabla \phi) = 0 \tag{5.2}$$

It may seem to be excessive to develop a surface to model the interface, but this helps in modeling the topological changes of the interface. COMSOL Multiphysics utilizes conservative LSM with phase-field function (Φ, not to be confused with phase-field parameter used in Phase-field methods). In C-LSM, all the thermo-physical properties are smeared over few cells with $0 \leq \Phi \leq 1$

5.1.1. Methodology

The crust of level set method is to define the interface implicitly by a regularized characteristic function ϕ which varies from 0 to 1 with $\phi = 0.5$ defined as the interface. The volume fraction of the nitrogen is set as the level set variable ϕ, since by default the component 2 is set as the level set variable. One of the major concerns in the implementation of LSM is the mass error which can be mitigated using a range of methods from advection schemes , reinitialization schemes to conservative schemes. The conservative level set equation employed in COMSOL is,

$$\frac{\partial \phi}{\partial t} + \mathbf{u} \cdot (\nabla \phi) = \gamma \nabla \cdot (\epsilon \nabla \phi - \phi(1-\phi)\frac{\nabla \phi}{|\nabla \phi|}) \tag{5.3}$$

The right-hand side of the above equation is for the numerical stability. The parameter ϵ determines the interface thickness, usually its better to have a grid dependent number. The γ is the amount of re-initialization required and it is equal to the maximum velocity in the model.

Re-initialization is required to maintain the signed distance property of the level set function. The advecting the interface results in inaccurate calculation of the interface and the thermo-physical property. There is a brute force method by computing the interface location and distance from the interface to all the points. This prohibitively computationally expensive. There is a PDE based re-intialization, but it moves the interface significantly and resulting in loss of mass. Finally, Olsson et al. [2007] postulated the equation 5.3.

In the level set approach, the surface tension is included in the body force terms and is obtained from the gradient of the level set function.

$$F_{st} = \sigma \delta \kappa \mathbf{n} + \delta \nabla_s \sigma \tag{5.4}$$

σ, δ, κ, $\mathbf{n}$, and ∇_s are the surface tension coefficient, Dirac-delta function, curvature, unit normal, and surface gradient operator respectively.

5.2. Theory of Diffuse Interfaces

Diffuse interface methods can again be classified into two classes,

- Phase-field formulation
- Numerically smeared interface

Phase-field is derived from the thought that all the processes of significant time scale in nature occur in order to minimize the free energy of the system. Phase-field models can be thought of physically motivated level set method via a consistent level set function called as the order parameter. In contrast to the level set methods where the surface tension is brought into the equations via the body force, in phase-field, it is implemented via the Korteweg stress tensor($\lambda\nabla\rho\nabla\rho$) (Jamet [1999]). If the concentration is used as a conserved order parameter, the equation governing the interfacial dynamics is equivalent to the generalized Fick's law.

Phase-field method models the interfacial dynamics using the free energy Gibbs or Helmholtz energy via the order parameter. The description of the interfaces is achieved via the order parameter, which varies rapidly but smoothly over the interface.

Phase-field methods can be further classified as,

- Navier-Stokes-Cahn-Hilliard (NSCH)
- Navier-Stokes-Korteweg (NSK)
- Navier-Stokes-Allen-Cahn (NSAC)

In NCSH, the free energy is given by the classical part of the energy and the gradient of the concentration/ mass fraction or any other unique parameter. The system of equations for NSCH with mass concentration (c) as the order parameter are,

$$\rho_0 \frac{\partial \mathbf{v}}{\partial t} + \rho_0 \mathbf{v} \cdot \nabla \mathbf{v} = -\nabla \tilde{P} + -\nabla \cdot (\lambda \nabla c \otimes \nabla c) + \nabla \cdot \boldsymbol{\tau} \tag{5.5}$$

Along with the Cahn-Hilliard equation namely,

$$\frac{\partial c}{\partial t} = \nabla \cdot [\kappa \nabla (\mu^0(c) - \nabla^2 c)] \tag{5.6}$$

For instance, take ϕ as the order parameter then the system of equations (for an isothermal system) are,

$$F(\phi) = \int_\Omega f(\phi(x)) + \frac{1}{2}\kappa |\nabla \phi(x)|^2 dx \tag{5.7}$$

Therefore, the chemical potential is given as, $\mu(\phi) = \frac{\partial F(\phi)}{\partial \phi(x)}$

$$\frac{\partial \phi}{\partial t} + \mathbf{u} \cdot \nabla \phi = \nabla \cdot (M(\phi) \nabla \mu) \tag{5.8}$$

M is the Mobility constant/ Onsager coefficient.

$$\rho\Big(\frac{\partial \mathbf{u}}{\partial t} + \mathbf{u} \cdot \nabla \mathbf{u}\Big) = -\nabla \cdot p + \nabla \cdot \eta(\nabla \mathbf{u} + \mathbf{u}^T) + \mu \nabla \pi \nabla \cdot \mathbf{u} = 0 \tag{5.9}$$

NSK follows from the work of van der Waals [1893], who concluded that the interfaces depend on local and as well as non-local quantities. This model includes the additional Korteweg ($\lambda\nabla\rho\nabla\rho$) stress term but also a peculiar form of the pressure as a function of the density (any other order parameter for that matter). The function $P(\rho)$ tends to sharpen the interface (with a zero-thickness interface if only this term is present in the momentum balance equation), and the Korteweg stress tensor tends to diffuse the interface.

$$\rho \frac{d\mathbf{v}}{dt} = \nabla P^0 + \nabla(\lambda \rho \nabla^2 \rho + \frac{\lambda}{2}(\nabla \rho)^2) - \nabla \cdot (\lambda \nabla \rho \otimes \nabla \rho) + \nabla \cdot \boldsymbol{\tau} \tag{5.10}$$

Many works do advise against using NSAC, at-least without special treatment, to ensure the conservation of mass in the interfacial region. The system of equations includes the Navier-Stokes equation coupled with the Allen-Cahn equation for the order parameter.

If the NCSH or NSK are utilized for modeling the interfaces, there's a need to enlarge the interface thickness artificially, and consecutively, expressions of the EoS are changed to make sure that the scaled interface doesn't affect the bulk properties. The whole crux of the model is that interface thickness is governed by numerical arguments rather than the physical arguments, i.e., interface thickness should be a free parameter. For instance, consider a generic NSK model where the thickness is given by the following term,

$$h = \frac{1}{\rho_l - \rho_v}\sqrt{\frac{\lambda}{2A}} \tag{5.11}$$

where λ is the capillary coefficient, A is the coefficient of free energy. Finally, ρ_l and ρ_v are densities of the liquid and gas components at the interface. It is interesting to note that from the above relation, λ is the only term which affects the interface affects the bulk quantities. To increase the interface thickness, the λ needs to be increased, which increases the surface tension, $\sigma = \frac{(\rho_l-\rho_v)^3}{6}\sqrt{2A\lambda}$.

Nomenclature in other relevant studies

As stated in the Chapter 2, few studies have modeled the liquid-vapor interface with Linear Gradient Theory, Density Gradient Theory, Density Functional Theory and so on. The fundamental differences between the DGT and DFT are,

- DFT is purely predictive whereas the DGT requires correlation terms.
- In DGT, the local Helmholtz energy density is obtained by the local density approximation where the terms subsequent to the square density gradient terms are neglected. The correlation is applied to the prefactor of the square density gradient term.
- In DFT, the total Helmholtz energy is obtained from the EoS using the perturbation theory i.e., in DFT the free energy of the inhomogeneous fluid is given by just by the $\rho(r)$. DFT is rightly viewed as the generalized version of DGT method of van der Waals.

5.2.1. Methodology

For interface modeling, the formulation similar to the work of Guo and Lin [2015], namely Yue et al. [2006] was utilized. For binary fluids, the concentration of the fluid is a more consistent parameter since the solubility of the components is an important phenomenon after the critical point. Also, having the density as an order parameter might lead to spurious results if there is a density gradient in the bulk of the flow. The diffuse interface is achieved via the phase-field modules in the COMSOL Multiphysics. The interface is described by the free energy by the following relation,

$$f_{mix}(\phi, \nabla\phi) = \frac{\lambda}{2}|\nabla\phi|^2 + f_0(\phi) \tag{5.12}$$

$$\text{The classical free energy is,} f_0 = \frac{\lambda}{4\epsilon^2}(\phi^2 - 1)^2$$

The governing equations of the phase-field equations with scaled volume fraction ϕ, as the order parameter are,

$$\frac{\partial\phi}{\partial t} + \mathbf{u}\cdot(\nabla\phi) = \nabla\cdot\frac{\gamma\lambda}{\epsilon^2}\nabla\psi \tag{5.13}$$

$$\psi = -\nabla\cdot\epsilon^2\nabla\phi + (\phi^2 - 1)\phi + \left(\frac{\epsilon^2}{\lambda}\right)\frac{\partial f_{ext}}{\partial\phi} \tag{5.14}$$

$$\sigma = \frac{2\sqrt{2}}{3}\frac{\lambda}{\epsilon} \tag{5.15}$$

λ, ϵ and γ corresponds to the energy density parameter (capillary coefficient), interface width, and the mobility parameter. These variables are characteristic of the phase-field models. Mobility is computed from the mobility tuning parameter, which determines the time scale of the Cahn- Hilliard diffusion. An increase in

mobility favorably affects the time taken for the system to reach equilibrium and thereby to lead to thinning or thickening of interfaces.

$$\text{Mobility tuning parameter,} \quad \chi = \frac{Uh_{max}}{3\sqrt{2}\sigma\epsilon} \tag{5.16}$$

$$\text{Mobility,} \quad \gamma = \chi\epsilon^2 \tag{5.17}$$

Finally, the density and dynamic viscosity are defined as,

$$\rho = \rho_1 + (\rho_2 - \rho_1)V_f \tag{5.18}$$

$$\mu = \mu_1 + (\mu_2 - \mu_1)V_f \tag{5.19}$$

The volume fraction of the two components is given by, $V_{f1} = \frac{1-\phi}{2}$ and $V_{f2} = \frac{1+\phi}{2}$. The surface tension is one of the distinctive features of phase-field methods. In the phase-field models, the surface tension is modeled as a body force in the Navier-Stokes equation,

$$F_{st} = \Big(\mu - \frac{\partial f}{\partial \phi}\Big)\nabla\phi \tag{5.20}$$

$$\mu = \lambda\Big(-\nabla^2\phi + \frac{\phi(\phi-1)}{\epsilon^2}\Big) + \frac{\partial f}{\partial \phi} \tag{5.21}$$

where μ is the chemical potential (J/m^3). The above equations are solved along with the continuity, Navier-Stokes, and conservation of energy. In this work, NSCH is preferred over the NSK due to the binary species in the vapor phase. This method of surface tension definition eliminates the tedious process of computing the surface normal and the curvature of ϕ

6

0-D studies on evaporation of droplets

For better understanding of interaction of the droplets, they were studied in a series from 0-D to 3-D. This chapter exclusively deals with the study of droplets in 0-D.

6.1. Test cases

The 0-D models were mainly based on the work of Kadota and Hiroyasu [1976] and Sánchez [2012]. The former studied the vaporization of n-heptane computationally and experimentally in high temperature and high pressure conditions (ranging from 373 K to 773 K and 0.1 MPa to 5.1 MPa respectively). They used RK-EoS for fugacity computations and all other thermo-physical properties (density, heat capacity, thermal conductivity, diffusivity and viscosity) were based on the fifth-order polynomial from an experimental database. All the experiments were conducted for stationary droplets under gravity.

This work was also validated the results against the results of Sánchez [2012]. They studied the vaporization of droplets using Abramzon-Sirignano (AS) model for n-heptane and kerosene. They improved the accuracy of the model by working on new constant Prandtl number and Schmidt number for conditions of interest. They computed the transport properties in a simplified manner, using constant non-dimensional numbers.

Transport properties		
Name	Pr	Sc
ievap 21	0.82536	1.4807
ievap 11	0.71	2.10
ievap 01	variable via CANTERA	variable via CANTERA

Table 6.1: Non-dimensional numbers for transport properties for Sanchez's test case

6.2. Governing equations

Two equations accounting for the variation of diameter and temperature were solved temporally. The dissolution of nitrogen into heptane was also included by the ratio of mass flux of nitrogen and mass flux of heptane. As for the heptane, a simple system of equations was utilized.

$$\frac{dT_l}{dt} = \frac{1}{mC_{p,l}}(Q_d + L\frac{dm}{dt}) \tag{6.1}$$

$$\frac{dD_l}{dt} = \frac{2}{\pi D_l^2 \rho_l}(\frac{dm}{dt} - \frac{\pi D_l^3}{6}\frac{d\rho_l}{dT_l}\frac{dT_l}{dt}) \tag{6.2}$$

where $\frac{dm}{dt} = \pi D_l^2 k^* \frac{y_{A0}-y_{A2}}{1-(1+\zeta)y_{A0}}$ and

$$\zeta = -\frac{\rho_g(1-y_{A0})}{\rho_l + \frac{r_l}{3}\frac{d\rho_l}{dt}/\frac{dr_l}{dt}}.$$

where T , ρ, m, C_p, L, D_l, k^*, h^*, r_l and ζ corresponds to temperature, density, mass of the droplet, specific heat, latent heat, diameter of the droplet, corrected coefficient of mass transfer, corrected coefficient of heat transfer, radius of the droplet and dissolution rate. The subscript l, g and A0 corresponds to liquid, gas and droplet surface respectively. The corrected coefficient of mass transfer (k^*) and corrected coefficient of heat transfer (h^*) are corrected for the high mass and heat transfer. Corrections to heat transfer and mass transfer are done because of the simultaneous mass transfer and heat transfer with the following,

$$h^* = \xi_T h \tag{6.3}$$

$$k^* = \xi_M k \tag{6.4}$$

The coefficient of mass transfer (k) is given by the expression, k = $\frac{\rho \mathscr{D} Sh}{D_l}$ where $Sh = 2 + 0.6Gr^{0.25}Sc^{0.333}$ with the Grasshof number being $\frac{g(\rho_{sf}-\rho_\infty)D_l^3}{\rho_\infty \nu_\infty^2}$ rather than the conventional $\frac{g\beta(\Delta T)D_l^3}{\mu}$. Since, the latter's Boussinesq approximation of density in terms of a linear relation is questionable at-least for the conditions under study, and this observation was validated by the study Gogos et al. [2003].

The coefficient of mass transfer (h) being $h = \frac{\lambda Nu}{D_l}$ where $Nu = 2 + 0.6Gr^{0.25}Sc^{0.333}$. where, $\xi_T = \frac{z_t}{exp(z_t)-1}$ and $\xi_M = \frac{z_m}{exp(z_m)-1}$.

All the transport and thermodynamic properties for the correlations are computed at the boundary layer utilizing the 1/3rd rule. The 1/3 rd rule is $T_{sf} + \frac{1}{3}(T_\infty - T_{sf})$. It is done as to take the effects of the ambient temperature into account for the computation of the boundary layer. It is very much an ad-hoc implementation as there are no exact expression. It is significant to note that Kadota and Hiroyasu [1976] uses abstract boundary layer thickness for the computation of the effective heat transfer and mass transfer coefficient instead of transfer coefficients at low-mass and heat-transfer rates as given in the book by Bird et al. [1961]. The terms z_m and z_T are given in the work of Jin and Borman [1985].

Finally, the heat transfer due to the convection is given by,

$$Q_d = \pi D^2 h^* (T_{infty} - T_l) \tag{6.5}$$

This system of equations is well suited for elevated pressures and temperatures as,

- Latent heat of vaporization isn't constant. It is computed from the enthalpy of the vapor and liquid components to account for pressure effects on the same.
- The mass fraction of n-heptane is computed from the iterations from the COMSOL application, i.e., $f_i^l = f_i^v$ or by the Poynting factor.
- Higher-order EoS is utilized, which is very much suited due to the operating conditions under study.

As for the computation of the diffusivity of the gas using ($\mathscr{D}$) fuller's method and Chapman were utilized in the validation studies. At high pressures, the Takahashi's high-pressure correction was implemented for Fuller's diffusion model by Palle et al. [2005].

The work by Ma [2016] enforces confidence in the system of equations. The author worked on the modeling of turbulent combustion. They utilized the correlations comparable to this work with the difference being Reynolds number in the Nusselt number formulation. The author direct the existence of two formulations for the simultaneous heat and mass transfer coefficients namely

- Bird's formulation
- Abraham's formulation

They investigated both the models and concluded that the latter model takes more computing resources compared to the former one. The difference in accuracy between the models is negligible. This work also throws light on the weighted averages and its significance on the evaporation. The author recommends 1/3rd rule as the increasing the weighted factor increases the evaporation rate. The role of the weighted factor in droplet evaporation was studied. It was concluded that it is of significance only when the ambient and droplet surface temperature varies significantly, such as the conditions in the combustors, unlike the conditions of this study, Chauveau et al. [2008], and Kadota and Hiroyasu [1976].

6.2.1. Discrepancies

In the work of Kadota and Hiroyasu [1976], the simultaneous heat and mass transfer are modeled by assuming an abstract boundary layer, which in turn requires abstract magnitude which quantifies the importance of the heat/ mass transfer (usually taken as 1). During the validation of the Kadota test case, the above-mentioned method was utilized, and in the other studies, the principle prescribed in Bird et al. [1961] was used. An important barrier in replicating the results of Kadota and Hiroyasu [1976] is the absence of a description of the transport properties employed in the study. It is also important to note that the density and heat capacity were based on the fifth-order polynomial rather than the RK method that was used for the fugacity computations.

6.3. Results

6.3.1. Sanchez's test case

Sánchez [2012] studied the effects of the various assumptions such as the Prandtl number and Schmidt number for the computation of the transport properties. They compared against the experimental data of Nomura et al. [1996] and Yang and Wong [2002] for validating the work. The Sanchez's results were in good agreement with the Yang's data and the droplet lifetime increases. The results in this study aren't in good agreement with experimental data in the low conditions (ambient pressure of 1 bar and 5 bar). The accuracy of the models in the moderate to high-pressure regimes are in excellent agreement with the experimental results. The Nomura results are actively contested in the community, as they moved the droplet to a study area thereby leading to forced convection effects to the heat transfer and finally, they utilized a fibre of significant thickness to hold the droplet leading to heat transfer via the fibre therefore Yang studied the droplet vaporization at same conditions but corrected for effects of fibre conduction and radiative heat transfer. The Nomura results are also studied in the next chapter.

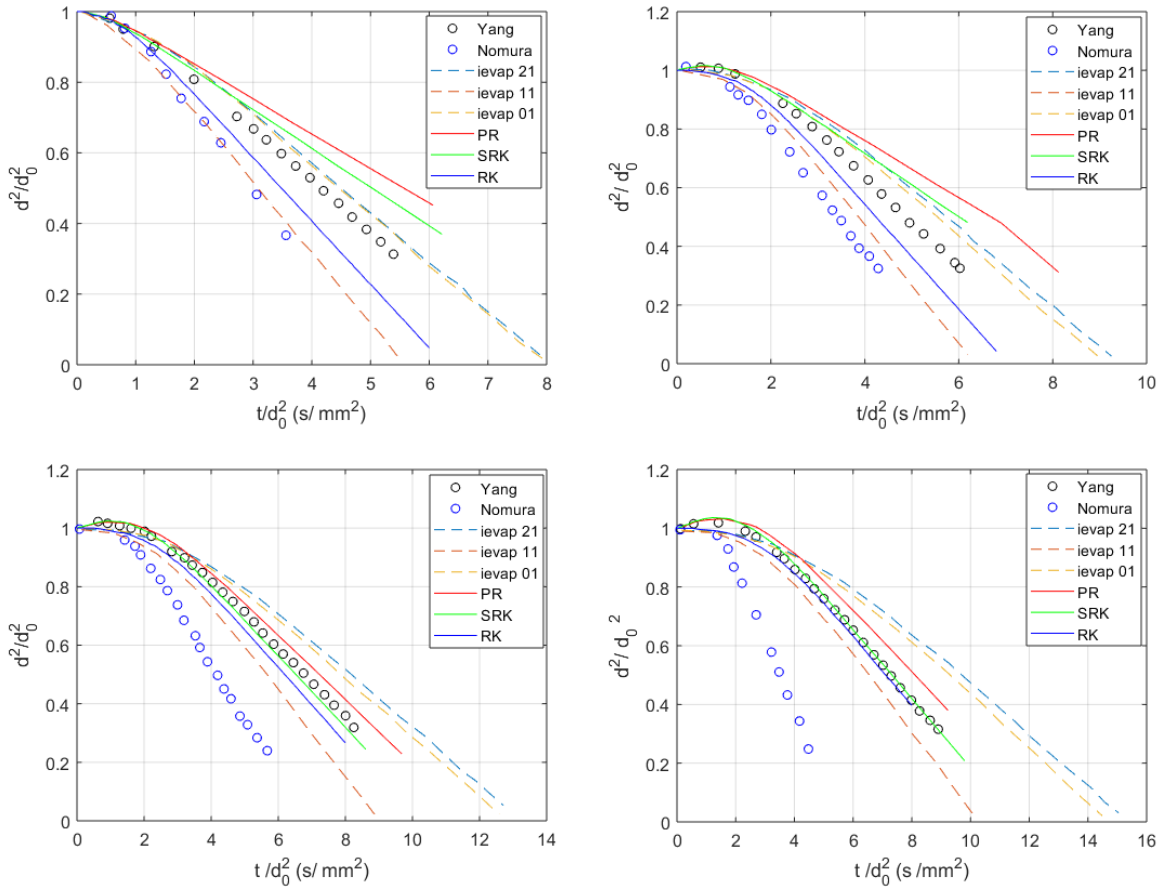

Figure 6.1: Top-left: non-dimensional diameter vs. scaled time (t/d_0^2, s/mm^2) at P = 1 bar; Top-right: non-dimensional diameter vs. scaled time (t/d_0^2, s/mm^2) at 5 bar; Bottom-left: non-dimensional diameter vs. scaled time (t/d_0^2, s/mm^2) at 10 bar; Bottom-right: non-dimensional diameter vs. scaled time (t/d_0^2, s/mm^2) at 20 bar, Sánchez [2012]

Test case	PR	SRK	RK
1 bar	10.82%	7.65%	-10.89%
5 bar	10.84%	7.76%	-9.01%
10 bar	2.90%	-1.74%	-4.14%
20 bar	5.47%	0.54%	-1.37%

Table 6.2: Mean percentage errors for different EoS for Sanchez's test case

The droplet's lifetime of Sanchez's test case is illustrated in fig. 6.1 at P = 1 bar, 5 bar, 10 bar, and 20 bar respectively. It is evident that the droplet's lifetime increases as pressure increases which can be attributed to the combined effects of increased boiling point of the component and decreased mass diffusion coefficient.

6.3.2. Kadota's test case

Kadota and Hiroyasu [1976] studied the effects of different modes of heat transfer in the droplet vaporization in high pressures and high temperatures both experimentally and numerically. As seen from the figure 6.2, the results are in good agreement with the experimental results at low and moderate pressures. The work of Kadota reports that the droplet size decreases slightly initially and then it follows a linear trajectory whereas in this work, the initial heating period leads to the expansion of the droplet as noted in other studies such as Sánchez [2012]. Kadota and Hiroyasu [1976] states that the lifetime of the droplet decreases with the increase in pressure at high temperatures which is also consistent with this work's results as evidenced in fig.6.2.

The dissolution of nitrogen into the droplet for the SRK EoS model for the conditions under study is shown the fig. 6.3. Consistent with the conventional wisdom, it is negligible at low temperatures and low pressures and significant, albeit in the heating phase of the droplet.

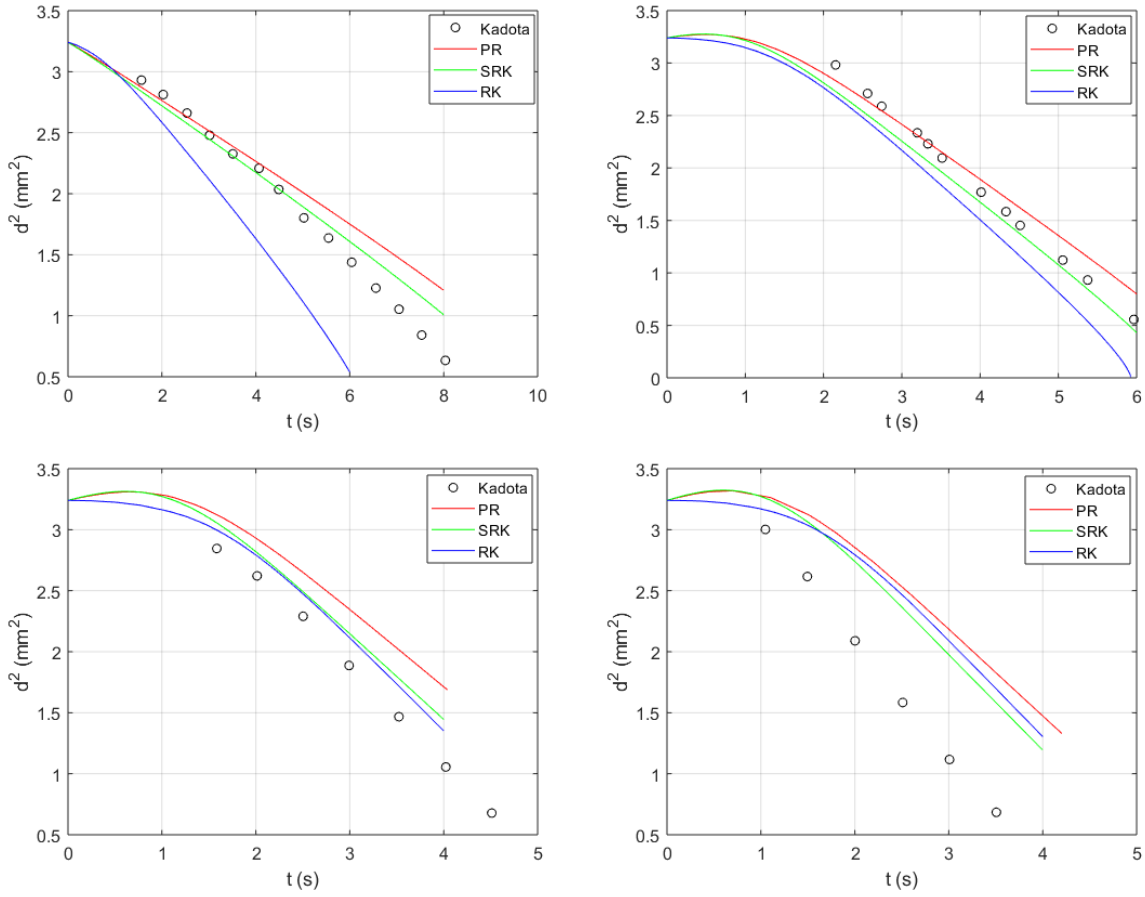

Figure 6.2: Top-left: Diameter squared vs. time at P = 0.1 MPa; Top-right: Diameter squared vs. time at P = 1.1 MPa; Bottom-left: Diameter squared vs. time at P = 3.1 MPa; Bottom-right: Diameter squared vs. time at P = 5.1 MPa respectively at constant ambient temperature of 573 K for Kadota test case

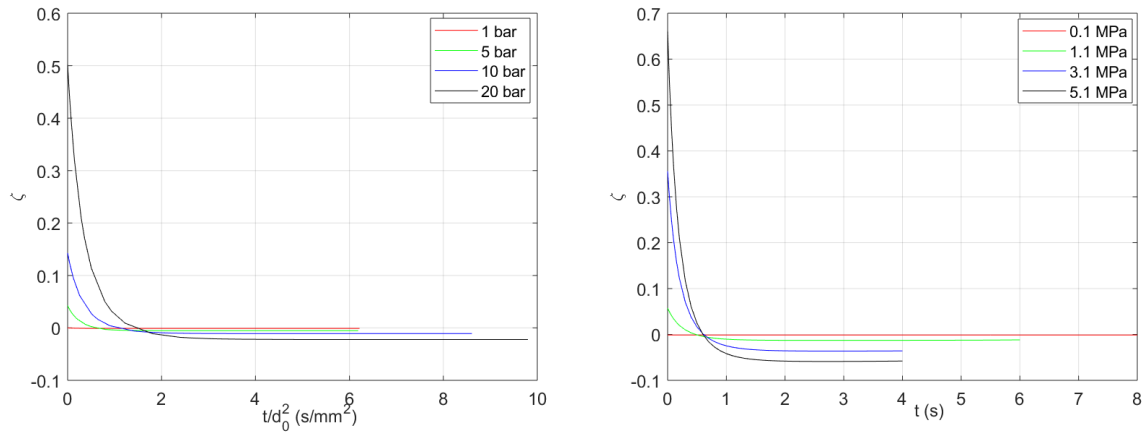

Figure 6.3: Left: The ratio of mass flux of nitrogen and n-heptane for Sanchez's test case by SRK EoS; Right: The ratio of mass flux of nitrogen and n-heptane for Kadota's test case by SRK EoS

Test case	PR	SRK	RK
0.1 MPa	5.97%	2.86%	-8.23%
1.1 MPa	4.16%	-4.2%	-8.75%
3.1 MPa	10.49%	4.05%	3.38%
5.1 MPa	26.60%	22.27%	24.09%

Table 6.3: Mean percentage errors for different EoS for Kadota's test case

As to reduce the computational load, an interpolation from a lookup table is computed for the VLE calculations for binary mixtures. The table is computed via a MATLAB script using fsolve command. Very few differences between the interpolation and the on-line VLE calculations were observed. The interpolation is better suited because the on-line VLE causes numerical instability for certain temperatures at high pressures. The fig.6.4 illustrates the differences in the computation of the droplet's lifetime with and without interpolation for the VLE for Kadota's test case. Minimal deviations are observed only in the PR-EoS. It is not shown for the RK-EoS since COMSOL doesn't have RK-EoS in their predefined modules.

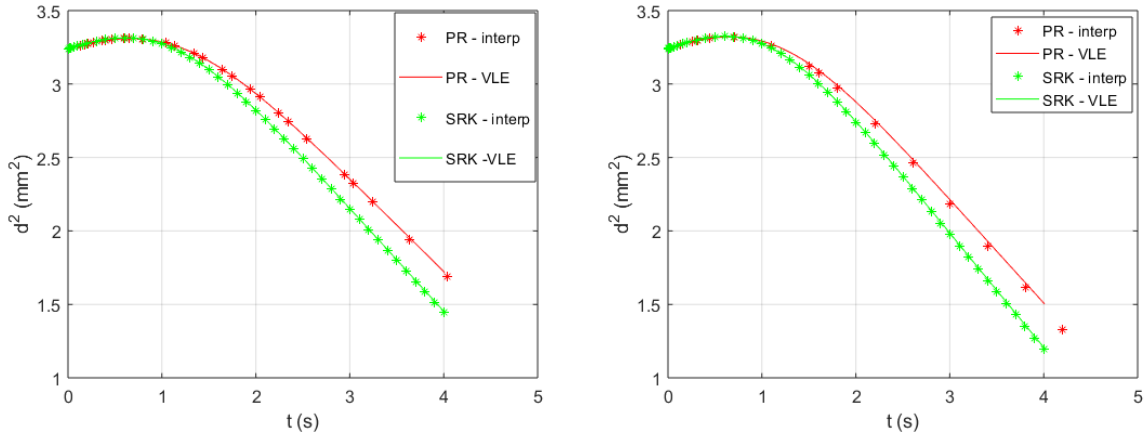

Figure 6.4: Left: Diameter squared vs. time at P = 3.1 MPa; Right: Diameter squared vs. time at P = 5.1 MPa at ambient Kadota and Hiroyasu [1976]

6.4. Conclusions

From the above results, it is clear that the performance of SRK is better than the PR for the study of the evaporation of droplets under the prescribed conditions.

It is interesting to note that Sánchez [2012] did not consider the effects of the dissolution of nitrogen into the droplet. The authors attributed the deterioration of the results in high-pressure conditions to the lack of real-gas effects on the VLE, dissolution of the nitrogen in the droplet, and ignoring the effects of gravity in the Grasshof number. The experiments of Yang and Wong [2002] and Nomura et al. [1996] were undertaken in the microgravity conditions to augment the spherical geometry assumption. This work considers the effects of gravity, real-gas effects, and the dissolution effects; hence the results are in very much in agreement with the experimental values. The discernible differences in accuracy stems from the computation of the latent heat of vaporization as shown in the appendix A.6.

7

1-D studies on evaporation of droplets

In this study, spray formulation Ma [2016] was utilized for the 1-D modeling; namely, the liquid properties were computed using the 0-D modeling approach. Initially, full 1-D equations were investigated for its application. However, in the thesis but due to a difficulty in the implementation of the boundary condition, it was discontinued. Hence, a numerical model similar to the work of Ebrahimian and Habchi [2011] was developed. For the 1-D validation, the work of Subashki [2016] was utilized. This work models the effect of convective stream using the Nusselt number and Sherwood number correlation from the work of Patel [2018]. For the droplet properties, the models discussed in previous chapters were used.

7.1. Test cases

The two formulations primarily used for this work are Ebrahimian and Habchi [2011] and Subashki [2016]. The former's solution strategy was used and was compared against the latter. Ebrahimian and Habchi [2011] conducted a numerical work studying the vaporization of mono-component and multi-component stagnant droplets at all pressures. They invoked biot number assumption (infinite liquid thermal conductivity assumption) for the liquid phase and solved the conservation of species, mass, and internal energy for the gas phase. They closed the equations with perfect-gas and real-gas EoS (PR). As for the components they investigated, it was n-heptane and n-decane in mono-component section and a mixture of n-heptane, n-decane and nitrogen for the multi-component section. This work included two central phenomenon in the droplet evaporation,

- Simplified Stephen velocity expression in consistence with the gas mass conservation
- Heat flux due to species diffusion

They utilized the Kulmala & Vesala correlation for the Nusselt number and Sherwood number contrary to the Ranz-Marshall correlation used in this work for stationary droplets. As for the Grashof number, the Boussinesq approximation was used.

All the thermodynamic and transport properties were obtained from the fitted data. They validated the data for the 1-D model against the work of Chauveau et al. [2008]. They tested their model against the 1989 Abramzon and Sirignano model.

The validation work was of Subashki [2016], where stagnant n-heptane was studied. They validated their results against Nomura et al. [1996]. Subashki solved the full 1-D governing equations utilizing a finite difference scheme for a non-isothermal transient profile. They investigated the role of Lewis number in the droplets vaporization. They ignored the Soret and Dufour effects. The author studied the rate of increase in droplet temperature. Initially, it increases rapidly and then gradually till the saturation temperature is reached. The authors studied the effect of Lewis number where Le < 1 corresponds to the mass-diffusion dominated regime while for Le > 1 corresponds to thermal-diffusion dominated vaporization resulting in relatively faster droplet heating. As for the thermo-physical properties,

- NIST RefProp database for the computation of thermal conductivity, density, and specific heat was utilized.

- Fuller's model, along with high-pressure Takahashi correction, was utilized.

They supplemented the model with the 1D governing equations and finally simulated the spray calculations using the information from the 1D equations in the form of corrected d2-law, where the diameter of the droplet is given by a function of temperature. The droplet was considered to be an isothermal point with the Nusslet and Sherwood numbers provided by Ranz and Marshall. The authors do note the limitation of ANSYS Fluent that PR-EoS can only be used for discrete particles. Finally, they studied the evaporation of the non-convective droplet by applying the relative velocity as 0 with the individual velocity of the droplet and nitrogen set to 2 m/s.

7.2. Governing equation

The assumptions used in this work are,

- The Biot number of the system under study is less (O (-1)); hence the assumption of time-varying uniform liquid temperature is justified.
- Fick's law of diffusion is utilized for modeling of the diffusion of the species. The second-order effects, such as Soret and Dufour are neglected for this 1-D model.
- The liquid component is assumed to be a single component and the gaseous to be a mixture of n-heptane and nitrogen.
- Viscous dissipation, chemical kinetics, and radial velocity effects are ignored.
- Higher-order EoS is utilized for closing the system of equations such as PR, SRK, RK, and PC-SAFT.
- The effect of gravity is neglected for the convective case, while for a stagnant case, the effect of gravity in natural convection is modeled via Grasshof number.
- High-pressure effects such as solubility of inert gas into the droplet are modeled in the droplet film.

The following system of equations is solved in the spherical coordinates for the gas phase properties.

$$C_p \rho r^2 \frac{\partial T}{\partial t} - \frac{\partial}{\partial r}\left(r^2 \lambda \frac{\partial T}{\partial r}\right) = -r^2 \sum_i \frac{\partial \overline{h}_i}{\partial r} \frac{J_i}{M_i} \tag{7.1}$$

$$\rho r^2 \frac{\partial Y_F}{\partial t} + Y_F \frac{\partial \rho r^2}{\partial t} - \frac{\partial}{\partial r}\left(\rho D_{12} r^2 \frac{\partial Y_F}{\partial r}\right) = 0 \tag{7.2}$$

where T, C_p, ρ,r, λ, $\overline{h}$, J_i,and Y_F corresponds to temperature, specific heat, density, radial distance, thermal conductivity, partial molar enthalpy of the species, mass flux ($-\rho D_{ij} \frac{\partial Y_F}{\partial r}$) and mass fraction. The energy equation in terms of temperature is used rather than the energy equation in enthalpy. The last term in equation 7.1 corresponds to the diffusion of enthalpy, which accounts for the energy changes stemming from the species diffusion (Cook [2009]). It is quite significant in the system of varying molecular weights, but in this case, it was found to be very minimal. The liquid properties were computed by the equations discussed in the previous chapter.

The following Nusselt and Sherwood number correlations are used for 1-D models,

- Kulmala & Vesala correlation
- Ranz-Marshall correlation

Ranz-Marshall correction is given by,

$$Nu = 2 + 0.6 \times (Gr)^{1/4} \times Pr^{1/3} \tag{7.3}$$

$$Sh = 2 + 0.6 \times (Gr)^{1/4} \times Sc^{1/3} \tag{7.4}$$

Kulmala & Vesala correlation is given by,

$$Nu = 2.0009 + 0.514\Big(max\big(Re, max(Gr,0)^{1/2}\big)\Big)^{1/2} Pr^{1/3} \tag{7.5}$$

$$Sh = 2.0009 + 0.514\Big(max\big(Re, max(Gr,0)^{1/2}\big)\Big)^{1/2} Sc^{1/3} \tag{7.6}$$

The 1/3rd rule is utilized for the computation of the transport properties and so on for the subsequent computations of the non-dimensional numbers. Because of the relatively low pressure, Chapman's diffusivity model is utilized. As for the viscosity Pedersen CSP and the kinetic theory for the thermal conductivity are used, the accuracy of the thermal conductivity in the conditions under study is excellent.

7.3. Results

7.3.1. Subashki's case

The results were compared to the results published in the work of Subashki [2016]. The author validated his numerical model against the Nomura et al. [1996]. The results of Nomura are quite contested in the community because of the additional heat source in the experimental setup. The authors used relatively big fiber to suspend the droplet in the nitrogen environment (0.150 mm). The other works, such as Yang and Wong [2002] and Chauveau et al. [2008] suggest the big fiber leads to an additional heat source from the fiber to the droplet, thereby leading to increased evaporation rate and shorter droplet lifetime. Gogos correction is shown in the appendix A.8 which accounts for the discrepancies in the experimental setup. Figure 7.1 shows the droplet lifetime of n-heptane in nitrogen at various conditions.

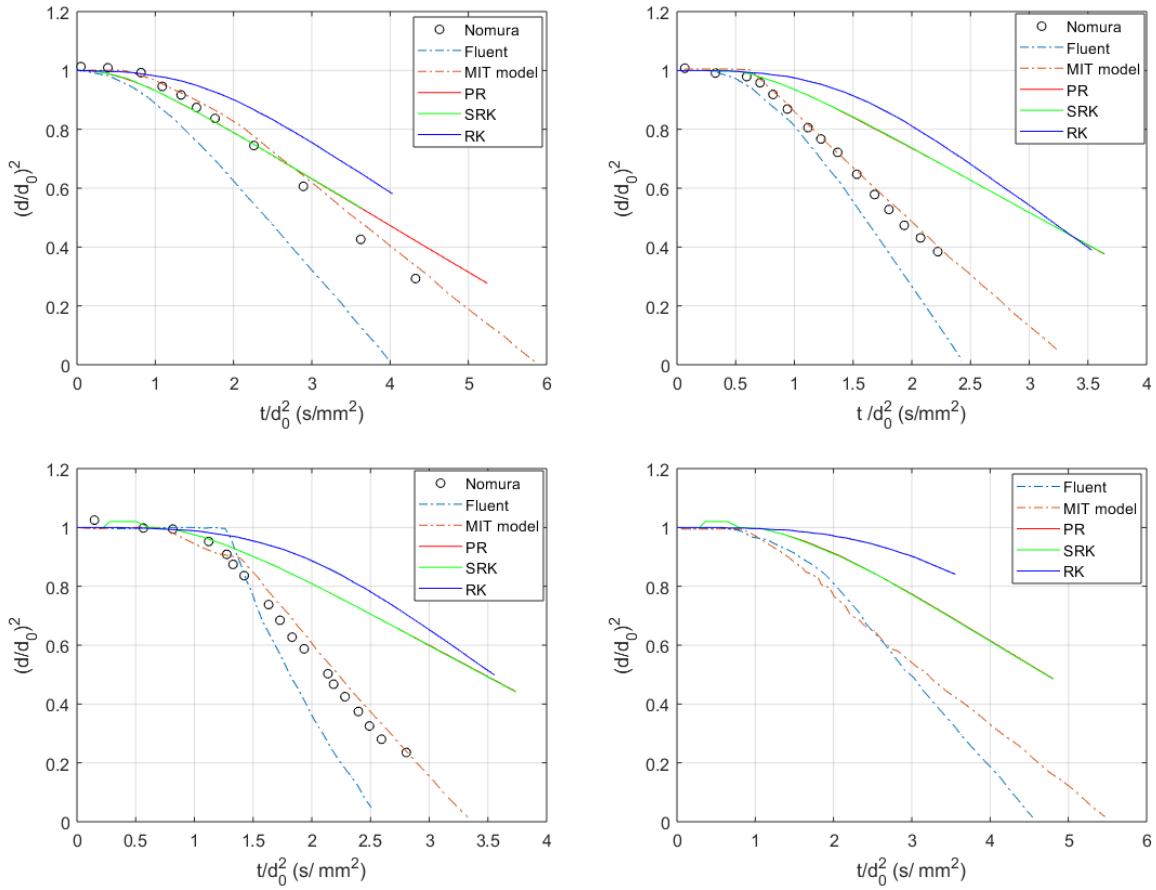

Figure 7.1: Top-left: Droplet lifetime of n-heptane in nitrogen at 5 atm and 556 K; Top-right: Droplet lifetime of n-heptane in nitrogen at 10 atm and 669 K; Bottom-left: Droplet lifetime of n-heptane in nitrogen at 20 atm and 656 K; Bottom-right: Droplet lifetime of n-heptane in nitrogen at 30 atm and 567 K

Test case	PR	SRK	RK
5 atm	2.44%	0.74%	5.64%
10 atm	11.59%	11.63%	14.93%
20 atm	20.04%	20.03%	24.30%

Table 7.1: Mean percentage errors for different EoS for Subashki's test case

7.3.2. Ebrahimian's case

The results of the developed model were in good agreement with the experimental results of Chauveau et al. [2008], which utilized a thin fiber to minimize the heat conduction from the fiber to the droplet along with a unique fiber geometry. It is interesting to note that even after neglecting the Stephen velocity in the model developed in this work, the results are very promising. It is evident that not all the EoS perform well with the accuracy in the following descending order SRK, PR, and RK. It is consistent with the previously observed 0-D results, where SRK did better than the PR. From the work of Ebrahimian and Habchi [2011], it is very evident that the density model doesn't vary the predictions significantly. Still, the differences between the different EoS can be attributed to the differences stemming from the latent heat of vaporization. The figure 7.2 shows the droplet lifetime of n-heptane in nitrogen at various temperatures with pressure set at 0.1 MPa.

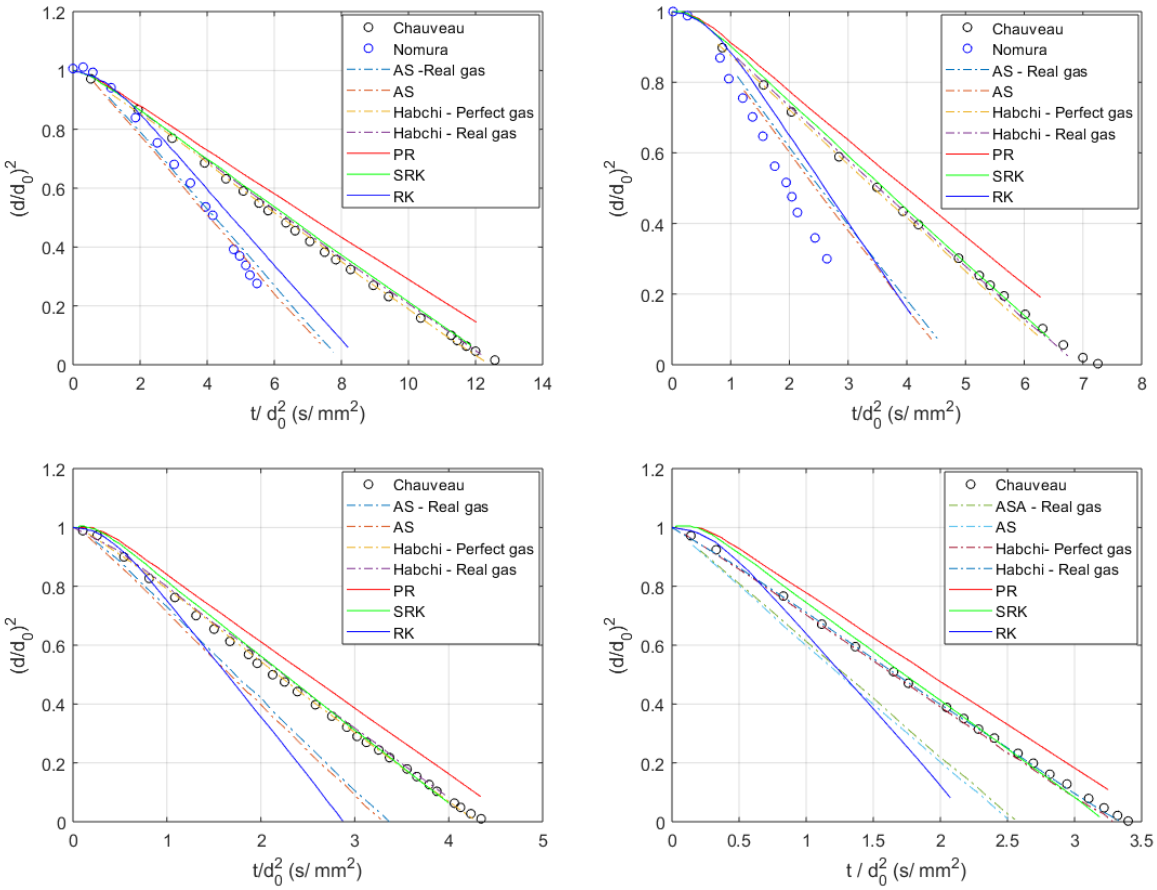

Figure 7.2: Top-left: Droplet lifetimes of n-heptane in nitrogen at 0.1 MPa and 473 K; Top-right: Droplet lifetimes of n-heptane in nitrogen at 0.1 MPa and 623 K; Bottom-left: Droplet lifetimes of n-heptane in nitrogen at 0.1 MPa and 823 K; Bottom-right: Droplet lifetimes of n-heptane in nitrogen at 0.1 MPa and 973 K

Test case	PR	SRK	RK
473 K	14.58%	3.65%	-17.04 %
623 K	14.58%	0.02%	-13.60%
823 K	17.82%	1.01%	-16.34%
973 K	14.58%	-2.39%	-15.15%

Table 7.2: Mean percentage errors for different EoS for Ebrahimian's test case

7.4. Conclusions

Some of the critical inferences from the above studies are that at low-pressure, perfect gas EoS is sufficient along with a consistent heat of vaporization module. As the pressure increases, the SRK is more suited to the modeling of the thermodynamic properties due to its inherent predicting capabilities. From the Figure 7.3, the two regime of droplet evaporation is discernible. The initial heat-up/cool-down period until the wet-bulb temperature (T_{wb}) and the latter asymptotic period where a constant temperature is reached. It is evident that the initial temperature affects the time for the droplet to reach the wet-bulb temperature (T_{wb}) and the ambient temperature (T_{∞}) affects the wet-bulb temperature (T_{wb}) of the droplet.

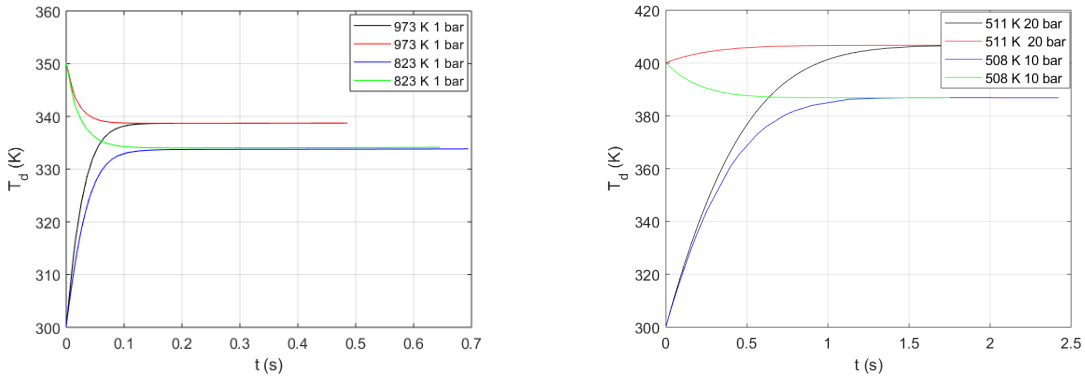

Figure 7.3: Left: Droplet temperature of n-heptane in nitrogen by 1-D model at different droplet temperatures and initial temperatures; Right: Droplet temperature of n-heptane in nitrogen by 0-D model at different droplet temperatures and initial temperatures

8

3-D studies on evaporation of droplets

This chapter deals with the evaporation of droplets using level set and phase-field methods via COMSOL Multiphysics. For the validation of the numerical model, the experimental work of Crua et al. [2017] work is utilized. A similar work in the field of diffuse-interface was conducted by Rainer et al. [2013] but the authors studied the Spray- A configuration. They used a 32 m-BWR EoS with Linear Gradient Theory (a later study included the Cahn-Hilliard equation) for the spatial distribution of the compositions across the interface.

8.1. Test cases

There's no 3-D phase-field droplet vaporization is available. Therefore, all the results are qualitatively compared. The results are compared for the experimental work of Crua et al. [2017] and a numerical work by Ping et al. [2019].

Studies in the vaporization at microscopic scales for the transcritical conditions are nearly non-existent except for the notable work of Crua et al. [2017]. This study visualized the three different vaporization regimes,

- Classical vaporization : This process is well known and characterized with continuous and progressive heat and mass transfer. The droplets maintain their spherical shape signalling the presence of surface tension. This process takes place when the time taken to vaporize is smaller than the timescale to reach the supercritical state.

- Translational vaporization: This regime starts off as a classical vaporization but soon they exhibit rapid deform deformation leading to increase in surface area of the droplet culminating in accelerated vaporization. The deformation can be attributed to the overcoming of the surface tension by the aerodynamic forces. The disintegration initiates at the wake side leading to a backward facing bag. The reason for the initiation at the wake is due to the thermal Marangoni forces since the surface tension is weaker in the wake due to relative high temperature of the wake. The authors also insisted on the intriguing characteristic of the multicomponent fuels stemming from the solutal Marangoni effects.

- Diffusive mixing: This is a very interesting vaporization regime where the sharp liquid-vapor interface becomes diffuse without any significant surface tension. The authors postulate this process as a single-phase two-fluid diffusive mixing. The timescale of transition from classical to diffusive mixing is around $1ms$ which is of significance when compared to the timescale in spray mixing. The droplets cannot be assumed to be spherical and the assumption of two-phase flow is limited for a short timescale.

There has been a recent numerical work by Ping et al. [2019] complementing the experimental campaign of Crua et al. [2017]. They utilized real-fluid and 4 equation homogeneous equilibrium model. The thermodynamic closure was obtained by Peng-Robinson with VLE from TPn flash. The transport properties were computed using Chung model with diffusivity from the Schmidt number. They studied 4 test cases with three relevant for this study namely,

Test case	Ambient pressure (bar)	Ambient temperature (K)	Initial temperature (K)	$D_d(\mu m)$	velocity (m/s)	Y_{C12}
Case 1	62	700	363	38	0	0.999999
Case 2	88	1000	363	60	0.2	0.999999
Case 3	102	1200	363	60	0.2	0.999999

Table 8.1: Test case parameters for the study by Ping et al. [2019]

The above work emphasized on the evidence of surface tension with the Case 1 exhibiting spherical shape till the droplet's lifetime. The Case 2 and Case 3 exhibited olive shape in-contrast to the distinct shearing as reported by Crua et al. [2017].

8.2. Governing equation

The following system of equations is utilized in conjunction with the above-described class of equations in chapter 4.
Continuity equation,

$$\frac{\partial \rho}{\partial t} + \nabla \cdot (\rho \mathbf{u}) = 0 \tag{8.1}$$

Momentum equation,

$$\rho \frac{\partial \mathbf{u}}{\partial t} + \rho(\mathbf{u} \cdot \nabla)\mathbf{u} = \nabla \cdot [-p\mathbf{I} + \boldsymbol{\tau}] + \mathbf{F} \tag{8.2}$$

Energy equation,

$$\rho C_p \Big(\frac{\partial T}{\partial t} + (\mathbf{u} \cdot \nabla) T \Big) = -(\nabla \cdot \mathbf{q}) + Q \tag{8.3}$$

Species transport equation,

$$\frac{\partial (\rho \omega_i)}{\partial t} + \nabla \cdot (\rho \omega_i \mathbf{u}) = -\nabla \mathbf{j}_i + R_i \tag{8.4}$$

For the 3-D models, diffusion is modeled by MS law rather than the Fick's law. The mass flux and driving flux given by $\mathbf{j}_i = -\Big(-\rho \omega_i \sum_{k=1}^{Q} D_{ik} \mathbf{d}_k - \frac{D_i^T}{T} \nabla T \Big)$ with $\mathbf{d}_k = \nabla x_k + \frac{1}{P}[(x_k - \omega_k)\nabla p]$.
The above equations are modified at the interface to account for the phase change in the interface,

$$\nabla \cdot \mathbf{u} = \dot{m}''' \Big(\frac{1}{\rho_V} - \frac{1}{\rho_L} \Big) \tag{8.5}$$

$$\rho C_p \Big(\frac{\partial T}{\partial t} + (\mathbf{u} \cdot \nabla) T \Big) = -(\nabla \cdot \mathbf{q}) + \dot{m}''' h_{evap} \tag{8.6}$$

The phase field equation is given by,

$$\frac{\partial \phi}{\partial t} + \mathbf{u} \cdot \nabla \phi = \nabla \cdot \frac{\gamma \lambda}{\epsilon^2} \nabla \psi - \frac{\dot{m}'''}{\rho_l} \tag{8.7}$$

The mass flux is given by,

$$\dot{m}'' = \rho_g (u_1 - u_s) \times (y_f) + J_{1,i} \tag{8.8}$$

$$\dot{m}''(1 - (y_f)) = J_{1,i} \tag{8.9}$$

$$\dot{m}''' = \frac{J_{1,i}}{\epsilon(1 - y_f)} \tag{8.10}$$

where $J_{1,i}$ and ϵ are the mass flux ($\frac{Kg}{m^2 s}$) and interface thickness (m)

Property	Model	Mixing rule
Liquid thermal conductivity	variable Prandtl number	Harstad and Bellan [2004a]
Vapour thermal conductivity	Ideal thermal conductivity in COMSOL [2019]	Yorizane
Liquid and vapour viscosities	Chung high-pressure in Poling et al. [2001]	NA
Diffusion coefficient	Firoozabadi model in Leahy-Dios and Firoozabadi [2007]	Vignes equation
Surface tension	Lee and Chien model in Pedersen et al. [2006]	NA
Thermodynamic closure	PR-EoS	van der Waals one-fluid mixing rules

Table 8.2: Transport properties

As discussed previously in the fourth chapter, surface tension is an essential property of phase-field models. In this work, a relatively simple model based on the work of Lee and Chien from Pedersen et al. [2006] is used for the computation of the surface tension. Figure 8.1 shows the surface tension computed by PR and SRK EoS at various pressures. The plots were produced with the mass fraction of the vapor computed from the equality of fugacity with liquid mass fraction set at 1.

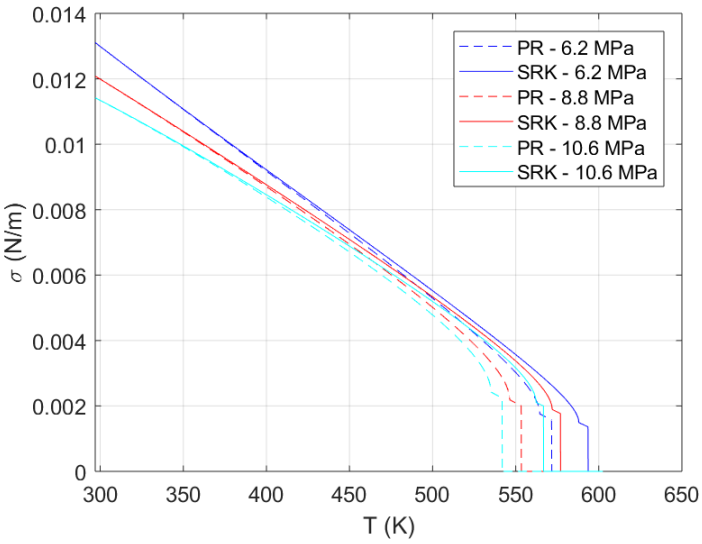

Figure 8.1: Surface tension coefficient of n-dodecane and nitrogen at different conditions

8.3. Geometry

The n-dodecane droplet of diameter $50\mu m$ is placed in the centre of a cube of edge-length $750\mu m$. A thin sphere of diameter $70\mu m$ and thickness $10\mu m$ is placed outside the droplet as to achieve the equality of fugacity at lower ambient temperatures. Without the layered sphere, it would be impossible to achieve the equality of fugacity as the ambient space's mass fraction of n-dodecane is set to 0.2.

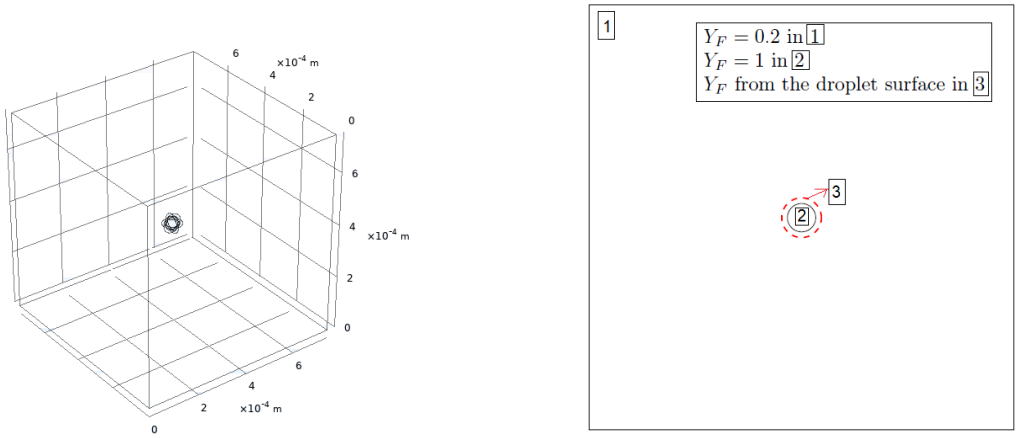

Figure 8.2: From left to right: Isometric view of the system and 2-D slice of the droplet, the dashed red line corresponds to the hollow sphere and the black circle to the droplet. Figure drawn to scale, magnification = 1000x

8.4. Mesh

In regard to the meshing, grid convergence study wasn't performed due to lack of time. Two different mesh models are used for level set and phase-field respectively. The computational domain along with the surface mesh is shown below(fig. 8.3).

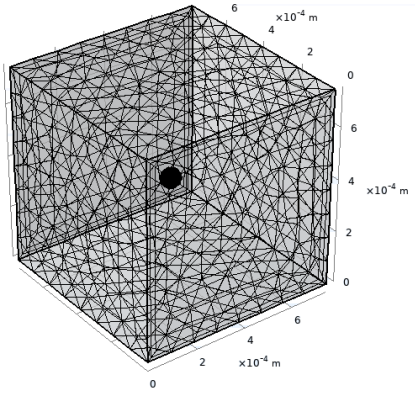

Figure 8.3: Computational domain

8.4.1. Level Set Method

Level set methods doesn't require high mesh resolution since it doesn't capture the liquid-vapour interface but translates it via the level set function. The domain is divided into two regions. The total number of elements is 71142 with average element quality 0.6879 and minimum element quality of 0.207.

	Minimum size (m)	Maximum size (m)	Max element growth rate
Region 1	5e-5	1e-4	1.21
Region 2	1e-8	3e-5	1.2

Table 8.3: Mesh parameters for LSM

8.4.2. Phase-field Method

Phase-field methods requires prohibitively high resolution to capture the liquid-vapour interface (O(-9) m). Ideally, time-adaptive mesh refinement should be utilized with the error function defined by the gradient of the phase-field help variable which dictates the further mesh refinement but to the computational con-

straints a fixed adaptive grid is used. The total number of elements corresponds to 81244. The global average element quality of 0.6857 and the global minimum element quality of 0.1941 is achieved.

	Minimum size (m)	Maximum size (m)	Max element growth rate
Region 1	7e-6	1e-4	1.25
Region 2	1e-8	5e-6	1.15

Table 8.4: Mesh parameters for PFM

8.5. FEM

COMSOL Multiphysics utilises Finite Element Methods to solve the model.

Direct PARDISO solver with constant Newton-Raphson algorithm with tolerance as the termination criteria is employed to solve the algebraic equations. Anderson acceleration is also used as to improve the convergence of the system. As for the temporal discretization, Backward Differentiation Formula (BDF) of order 1 is utilized. The time step in the BDF gets accepted only if,

$$|e_k| \leqslant A + R|U^k| \tag{8.11}$$

with A, R, e and U being the absolute tolerance, relative tolerance, local truncation error and the scaled/unscaled field component in time step k. The error per time step depends on two quantities:

- The size of the time step
- The order of the discretization scheme

Please refer the appendix A.9, for more detailed description of time-stepping in COMSOL. Regarding the spatial discretization, the number of the node denotes how each edge in the element is split e.g., P1 uses linear elements therefore one node at each end whereas P2 denotes three nodes, two at the ends and one node in the middle. P1 +P1 (velocity + pressure) scheme is employed in this study. The scaling of the variables has significant impact on the convergence of the system. Here, scaling is based on the initial values. For linear Lagrangian elements (q=1), absolute tolerances is set to 1e-8. Regarding the time step taken by the solver, manual option is used. The maximum time step of $3\mu s$ is used.

8.6. Numerical configuration

8.6.1. Boundary conditions

The boundary conditions for the model are given in table 8.5,

Test case	Ambient pressure (MPa)	Ambient temperature (K)	velocity (m/s)
Case 1	6.2	700	0.2
Case 2	8.8	1000	0.2
Case 3	10.6	1200	0.2

Table 8.5: Boundary conditions for n-dodecane of diameter of 50 μm

8.6.2. Level Set Method

The Level set equation with volume fraction instead of signed distance function is given by,

$$\frac{\partial \phi}{\partial t} + \mathbf{u} \cdot \nabla \phi = \gamma \nabla \cdot \left(\epsilon \nabla \phi - \phi(1-\phi) \frac{\nabla \phi}{|\nabla \phi|} \right) \tag{8.12}$$

where ϕ, γ and ϵ in 8.12 are the volume fraction of the nitrogen, re-initialization parameter which determines the average flow to which the interface is subjected and the parameter controlling the thickness respectively. The values of these quantities are given in the table 8.6. The R.H.S of the equation 8.12 compresses the interface as to maintain the sharp interface.

Quantity	Value	Remarks
Re-initialization parameter (γ)	0.2 m/s	Maximum velocity
Parameter controlling interface thickness	1.5e-4 m	Based on the default relation given below (COMSOL [2019])
Surface tension	Neglected	

Table 8.6: Parameters used in the LSM

8.6.3. Phase-field Method

The phase-field method with volume fraction as the order parameter is given by,

$$\frac{\partial \phi}{\partial t} + \mathbf{u} \cdot \nabla \phi = \nabla \cdot \frac{\gamma \lambda}{\epsilon^2} \nabla \psi \tag{8.13}$$

where parameters for the equation 8.13 are given in the table 8.7. The original Cahn-Hilliard is given in this form to reduce the labour of computing the fourth order derivatives. The mobility tuning parameter (χ) determines the time scale of the diffusion of the system under study. The phase-field settings used in this study is shown in the fig.8.4

Quantity	Value	Remarks
Mobility tuning parameter (ψ)	$\frac{2u_{max}}{(3\sqrt{2}\sigma)} \frac{h_{max}}{\epsilon}$	with u_{max} set at 0.2 m/s
Parameter controlling interface thickness	1.5e-4 m	Based on the default relation given below (COMSOL [2019])
$\frac{\partial f}{\partial \phi}$	0	External free energy is zero
Surface tension	Approximate value	Based on the Lee and Chien model

Table 8.7: Parameters used in the PFM

The parameter controlling interface thickness is an important input parameter as it determines the mobility of the fluids as in the case of the phase-field methods and initial interface distance in level set methods. It is given by the expression $h_{max}\Big((h_{max} > 1.3h_{min}) + 2(h_{max} <= 1.3h_{min})\Big)$ where h_{min} and h_{max} corresponds to the minimum and maximum grid size.

8.6.4. Weak contributions

It is important to note that the modules in COMSOL aren't suited for the phase change. Hence, for the droplet evaporation, the mass source phase-field equation are achieved using the weak contribution in COMSOL. Since, the mass source in continuity and energy equation can be neglected because of the local thermodynamic equilibrium as the density is the same at the interface stemming from equality of fugacity. Here, the weak contribution is implemented via the test function of psi (ψ). The negative sign convention is used since source term is brought from the R.H.S to the L.H.S. The weak contribution is given by $-\left(\frac{J_{1,i}}{\epsilon \rho_{sf}}\right) \times$ test(psi), where $J_i, z_1, \epsilon,$ and ρ_{sf} corresponds to the molecular diffusive flux of species i, mass fraction of the fuel at the surface, interface thickness and density at the interface. The weak contribution is illustrated in the fig.8.5.

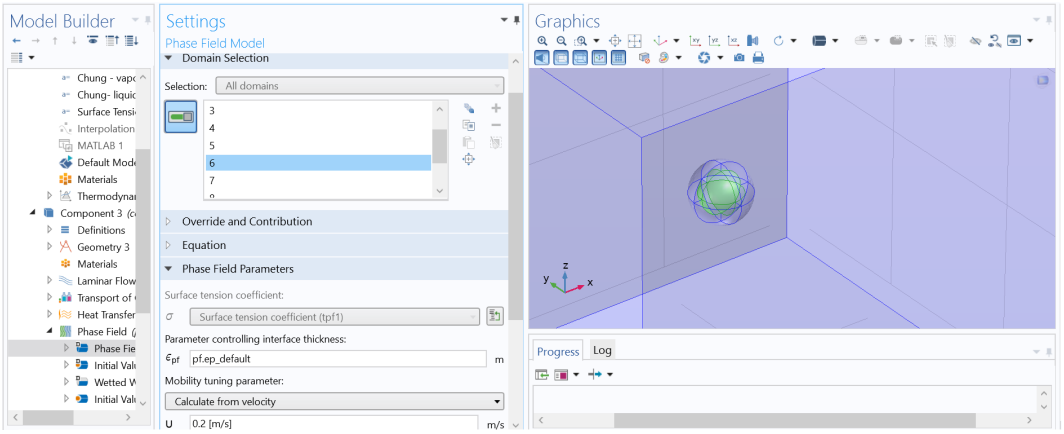

Figure 8.4: Phase-field module in COMSOL Multiphysics

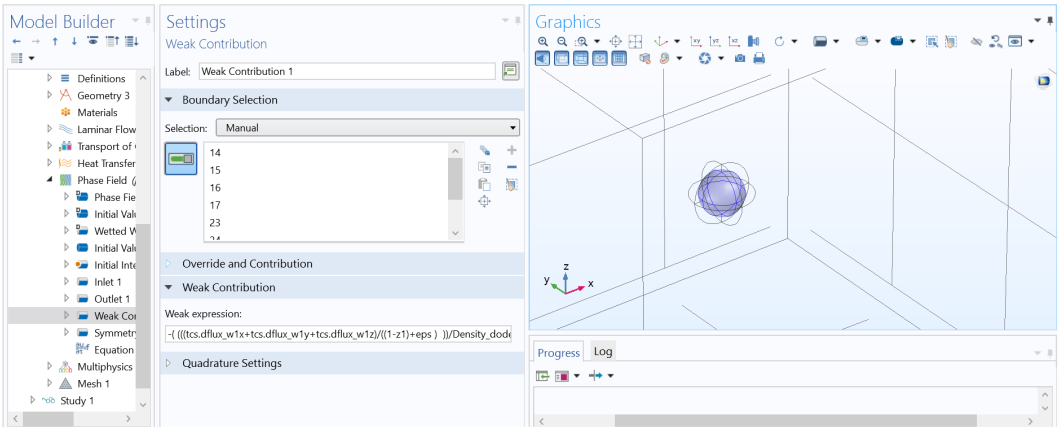

Figure 8.5: Weak contribution used in the phase-field module

The highlighted part in fig.8.4 corresponds to the droplet. The subplot in the right hand side shows the weak contribution setting used in this study. The modules are shown in the appendix A.10.

8.7. Results

8.7.1. Classical evaporation

In classical evaporation regime, the experimental observations note a spherical droplet reinforcing the notion of surface tension. From the shadowgraphs, it is evident that the level set and phase-field methods reproduces olive shaped droplets. The work of Ping et al. [2019] also reports olive shaped droplets for all the convective cases. The rate of vaporization is nearly same for both the methods. Similarly, from the shadowgraphs it is evident that the thickness of the interface in phase-field method is higher than the level set method. The figure 8.9 shows the shadowgraphs for the case 1 of Crua et al. [2017]. The density distribution of droplets of the phase-field method are also plotted for the case 1 against the numerical work by Ping et al. [2019] in figure 8.6. The latter and the experimental case shows a spherical droplet but it is to be noted that the case 1 in Ping et al. [2019] is a stationary one and the authors report olive shaped droplets for the convective cases. It is noticeable that the numerical results of Ping et al. [2019] produces nearly perfect circular profile for the density whereas this work has a droplet shadow. It can be hypothesized that this due to the diffusive flux and the convective flux of the n-dodecane, as seen in the plots of mass fraction in this work in the appendix A.11 against the mass fraction plot in the figure 2a in Ping et al. [2019].

Figure 8.6: Density distribution from the work of Ping et al. [2019] and this work (left to right) for Case 1 at t =0.1 ms

8.7.2. Translational mixing

As for the translational mixing, olive shaped droplets were noted for both the methods in this work. This regime also exhibits surface tension of significant magnitude. As time passes, the droplet may exhibit rapid deformations as two opposing forces namely inertial and capillary forces act on the droplet. This work reports olive shaped droplets for both the level set and phase-field methods. The figure 8.10 shows the shadowgraphs for the case 2 of Crua et al. [2017] against the shadowgraphs of level set and phase-field method respectively. The phase-field methods has a lower droplet lifetime compared to the level set method. The density distribution of droplets of the phase-field method are also plotted for the case 2 against the numerical work by Ping et al. [2019] in figure 8.7. The latter shows a circular droplet while the droplet in this case is close to an olive shape.

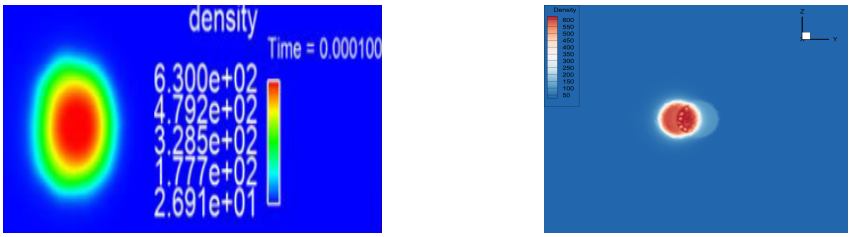

Figure 8.7: Density distribution from the work of Ping et al. [2019] and this work (left to right) for case 2 at t =0.1 ms

8.7.3. Diffusive mixing

In the diffusive mixing, the performance of level set method is slightly better than the phase-field method based on the shape of the droplet. The shadowgraphs from experiments, level set and phase-field in figures The phase-field exhibits nearly non-existent surface tension for this case. As seen in the previous case, both the cases exhibit olive shaped droplets. The figure 8.11 shows the shadowgraphs for the case 3 of Crua et al. [2017]. The density distribution of droplets of the phase-field method are also plotted for the case 3 against the numerical work by Ping et al. [2019] in figure 8.8. The square shaped droplet in the latter's work may signal the reduced significance of surface tension but its interesting to note that the surface tension was not considered in their model.

Figure 8.8: Density distribution from the work of Ping et al. [2019] and this work (left to right) for case 3 at t =0.1 ms

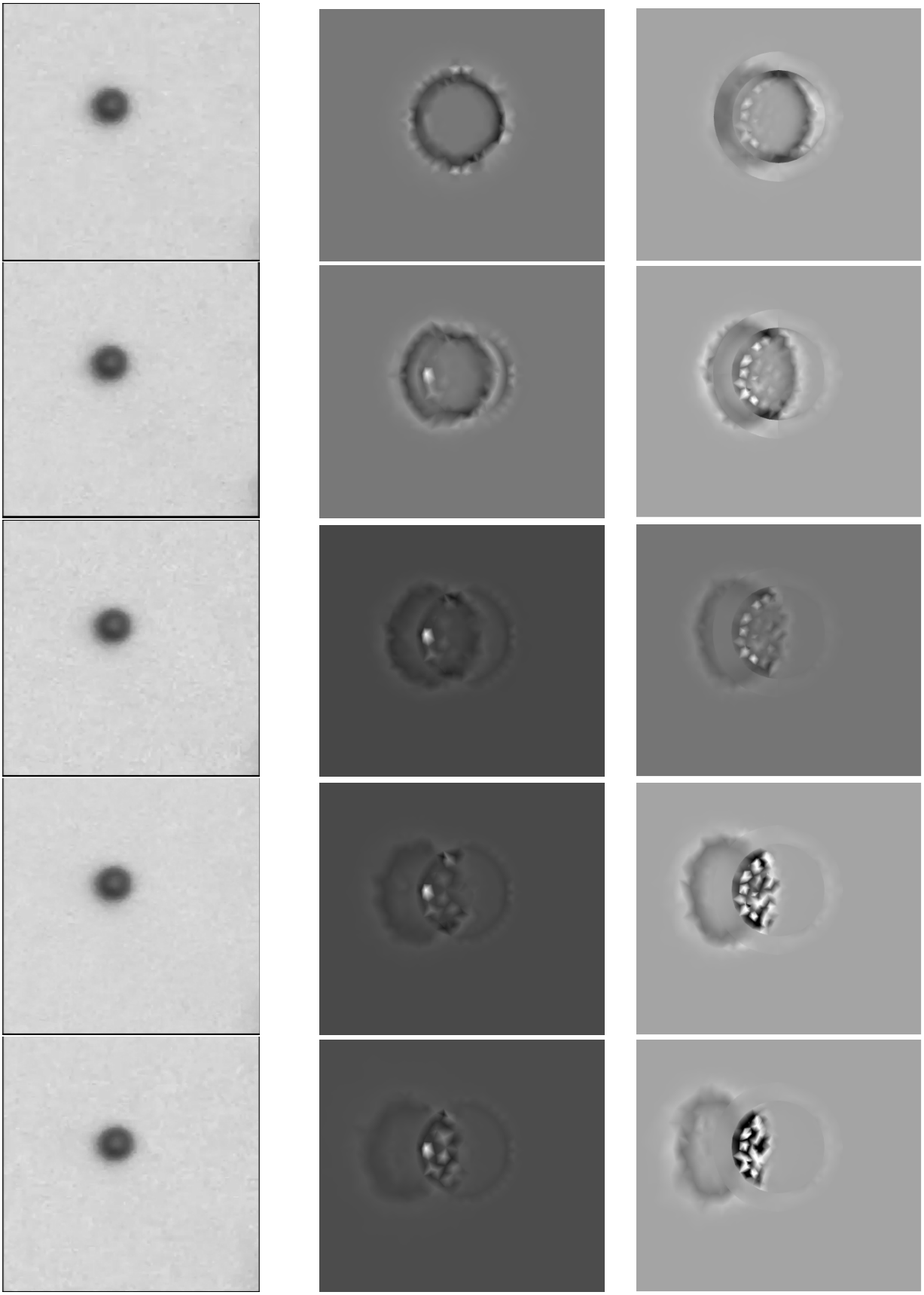

Figure 8.9: Instantaneous results from experiments (left), level-set method (center), phase-field method (right) at times 0.03333 ms, 0.067 ms, 0.1 ms, 0.133 ms and 0.167 ms of case-1

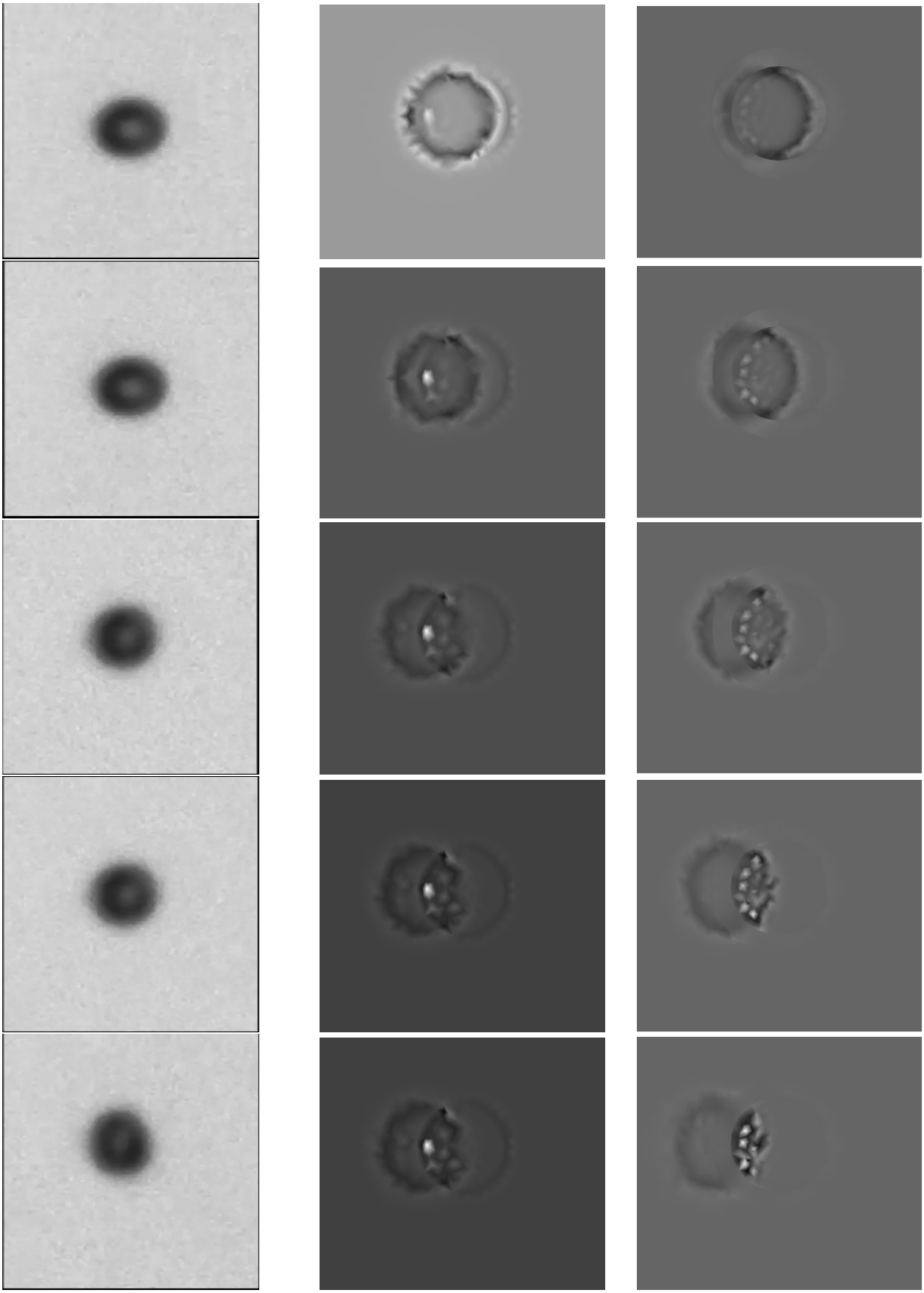

Figure 8.10: Instantaneous results from experiments (left), level-set method (center), phase-field method (right) at time at 0.03333 ms, 0.067 ms, 0.1 ms, 0.133 ms and 0.167 ms of case-2

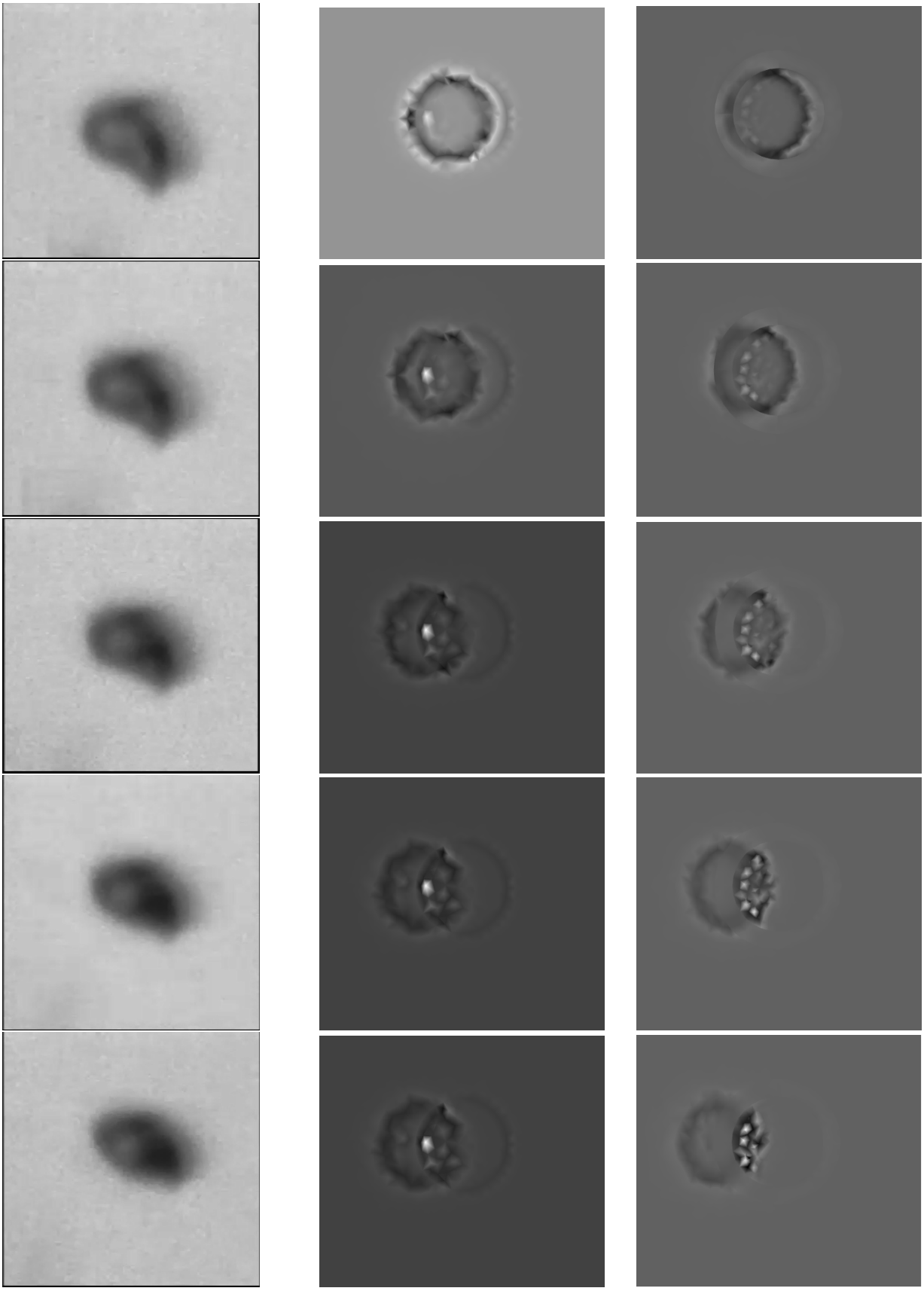

Figure 8.11: Instantaneous results from experiments (left), level-set method (center), phase-field method (right) at time at 0.03333 ms, 0.067 ms, 0.1 ms, 0.133 ms and 0.167 ms of case-3

8.8. Various quantities in the phase-field method

The Peclet, Capillary and Cahn number are plotted for the phase-field methods. The Peclet number represents the ratio of advection to diffusion, the Capillary number represents the impact of surface tension over the viscous force and finally, the Cahn number which represents the ratio of interfacial thickness over the characteristic length. The Cahn number totally depends on the interfacial thickness and hence constant value of 3 is obtained whereas Cahn number of 0.01 is recommended for the phase-field methods. The molecular diffusive fluxes and heat fluxes in the y component are plotted as to illustrate the differences the level set and phase-field method stemming from the non-local interactions in the latter. As for the Peclet number, a maximum of 2000 was achieved in the vicinity of the droplet. The plots of the mass fraction are given in the figure A.16, from which it is evident that the phase-field model predicts higher diffusion of the fuel into the ambient region. From the fig. 8.13, it is clear that the molecular diffusive fluxes are quite identical as observed in A.19. As for the energy fluxes, the trend remains the same but the magnitude differs it can be attributed to the changes in the mesh settings as with the same mesh settings in 2-D both LSM and PFM gave nearly identical results.

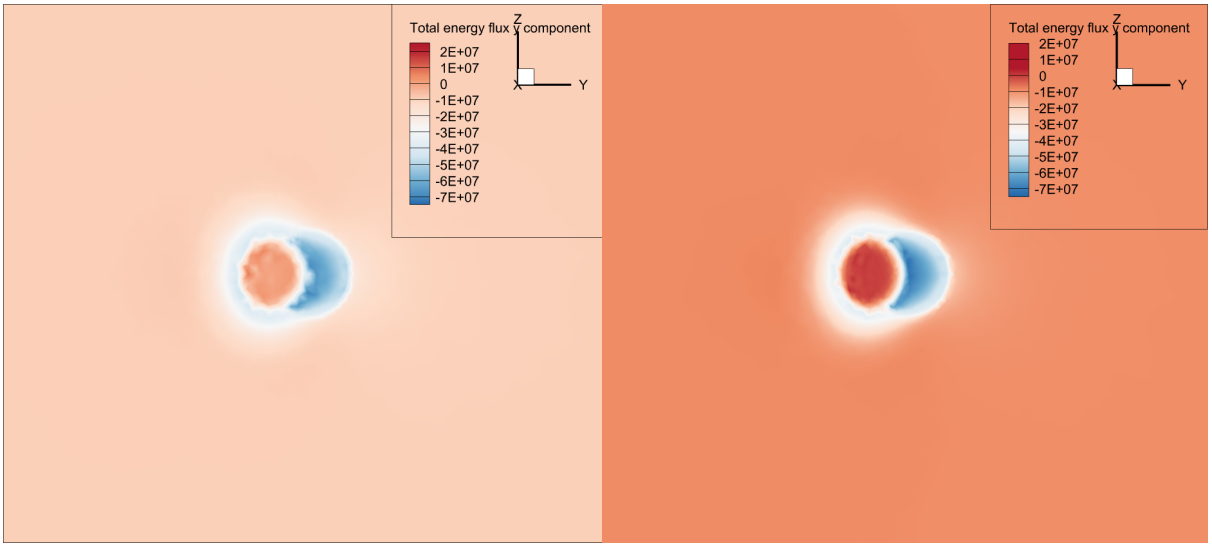

Figure 8.12: Total energy fluxes in y-component from level Set Method (left), phase-field method (right) of case-3 at t = 0.1 ms

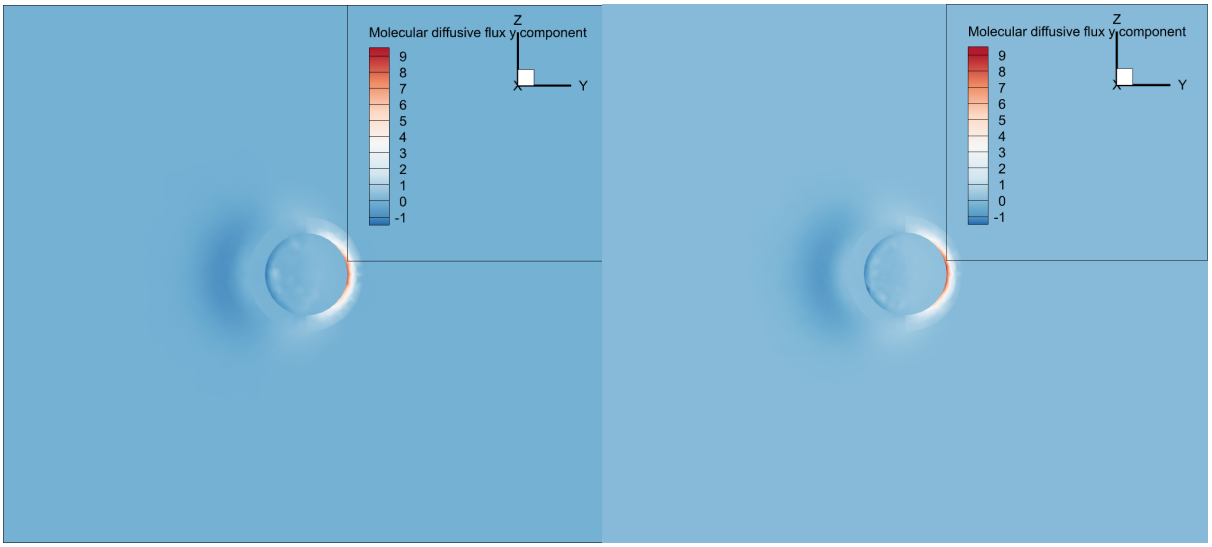

Figure 8.13: Molecular diffusive fluxes in y-component from level Set Method (left), phase-field method (right) of case-3 at t = 0.1 ms

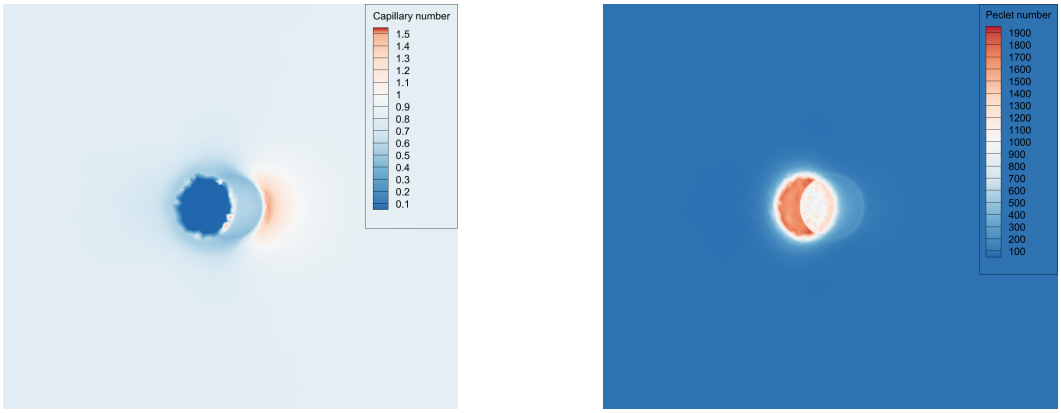

Figure 8.14: Peclet and Capillary numbers for Case-3 at t = 0.1 ms using phase-field method

8.9. 3D vs 1D

To illustrate the effects of the 3D model, a 1-D model based on the work of Gao et al. [2018] was executed in this work as well. Unlike the previous models with biot number assumption, this model is solved for the liquid phase and the gas quantities are computed by the 1/3 rd rule. Nusslet and Sherwood numbers based on Kulmala & Vesala correlation (as in Chapter-7, based on Ma [2016]) and Gao et al. [2018] are used.

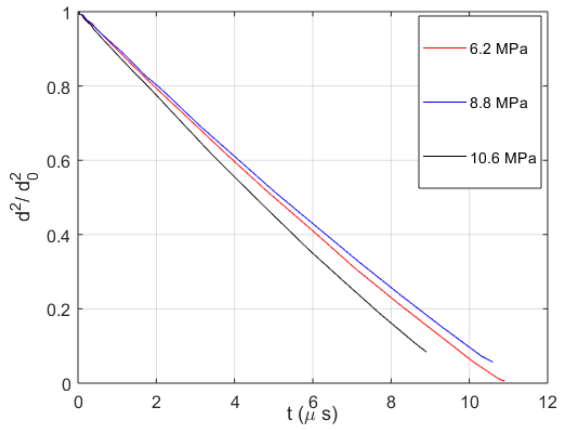

Figure 8.15: Evaporation behaviour of n-dodecane droplet obtained in this work at conditions studied by Crua et al. [2017]

The two correlations lead to very similar results and hence the former was preferred in this work due to lack of works supporting the former correlation. The 1-D model has significant discrepancies compared to the 3-D and experimental works.

8.10. Conclusions

The phase-field method predicts higher vaporization rate than the level set method. The level set method is concluded to be better than the phase-field model as the validity of the phase-field model is debatable with thickness of the interface set at 1.5e-4 m but still a level set model with better mesh resolution is desirable. The obtained results don't exhibit the characteristic deformation observed in the experimental campaign. Further investigations needs to be carried as the experimental work of Crua et al. [2017] observes spherical droplet for case-1 but the computational work of Ping et al. [2019] notes an olive shaped droplet. Since the 3-D models were meant to be demonstrator hence further refinements are necessary. The next step towards validating the model would be comparing the 3-D models against the numerical works such as Ping et al. [2019]. The increased thickness in the phase-field method increases the mobility of the flow field. These observations are supplemented by the differences in the flow field for a 2-D generic configuration under ambient conditions of case-1 (shown in appendix A.12). As the physical interface thickness increases, the phase-field variable is more physically representative of the model. At-last, LSM and PFM were compared for

the same mesh specifications in a 2D configuration. The flow-field is almost similar except to the interface of the latter, which can be described as slightly elongated spheroid compared to the former.

8.11. Recommendations

It would be captivating to study the effects of SAFT based EoS, and second-order effects such as Soret and Dufour.

9

Conclusions and recommendations

9.1. Conclusions

Liquid fuel atomization and air-fuel mixing has to be carefully examined as the standards postulated by ICAO-CAEP demands reduction in pollutant emissions. At subcritical pressures, atomization is dictated by aerodynamic shearing and homogeneous dispersion of the liquid droplets on the contrary in LRE the gaseous fuel is at supercritical state while the liquid oxidiser reaches the supercritical state. Hence, the mixing is governed by diffusive mixing rather than the surface tension. Also, as the fuel mixture reaches critical state, the thickness of the liquid-vapour interface increases. Recently, there's been a renewed interest in modeling the vaporization processes as to develop a robust SGS interface-modeling methods that's suitable for all regimes. Various research groups has developed a range of numerical frameworks for spray atomization ranging from Eulerian Lagrangian to Eulerian Eulerian model with VOF/ numerically diffused interface models with the recent numerical model being the work by Ma et al. [2019]. Although the physically consistent diffuse interface method have been utilized, the application of NSK for a binary mixture is contentious to say the least since NSK is recommended only for a single species e.g., fuel droplet evaporating in its own vapor. Therefore, the objective of the current thesis was to close the gap in the numerical modeling of droplet evaporation using physically consistent diffuse interface models via phase-field methods, given as:

Modeling of the interfacial dynamics using phase-field methods

The secondary objective of this work is utilization of robust thermo-physical property models. As for the validation of the models, different a range of experimental and computational works are considered. The 0-D and 1-D results are validated by comparing the droplet's lifetime. The 3-D model is validated by comparing the mass fraction plot with the experimental work of Crua et al. [2017].

9.1.1. 0-D results

The 0-D model was developed from the work of Kadota and Hiroyasu [1976]. The Kadota's results could not be replicated as the exact thermo-physical property models are not described. Hence, the recent work of Sánchez [2012] is used to validate the 0-D model. The results were in good agreement with the experimental results. The numerical model exhibited the characteristic increase in the droplet diameter in the initial phase of the heating.

9.1.2. 1-D results

As for the 1-D model, three methods were utilized namely,

1. Using correlations such as Gr and Pr

2. Assuming the 0-D model for the liquid droplet and solving the gaseous system in a 1-D framework

3. Simulating the liquid part and assuming correlations for the gaseous regions.

As for the validation two works namely Subashki [2016] and Ebrahimian and Habchi [2011] were used. Although the numerical framework without any correlation is interesting, the absence of gravity in the system is a serious limitation to the latter's work as most of the experiments were conducted in micro-gravity as to ensure the spherical structure of the droplet. The performance of the EoS are in the order SRK, PR and RK in the descending order respectively.

9.1.3. 3-D results

As for the 3-D models, level set and phase-field methods were utilized to model the interface dynamics. The experimental work of Crua et al. [2017] and numerical work of Ping et al. [2019] are used to validate the system. The phase-field model did capture some features of the droplet vaporization from subcritical to supercritical regimes namely presence of surface tension leading to the olive shaped droplets. But there are a lot of room for improvements, as the numerical thickness of the interface should be in the order of the physical interface thickness. The phase-field and level set methods were plotted for a generic 2-D model to illustrate the differences between these methods.

9.2. Recommendations

The following improvements will be fascinating to be included in the numerical framework,

- Implementation of better surface tension models.
- Modelling of Soret and Dufour effects.
- Utilization of PC-SAFT for the thermodynamic closure of the system: The coupling between COMSOL Multiphysics and the MATLAB significantly increases the computing time. Therefore, the PC-SAFT wasn't used for the 3-D models.
- Application of better thermal conductivity models: Although entropy scaling is quite captivating better mixing rules should be examined either via solving the thermal conductivity using one-fluid mixing rule or finding a mixing rule using Artificial Neural Networks from extensive the experimental data sets.
- As evidenced from the mesh resolution for the phase-field methods either a proper scaling protocol needs to be determined or a subgrid scale needs to be developed accounting for the interfacial dynamics.
- Finally, study of droplet dynamics under very fine mesh (O(-9)m) is required for a proper study of phase-field models.

Bibliography

Agelia M. Abudour, Sayeed A. Mohammad, Robert L. Robinson, and Khaled A.M. Gasem. Volume-translated peng–robinson equation of state for saturated and single-phase liquid densities. *Fluid Phase Equilibria*, 335:74 – 87, 2012. ISSN 0378-3812. doi: https://doi.org/10.1016/j.fluid.2012.08.013. URL http://www.sciencedirect.com/science/article/pii/S0378381212003901.

Michael Adewumi. Png 520: Phase relations in reservoir engineering. *Penn State, College of Earth and Mineral Sciences*, Accessed on 3/31/2020. URL https://www.e-education.psu.edu/png520/.

MJ Assael, I Bogdanou, SK Mylona, ML Huber, RA Perkins, and V Vesovic. Reference correlation of the thermal conductivity of n-heptane from the triple point to 600 k and up to 250 mpa. *Journal of Physical and Chemical Reference Data*, 42, 2013. doi: 10.1063/1.4794091. URL http://dx.doi.org/10.1063/1.4794091.

M.R. Baer and J.W. Nunziato. A two-phase mixture theory for the deflagration-to-detonation transition (ddt) in reactive granular materials. *International Journal of Multiphase Flow*, 12(6):861–889, 1986. ISSN 0301-9322. doi: https://doi.org/10.1016/0301-9322(86)90033-9. URL https://www.sciencedirect.com/science/article/pii/0301932286900339.

B. Balaji, Vasudevan Raghavan, K. Ramamurthi, and George Gogos. A numerical study of evaporation characteristics of spherical n-dodecane droplets in high pressure nitrogen environment. *Physics of Fluids*, 23 (6):063601, 2011. doi: 10.1063/1.3599700. URL https://doi.org/10.1063/1.3599700.

Daniel Banuti, Muralikrishna Raju, Peter C. Ma, Matthias Ihme, and Jean-Pierre Hickey. Seven questions about supercritical fluids - towards a new fluid state diagram. *55th AIAA Aerospace Sciences Meeting*, 2017. doi: 10.2514/6.2017-1106. URL https://arc.aiaa.org/doi/abs/10.2514/6.2017-1106.

J. A. Barker and D. Henderson. Perturbation theory and equation of state for fluids. ii. a successful theory of liquids. *The Journal of Chemical Physics*, 47(11):4714–4721, 1967. doi: 10.1063/1.1701689. URL https://doi.org/10.1063/1.1701689.

Ian H. Bell, Richard Messerly, Monika Thol, Lorenzo Costigliola, and Jeppe C. Dyre. Modified entropy scaling of the transport properties of the lennard-jones fluid. *The Journal of Physical Chemistry B*, 123(29):6345–6363, 2019. doi: 10.1021/acs.jpcb.9b05808. URL https://doi.org/10.1021/acs.jpcb.9b05808. PMID: 31241958.

G. Billet, V. Giovangigli, and G. de Gassowski. Impact of volume viscosity on a shock–hydrogen-bubble interaction. *Combustion Theory and Modelling*, 12(2):221–248, 2008. doi: 10.1080/13647830701545875. URL https://doi.org/10.1080/13647830701545875.

R. B. Bird, W. E. Stewart, and E. N. Lightfoot. Transport phenomena. *AIChE Journal*, 7(2):5J–6J, 1961. doi: 10.1002/aic.690070245. URL https://aiche.onlinelibrary.wiley.com/doi/abs/10.1002/aic.690070245.

R. Byron Bird and Daniel J. Klingenberg. Multicomponent diffusion—a brief review. *Advances in Water Resources*, 62:238 – 242, 2013. ISSN 0309-1708. doi: https://doi.org/10.1016/j.advwatres.2013.05.010. URL http://www.sciencedirect.com/science/article/pii/S0309170813000900.

B. Bork, A. Preusche, F. Weckenmann, G. Lamanna, and A. Dreizler. Measurement of species concentration and estimation of temperature in the wake of evaporating n-heptane droplets at trans-critical conditions. *Proceedings of the Combustion Institute*, 36(2):2433 – 2440, 2017. ISSN 1540-7489. doi: https://doi.org/10.1016/j.proci.2016.07.037. URL http://www.sciencedirect.com/science/article/pii/S1540748916302954.

Radouan Boukharfane, Pedro José Martínez Ferrer, Arnaud Mura, and Vincent Giovangigli. On the role of bulk viscosity in compressible reactive shear layer developments. *European Journal of Mechanics - B/Fluids*, 77:32 – 47, 2019. ISSN 0997-7546. doi: https://doi.org/10.1016/j.euromechflu.2019.02.005. URL http://www.sciencedirect.com/science/article/pii/S099775461830565X.

Shane P. Cadogan, Bhavik Mistry, Yat Wong, Geoffrey C. Maitland, and J. P. Martin Trusler. Diffusion coefficients of carbon dioxide in eight hydrocarbon liquids at temperatures between (298.15 and 423.15) k at pressures up to 69 mpa. *Journal of Chemical & Engineering Data*, 61(11):3922–3932, 2016. doi: 10.1021/acs.jced.6b00691. URL https://doi.org/10.1021/acs.jced.6b00691.

Calsep. Pvtsim 20 method documentation. 2011.

Bernardo Carreón-Calderón and Verónica Uribe-Vargas. Thermomechanical point of view of the effect of pressure and free volume on the molecular diffusion coefficients. *Journal of Chemical & Engineering Data*, 64(5):1956–1969, 2019. doi: 10.1021/acs.jced.8b00995. URL https://doi.org/10.1021/acs.jced.8b00995.

Christian Chauveau, Fabien Halter, A Lalonde, and Iskender Gökalp. An experimental study on the droplet vaporization: effects of heat conduction through the support fiber. 01 2008. ILASS-EUROPE, COMO, IT, 2008.

Ting Horng Chung, Mohammad Ajlan, Lloyd L. Lee, and Kenneth E. Starling. Generalized multiparameter correlation for nonpolar and polar fluid transport properties. *Industrial & Engineering Chemistry Research*, 27(4):671–679, 1988. doi: 10.1021/ie00076a024. URL https://doi.org/10.1021/ie00076a024.

COMSOL. *Chemical Reaction Engineering Module User's Guide*. Version: COMSOL 5.5. 2019.

Andrew W. Cook. Enthalpy diffusion in multicomponent flows. *Physics of Fluids*, 21(5):055109, 2009. doi: 10.1063/1.3139305. URL https://doi.org/10.1063/1.3139305.

Cyril Crua, Julien Manin, and Lyle M. Pickett. On the transcritical mixing of fuels at diesel engine conditions. *Fuel*, 208:535 – 548, 2017. ISSN 0016-2361. doi: https://doi.org/10.1016/j.fuel.2017.06.091. URL http://www.sciencedirect.com/science/article/pii/S0016236117308013.

Lluis Jofre Cruanyes and Javier Urzay. On interfacial transport in transcritical flows of liquid fuels into high-pressure combustors. *Center for Turbulence Research Annual Research Briefs*, 2016. URL http://hdl.handle.net/2117/185922.

C Duwig, G Lupo, A Gruber, L Brandt, P B Govindaraju, M Ihme, and T Jaravel. Direct numerical simulation , analysis , and modeling of the evaporation of multiple fuel droplets in a hot turbulent flow. *Center for Turbulence Research*, 2018. URL https://stanford.app.box.com/s/5ir42z2bwi8jg4lgsb6k0kcwsuifyjn6.

Vahid Ebrahimian and Chaouki Habchi. Towards a predictive evaporation model for multi-component hydrocarbon droplets at all pressure conditions. *International journal of heat and mass transfer*, 54:3552–3565, 07 2011. doi: 10.1016/j.ijheatmasstransfer.2011.03.031.

Mostafa Mohamed Elmetwalli Elhawwari. Equation of state for hydrocarbons and water. *Dissertation*, 2020. POLITECNICO DI TORINO.

Pierre Gaillard, Vincent Giovangigli, and Lionel Matuszewski. A diffuse interface Lox / hydrogen transcritical flame model, HAL Id : hal-01308378 A diffuse interface Lox / hydrogen transcritical flame model. 2016. doi: 10.1080/13647830.2016.1150518. URL http://dx.doi.org/10.1080/13647830.2016.1150518.

Suya Gao, Junhao Yan, Mianzhi Wang, and Chia-Fon Lee. Modeling of quasi-1d multi-component fuel droplet vaporization using discrete approach with experimental validation. apr 2018. ISSN 0148-7191. doi: https://doi.org/10.4271/2018-01-0287. URL https://doi.org/10.4271/2018-01-0287.

Apostolos Georgiadis, Felix Llovell, Alexander Bismarck, Felipe J. Blas, Amparo Galindo, Geoffrey C. Maitland, J.P.Martin Trusler, and George Jackson. Interfacial tension measurements and modelling of (carbon dioxide+n-alkane) and (carbon dioxide+water) binary mixtures at elevated pressures and temperatures. *The Journal of Supercritical Fluids*, 55(2):743 – 754, 2010. ISSN 0896-8446. doi: https://

doi.org/10.1016/j.supflu.2010.09.028. URL http://www.sciencedirect.com/science/article/pii/S0896844610003189.

George Gogos, Siang Soh, and Daniel N. Pope. Effects of gravity and ambient pressure on liquid fuel droplet evaporation. *International Journal of Heat and Mass Transfer*, 46(2):283 – 296, 2003. ISSN 0017-9310. doi: https://doi.org/10.1016/S0017-9310(02)00269-7. URL http://www.sciencedirect.com/science/article/pii/S0017931002002697.

Z. Guo and P. Lin. A thermodynamically consistent phase-field model for two-phase flows with thermocapillary effects. *Journal of Fluid Mechanics*, 766:226–271, 2015. doi: 10.1017/jfm.2014.696.

K. G. Harstad and J. Bellan. Mixing rules for multicomponent mixture mass diffusion coefficients and thermal diffusion factors. *The Journal of Chemical Physics*, 120(12):5664–5673, 2004a. doi: 10.1063/1.1650296. URL https://doi.org/10.1063/1.1650296.

Kenneth Harstad and Josett Bellan. High-pressure binary mass diffusion coefficients for combustion applications. *Industrial & Engineering Chemistry Research*, 43(2):645–654, 2004b. doi: 10.1021/ie0304558. URL https://doi.org/10.1021/ie0304558.

Peng He, YunQing Li, and LiFeng Zhao. Evaporation of liquid fuel droplet at supercritical conditions. *Science China Technological Sciences*, 54(2):369–374, 2011. ISSN 1862-281X. doi: 10.1007/s11431-010-4231-x. URL https://doi.org/10.1007/s11431-010-4231-x.

Madlen Hopp and Joachim Gross. Thermal conductivity of real substances from excess entropy scaling using pcp-saft. *Industrial & Engineering Chemistry Research*, 56(15):4527–4538, 2017. doi: 10.1021/acs.iecr.6b04289. URL https://doi.org/10.1021/acs.iecr.6b04289.

Hongfa Huo, Xingjian Wang, and Vigor Yang. A general study of counterflow diffusion flames at subcritical and supercritical conditions: Oxygen/hydrogen mixtures. *Combustion and Flame*, 161(12):3040 – 3050, 2014. ISSN 0010-2180. doi: https://doi.org/10.1016/j.combustflame.2014.06.005. URL http://www.sciencedirect.com/science/article/pii/S0010218014001825.

Frederike Jaeger, Omar K. Matar, and Erich A. Müller. Bulk viscosity of molecular fluids. *The Journal of Chemical Physics*, 148(17):174504, 2018. doi: 10.1063/1.5022752. URL https://doi.org/10.1063/1.5022752.

Didier Jamet. Diffuse interface models in fluid mechanics. *Lecture notes, Grenoble - CEA*, 1999. URL http://citeseerx.ist.psu.edu/viewdoc/download?doi=10.1.1.320.3144&rep=rep1&type=pdf.

J. D. Jin and Gary Lee Borman. A model for multicomponent droplet vaporization at high ambient pressures. *SAE International*, 94, 1985. ISSN 0148-7191. doi: https://doi.org/10.4271/850264. URL https://doi.org/10.4271/850264.

Lluís Jofre and Javier Urzay. Transcritical diffuse-interface hydrodynamics of propellants in high-pressure combustors of chemical propulsion systems. *Progress in Energy and Combustion Science*, 82:100877, 2021. ISSN 0360-1285. doi: https://doi.org/10.1016/j.pecs.2020.100877. URL https://www.sciencedirect.com/science/article/pii/S0360128520300873.

Toshikazu Kadota and Hiroyuki Hiroyasu. Evaporation of a Single Droplet at Elevated Pressures and Temperatures . *Bulletin of JSME*, 19(138):1515–1521, 1976. doi: 10.1299/jsme1958.19.1515.

V V Khatavkar, P D Anderson, Meijer, and H E H. On scaling of diffuse–interface models. *Chemical Engineering Science*, 61(8):2364 – 2378, 2006. ISSN 0009-2509. doi: https://doi.org/10.1016/j.ces.2005.10.035. URL http://www.sciencedirect.com/science/article/pii/S0009250905008043.

Georgios M. Kontogeorgis and Georgios K. Folas. *Thermodynamic Models for Industrial Applications*. John Wiley Sons, Ltd, 2009. ISBN 9780470747537. doi: 10.1002/9780470747537.fmatter. URL https://onlinelibrary.wiley.com/doi/abs/10.1002/9780470747537.fmatter.

Rajamani Krishna. Diffusing uphill with james clerk maxwell and josef stefan. *Chemical Engineering Science*, 195:851 – 880, 2019. ISSN 0009-2509. doi: https://doi.org/10.1016/j.ces.2018.10.032. URL http://www.sciencedirect.com/science/article/pii/S0009250918307516.

Guilhem Lacaze and Joseph C. Oefelein. A non-premixed combustion model based on flame structure analysis at supercritical pressures. *Combustion and Flame*, 159(6):2087 – 2103, 2012. ISSN 0010-2180. doi: https://doi.org/10.1016/j.combustflame.2012.02.003. URL http://www.sciencedirect.com/science/article/pii/S0010218012000429.

Patrick Lafon, Hua Meng, Vigor Yang, and Mohammed Habiballah. Vaporization of liquid oxygen (LOX) droplets in hydrogen and water environments under sub- and super-critical conditions. (May 2007):1–26, 2008. doi: 10.1080/00102200701486873.

G. Lamanna, H. Sun, M. Schüler, B. Weigand, D. MAGATTI, and F. FERRI. Comparative study of equilibrium and nonequilibrium evaporation models for vaporizing droplet arrays at high-pressure. *Advanced Combustion and Aerothermal Technologies*, pages 445–455, 2007.

Grazia Lamanna, Christoph Steinhausen, Bernhard Weigand, Andreas Preusche, Benjamin Bork, Andreas Dreizler, Rolf Stierle, and Joachim Groß. On the importance of non-equilibrium models for describing the coupling of heat and mass transfer at high pressure. *International Communications in Heat and Mass Transfer*, 98:49 – 58, 2018. ISSN 0735-1933. doi: https://doi.org/10.1016/j.icheatmasstransfer.2018.07.012. URL http://www.sciencedirect.com/science/article/pii/S0735193318301830.

Alana Leahy-Dios and Abbas Firoozabadi. Unified model for nonideal multicomponent molecular diffusion coefficients. *AIChE Journal*, 53(11):2932–2939, 2007. doi: 10.1002/aic.11279. URL https://aiche.onlinelibrary.wiley.com/doi/abs/10.1002/aic.11279.

Likun Ma. Computational modeling of turbulent spray combustion, 2016. TU Delft, https://doi.org/10.4233/uuid:c1c27066-a205-45f4-a7b4-e36016bc313a.

Peter C. Ma, Yu Lv, Daniel T. Banuti, Jean-Pierre Hickey, and Mathias Ihme. Numerical methods for transcritical real-fluid reacting flows using the flamelet progress variable approach. *55th AIAA Aerospace Sciences Meeting*, 2017. doi: 10.2514/6.2017-0143. URL https://arc.aiaa.org/doi/abs/10.2514/6.2017-0143.

Peter C. Ma, Hao Wu, Daniel T. Banuti, and Matthias Ihme. On the numerical behavior of diffuse-interface methods for transcritical real-fluids simulations. *International Journal of Multiphase Flow*, 113:231 – 249, 2019. ISSN 0301-9322. doi: https://doi.org/10.1016/j.ijmultiphaseflow.2019.01.015. URL http://www.sciencedirect.com/science/article/pii/S0301932218300673.

D. B. Macleod. On a relation between surface tension and density. *Trans. Faraday Soc.*, 19:38–41, 1923. doi: 10.1039/TF9231900038. URL http://dx.doi.org/10.1039/TF9231900038.

J. Manin, M. Bardi, L.M. Pickett, R.N. Dahms, and J.C. Oefelein. Microscopic investigation of the atomization and mixing processes of diesel sprays injected into high pressure and temperature environments. *Fuel*, 134:531 – 543, 2014. ISSN 0016-2361. doi: https://doi.org/10.1016/j.fuel.2014.05.060. URL http://www.sciencedirect.com/science/article/pii/S0016236114005225.

Jan Matheis. Numerical simulation of fuel injection and turbulent mixing under high-pressure conditions. *Dissertation*, 2018. Technische Universität München, URL http://mediatum.ub.tum.de/doc/1363601/document.pdf.

Jan Matheis and Stefan Hickel. Multi-component vapor-liquid equilibrium model for les and application to ecn spray a. 2016.

Jan Matheis and Stefan Hickel. Multi-component vapor-liquid equilibrium model for les of high-pressure fuel injection and application to ecn spray a. *International Journal of Multiphase Flow*, 99:294–311, 2018. ISSN 0301-9322. doi: https://doi.org/10.1016/j.ijmultiphaseflow.2017.11.001. URL https://www.sciencedirect.com/science/article/pii/S0301932217301076.

Hua Meng and Vigor Yang. International Journal of Heat and Mass Transfer Vaporization of two liquid oxygen (LOX) droplets in tandem in convective hydrogen streams at supercritical pressures. *International Journal of Heat and Mass Transfer*, 68:500–508, 2014. ISSN 0017-9310. doi: 10.1016/j.ijheatmasstransfer.2013.09.041. URL http://dx.doi.org/10.1016/j.ijheatmasstransfer.2013.09.041.

R. S. Miller, K. Harstad, and J. Bellan. Evaluation of equilibrium and non-equilibrium evaporation models for many-droplet gas-liquid flow simulations. 24:1025–1055, 1998. doi: https://doi.org/10.1016/S0301-9322(98)00028-7. URL http://www.sciencedirect.com/science/article/pii/S0301932298000287.

Amin Mahmoudi Moghadam, Mehdi Shafieefar, and Roozbeh Panahi. Development of a high-order level set method: Compact conservative level set (ccls). *Computers Fluids*, 129:79 – 90, 2016. ISSN 0045-7930. doi: https://doi.org/10.1016/j.compfluid.2016.02.002.

Angel Mulero. *Theory and Simulation of Hard-Sphere Fluids and Related Systems*, volume 753. Springer, Berlin, Heidelberg, 2008. doi: 10.1007/978-3-540-78767-9.

Davy Nayigizente, Thomas Schmitt, and Sébastien Ducruix. Development of an interface thickening method for the direct numerical simulation of compressible liquid-vapor flows in the framework of the Second Gradient theory. 2018. URL https://hal.archives-ouvertes.fr/hal-01809166.

Hiroshi Nomura, Yasushige Ujiie, Hans J. Rath, Jun'ich Sato, and Michikata Kono. Experimental study on high-pressure droplet evaporation using microgravity conditions. *Symposium (International) on Combustion*, 26(1):1267 – 1273, 1996. ISSN 0082-0784. doi: https://doi.org/10.1016/S0082-0784(96)80344-4. URL http://www.sciencedirect.com/science/article/pii/S0082078496803444.

Joseph C Oefelein. Mixing and combustion of cryogenic oxygen-hydrogen shear-coaxial jet flames at supercritical pressure. *Combustion Science and Technology*, 178:229–252, 2006. ISSN 0021-9991. doi: https://doi.org/10.1080/00102200500325322.

Elin Olsson, Gunilla Kreiss, and Sara Zahedi. A conservative level set method for two phase flow ii. *Journal of Computational Physics*, 225(1):785 – 807, 2007. ISSN 0021-9991. doi: https://doi.org/10.1016/j.jcp.2006.12.027. URL http://www.sciencedirect.com/science/article/pii/S0021999107000046.

Sridhar Palle, Christopher Nolan, and Richard S. Miller. On molecular transport effects in real gas laminar diffusion flames at large pressure. *Physics of Fluids*, 17(10):103601, 2005. doi: 10.1063/1.1990198. URL https://aip.scitation.org/doi/abs/10.1063/1.1990198.

Saptarshi Basu; Avinash K Agarwal; Achintya Mukhopadhyay; Chetankumar Patel. Droplets and sprays : applications for combustion and propulsion. *Springer Singapore*, 2018. doi: 10.1007/978-981-10-7449-3.

Karen Schou Pedersen, Karen Schou Pedersen, Peter Lindskou Christensen, Jawad Azeem Shaikh, and Peter L. Christensen. *Phase behavior of petroleum reservoir fluids*. 2006. doi: https://doi.org/10.1201/9781420018257.

Yi Ping, Sajad Jafari, Songzhi Yang, and Chaouki Habchi. Numerical analysis of subcritical evaporation and transcritical mixing of droplet using a tabulated multicomponent vapor-liquid equilibrium model. 09 2019.

Bruce E. Poling, John M. Prausnitz, and John P. O'Connell. *The properties of gases and liquids*. McGraw-Hill, New York, 2001. ISBN 0070116822 9780070116825 0071189718 9780071189712. URL http://www.worldcat.org/search?qt=worldcat_org_all&q=0070116822.

Dahms Rainer, Julien Manin, Lyle M Pickett, and Joseph C Oefelein. Understanding high-pressure gas-liquid interface phenomena in Diesel engines. *Proceedings of the Combustion Institute*, 34(1):1667–1675, 2013. ISSN 1540-7489. doi: 10.1016/j.proci.2012.06.169. URL http://dx.doi.org/10.1016/j.proci.2012.06.169.

Guillaume Ribert, Xavier Petit, and Pascale Domingo. High-pressure methane-oxygen flames.analysis of subgrid scale contributions in filtered equations of state. *The Journal of Supercritical Fluids*, 121:78 – 88, 2017. ISSN 0896-8446. doi: https://doi.org/10.1016/j.supflu.2016.08.020. URL http://www.sciencedirect.com/science/article/pii/S0896844616302765.

Yaakov Rosenfeld. Relation between the transport coefficients and the internal entropy of simple systems. *Phys. Rev. A*, 15:2545–2549, Jun 1977. doi: 10.1103/PhysRevA.15.2545. URL https://link.aps.org/doi/10.1103/PhysRevA.15.2545.

Anthony M Ruiz, Guilhem Lacaze, Joseph C Oefelein, Raphael Mari, Bénédicte Cuenot, Laurent Selle, and Thierry Poinsot. Numerical benchmark for high- reynolds-number supercritical ows with large density gradients. *AIAA Journal*, 54:1445–1460, 2016. ISSN 0001-1452. doi: http://dx.doi.org/10.2514/1.J053931.

Patricia Sierra Sánchez. Modeling the dispersion and evaporation of sprays in aeronautical combustion chambers. *Dissertation*, 2012. University of Toulose, 2012, https://oatao.univ-toulouse.fr/6980/.

Richard Saurel and Carlos Pantano. Diffuse-interface capturing methods for compressible two-phase flows. *Annual Review of Fluid Mechanics*, 50(1):105–130, 2018. doi: 10.1146/annurev-fluid-122316-050109. URL https://doi.org/10.1146/annurev-fluid-122316-050109.

Sergei S. Sazhin. Advanced models of fuel droplet heating and evaporation. *Progress in Energy and Combustion Science*, 32(2):162 – 214, 2006. ISSN 0360-1285. doi: https://doi.org/10.1016/j.pecs.2005.11.001. URL http://www.sciencedirect.com/science/article/pii/S0360128505000535.

Daisuke Segawa, Tomoki Kajikawa, and Toshikazu Kadoka. Transcritical phenomena of autoignited fuel droplet at high pressures under microgravity. *Microgravity - Science and Technology*, 17(3):15–22, Sep 2005. ISSN 1875-0494. doi: 10.1007/BF02872083. URL https://doi.org/10.1007/BF02872083.

J.S. Shuen, Vigor Yang, and C.C. Hsiao. Combustion of liquid-fuel droplets in supercritical conditions. *Combustion and Flame*, 89(3):299 – 319, 1992. ISSN 0010-2180. doi: https://doi.org/10.1016/0010-2180(92)90017-J. URL http://www.sciencedirect.com/science/article/pii/001021809290017J.

Georgi Valeriev Subashki. An investigation of transcritical effects for fuel injection and mixing applications. *Master Dissertation*, 2016. MIT, 2016, URL http://hdl.handle.net/1721.1/107020.

S Sugden. The parachor and valency. 1930. doi: 10.1039/TF9231900038. URL http://dx.doi.org/10.1039/TF9231900038.

Shinji Takahashi. Preparation of a generalized chart for the diffusion coefficients of gases at high pressures. *Journal of Chemical Engineering of Japan*, 7(6):417–420, 1975. doi: 10.1252/jcej.7.417.

J.D. van der Waals. The thermodynamic theory of capillarity under the hypothesis of a continuous density variation. *English translation in J. Stat. Phys., 20, pp. 197–244 1979*, 1893.

Jeng-Renn Yang and Shwin-Chung Wong. An experimental and theoretical study of the effects of heat conduction through the support fiber on the evaporation of a droplet in a weakly convective flow. *International Journal of Heat and Mass Transfer*, 45(23):4589 – 4598, 2002. ISSN 0017-9310. doi: https://doi.org/10.1016/S0017-9310(02)00164-3. URL http://www.sciencedirect.com/science/article/pii/S0017931002001643.

Shichun Yang, Yanfei Gao, Yaoguang Cao, Yue Gu, and Zhuoran Gong. Investigation on deformation of an evaporating droplet in convective transcritical environments. *Advances in Mechanical Engineering*, 2014:1–12, 04 2014. doi: 10.1155/2014/326059.

Pengtao Yue, Chunfeng Zhou, James J. Feng, Carl F. Ollivier-Gooch, and Howard H. Hu. Phase-field simulations of interfacial dynamics in viscoelastic fluids using finite elements with adaptive meshing. *Journal of Computational Physics*, 219(1):47 – 67, 2006. ISSN 0021-9991. doi: https://doi.org/10.1016/j.jcp.2006.03.016. URL http://www.sciencedirect.com/science/article/pii/S0021999106001392.

Feichi Zhang, Henning Bonart, Thorsten Zirwes, Peter Habisreuther, Henning Bockhorn, and Nikolaos Zarzalis. *Direct Numerical Simulation of Chemically Reacting Flows with the Public Domain Code OpenFOAM*. 12 2015. doi: 10.1007/978-3-319-10810-0_16.

Hongtao Zhang, Vasudevan Raghavan, and George Gogos. Subcritical and supercritical droplet evaporation within a zero gravity environment; on the discrepancies between theoretical and experimental results. *International Journal of Spray and Combustion Dynamics*, 1(3):317–338, 2009. doi: 10.1260/175682709789141555. URL https://doi.org/10.1260/175682709789141555.

Julian Zips, Hagen Muller, and Michael Pfitzner. Efficient thermo-chemistry tabulation for non-premixed combustion at high-pressure conditions. *Flow Turbulence Combustion*, 2018. doi: https://doi.org/10.1007/s10494-018-9932-4.

A

Appendix

A.1. Thermal Conductivity using Excess entropy

This model rests on the pioneering work of Rosenfeld [1977], who postulated that the transport properties scale with the excess entropy. Excess entropy is given by,

$$S_{ex}(\rho, T) = S(\rho, T) - S_{id}(\rho, T) \tag{A.1}$$

It is to be noted that the excess entropy scaling is exact only when the potential energy is homogeneous, but it is very good approximate in other cases provided that species under does not have strong directional bonds. The following definition can encapsulate the excess entropy model, microscopic dynamics at the same state points with the same excess entropy are the same. Excess entropy scaling can be identified as a variant of isomorph theory, which states that state points 1 and 2 are said to be isomorphic if their reduced coordinates are the same. The next work on this topic was accomplished by Hopp and Gross [2017], where they worked on addressing the issue of failing of Rosenfeld's scaling, but it was noted that excess entropy could be regarded as a scaling factor provided an appropriate reference is used. They investigated different reference models, such as CE, CE, with the Eucken and LTST. Each model did better at the designed regime, e.g., CE did better in high-density regimes while vice versa was true for CE with Eucken and LTST. The authors utilized a correction term to provide a transition between different regimes. As for the reduced thermal conductivity, they used a third-order polynomial namely,

$$ln\Big(\frac{\lambda}{\lambda_{ref}}\Big) = A + Bs^* + C(1 - exp(s^*)) + D(s^*)^2 \tag{A.2}$$

A.2. Ideal thermal conductivity

As stated in the Chapter 8, ideal thermal conductivity model in COMSOL Multiphysics corresponds to the Stiel and Thodos thermal conductivity model. The individual thermal conductivities is computed from the correlation with reduced densities. It is important to note that the correction term ($\lambda_{v,P}$) is valid only till reduced density of 3.

$$\lambda_v = \sum_i x_i \lambda_{i,v} + \Delta\lambda_{v,P} \tag{A.3}$$

λ_v, x_i, $\lambda_{i,v}$ and $\lambda_{v,P}$ corresponds to the high- pressure thermal conductivity of the mixture, mole fraction, low-pressure and high pressure contributions respectively.

A.3. Firoozabadi Model for Diffusivity

Firoozabadi model is an empirical diffusion model based on the values of 889 experimental campaigns. A range of compounds from light to heavy gases, aromatic, polyaromatics, normal & branched alkanes was included in the database. The experimental data also included the self-diffusion coefficient and infinite binary diffusion. They utilized nonlinear least-squares minimization on the general functional form,

$$\frac{cD^{\infty}}{(cD)^0} = f\Big(\frac{\mu}{\mu^0}, T_r, P_r, \omega\Big) \tag{A.4}$$

The diffusion coefficient is computed from the following procedure,

1) Dilute gas diffusivity is computed using Fuller model
2) Density (mol/m^3) is computed using PR-EoS, viscosity (Pa.s) using Chung's model and as for the low-pressure viscosity Stiel and Thodos method is utilized
3) The diffusion at infinite dilution is computed
4) From the infinite dilution, the mixture diffusivity is computed from the Vignes equation

$$\text{Vignes equation, } D_{12} = (D_{12}^{\infty})^{x2}(D_{21}^{\infty})^{x1} \tag{A.5}$$

$$\frac{(cD)^{\infty}}{(cD)^{0}} = A0\Big(\frac{T_{r1}P_{r2}}{T_{r2}P_{r1}}\Big)^{A1}\Big(\frac{\mu}{\mu_0}\Big)^{(A2+A3)} \tag{A.6}$$

$$A0 = e^{a_1} \tag{A.7}$$

$$A1 = 10a_2$$

$$A2 = a_3(1 - 10\omega_1 - \omega_2 + 10\omega_1\omega_2)$$

$$A3 = a_4(P_{r1}^{3a_5} - 6P_{r2}^{a5} + 6T_{r1}^{10a_6}) + a_7T_{r2}^{-a6} + a_2(\frac{T_{r1}P_{r2}}{T_{r2}P_{r1}})$$

where the coefficients a_1, a_2, a_3, a_4, a_5, a_6, and a_7 are -0.0471, 0.0103, -0.0147, -0.0053, -0.3370, -0.1852, and -0.1914 respectively.

A.4. Prandtl number model for thermal conductivity for n-Dodecane

The Prandtl number correlation based on Fourier expression for PR-EoS for various pressure conditions as,

Pressure	6.2 MPa	8.8 MPa	10.6 MPa
a0	7.069	8.828	9.546
a1	7.551	10.26	11.55
b1	5	4.832	4.24
a2	3.335	5.275	6.233
b2	3.084	2.65	1.963
a3	1.806	2.787	3.264
b3	1.764	1.343	0.7713
a4	0.5996	0.9842	1.155
b4	0.7489	0.4817	0.2045
a5	0.1811	0.2576	0.2825
a5	0.2141	0.1141	0.02471
w	0.004065	0.004062	0.00395

Table A.1: Curve fit for Prandtl number using Chung's method

$$\begin{aligned} Pr = {} & a0 + a1 \times cos(w \times T) + a2 \times cos(2w \times T) + a3 \times cos(3w \times T) + a4 \times cos(4w \times T) + a5 \times cos(5w \times T) \\ & + b1 \times sin(w \times T) + b2 \times sin(2w \times T) + b3 \times sin(3w \times T) + b4 \times sin(4w \times T) + b5 \times sin(5w \times T) \end{aligned} \tag{A.8}$$

where T is the temperature.

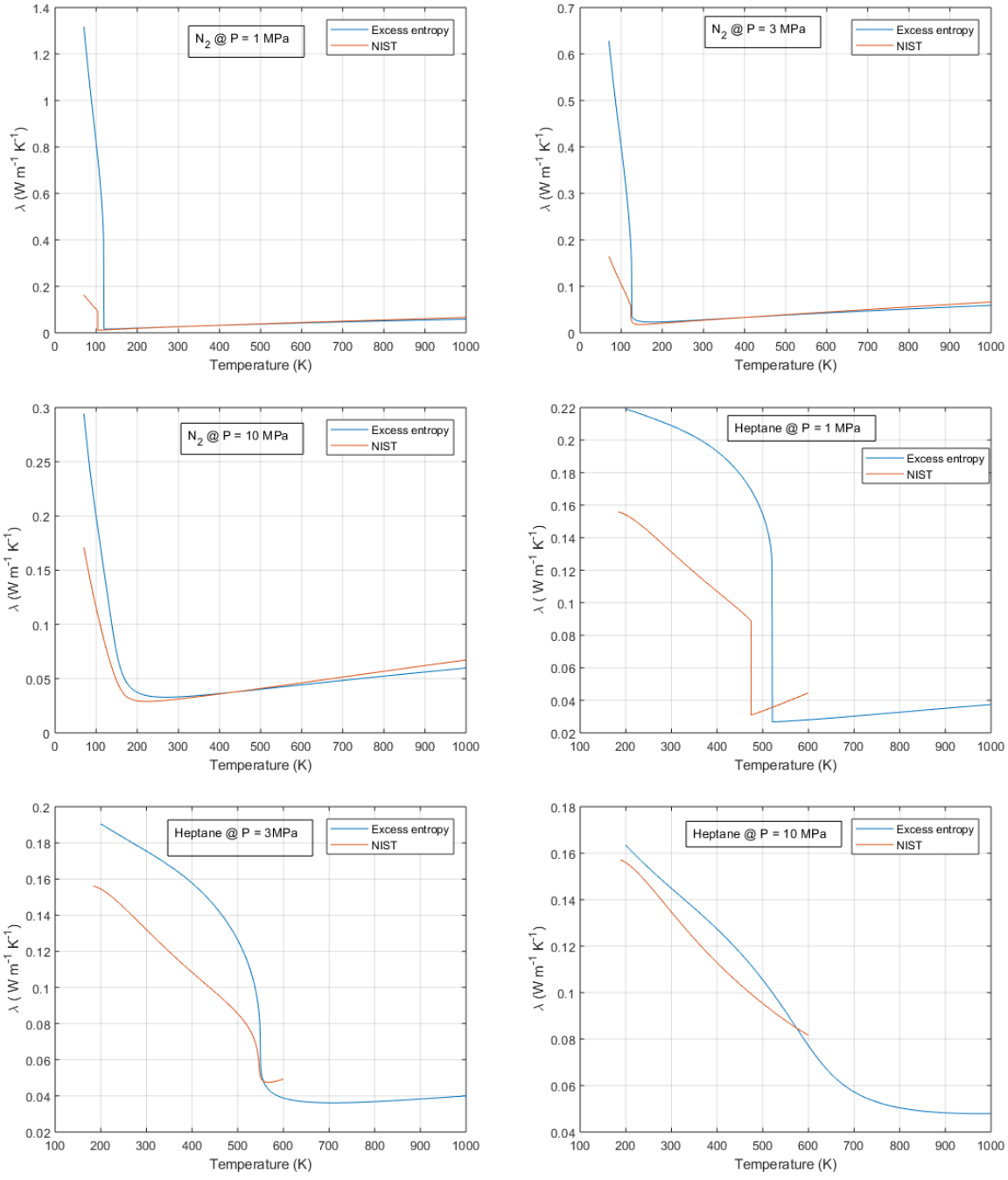

Figure A.1: Thermal conductivity of Heptane in various conditions

A.5. Mass fraction plots for 0-D and 1-D models

The mass fraction at the droplet interface for the 0-D model for Sanchez's test case is given by the figure A.2. The VLE is computed for all the EoS in MATLAB.

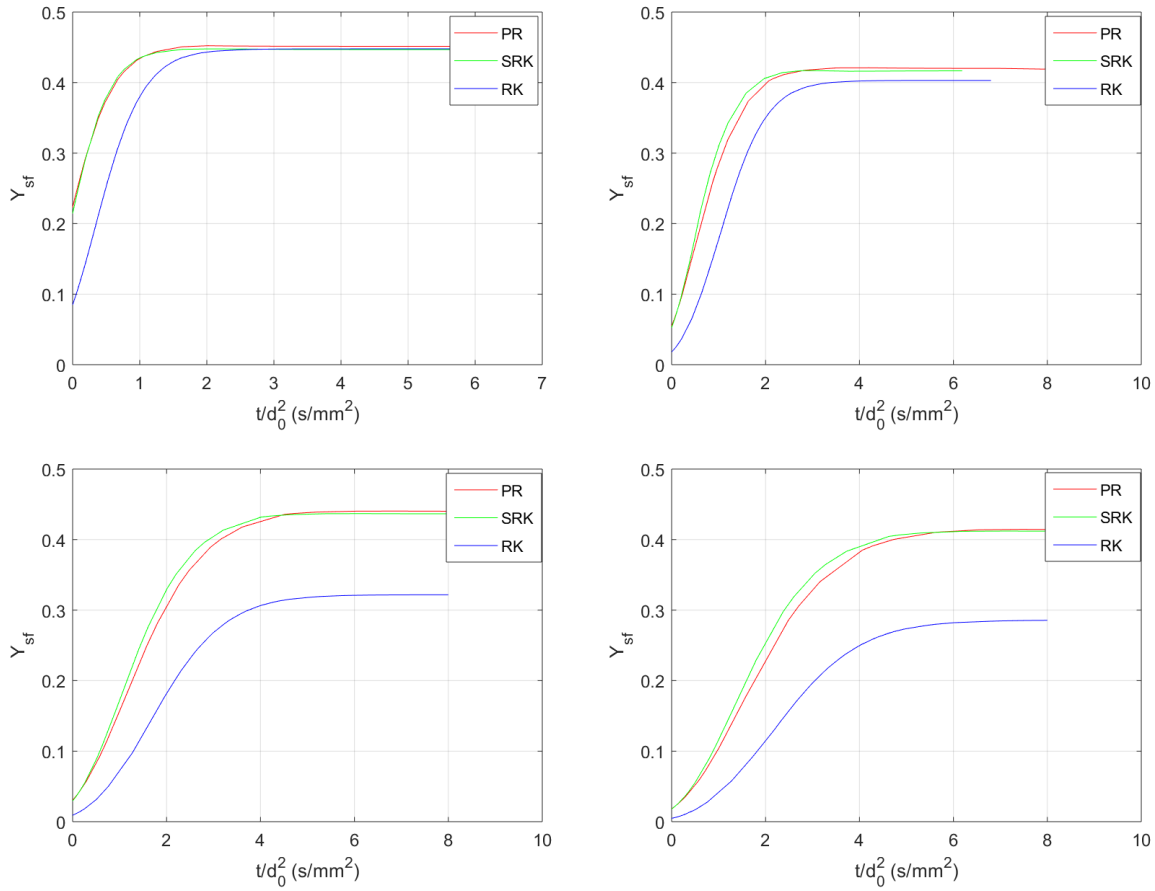

Figure A.2: Top-left: Mass fraction at the surface of the droplet for the Sanchez's test case at 1 bar; Top-right: Mass fraction at the surface of the droplet for the Sanchez's test case at 5 bar; Bottom-left: Mass fraction at the surface of the droplet for the Sanchez's test case at 10 bar; Bottom-right: Mass fraction at the surface of the droplet for the Sanchez's test case at 20 bar

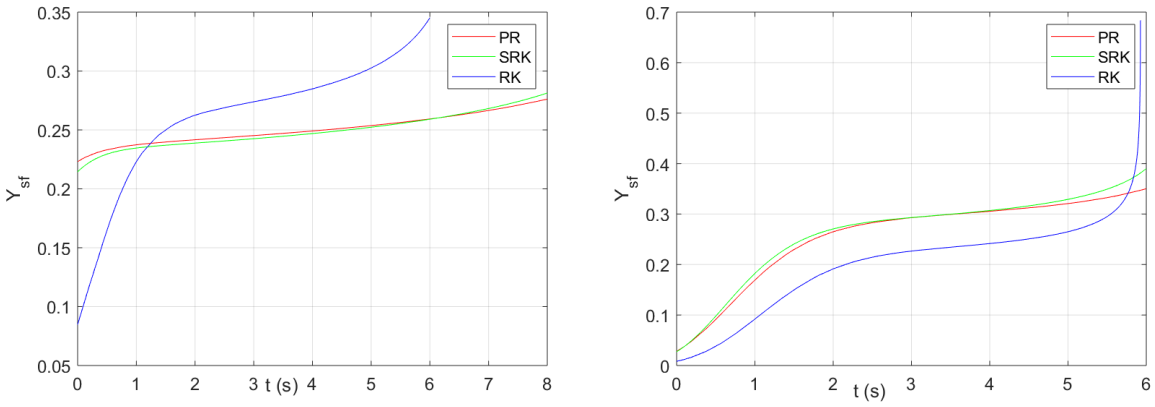

Figure A.3: Left: Mass fraction at the surface of the droplet for the Kadota's test case at 0.1 MPa; Right: Mass fraction at the surface of the droplet for the Kadota's test case at 1.1 MPa

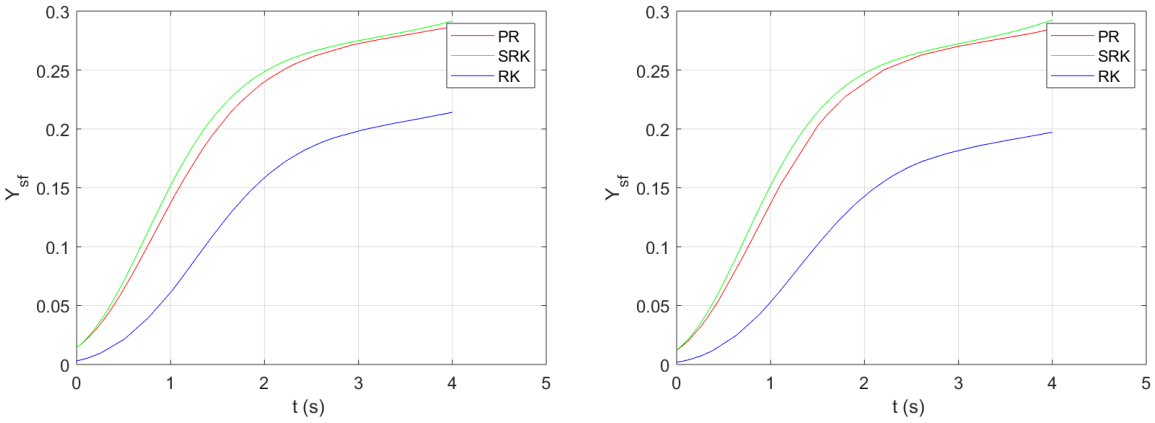

Figure A.4: Left: Mass fraction at the surface of the droplet for the Kadota's test case at 3.1 MPa; Right: Mass fraction at the surface of the droplet for the Kadota's test case at 5.1 MPa

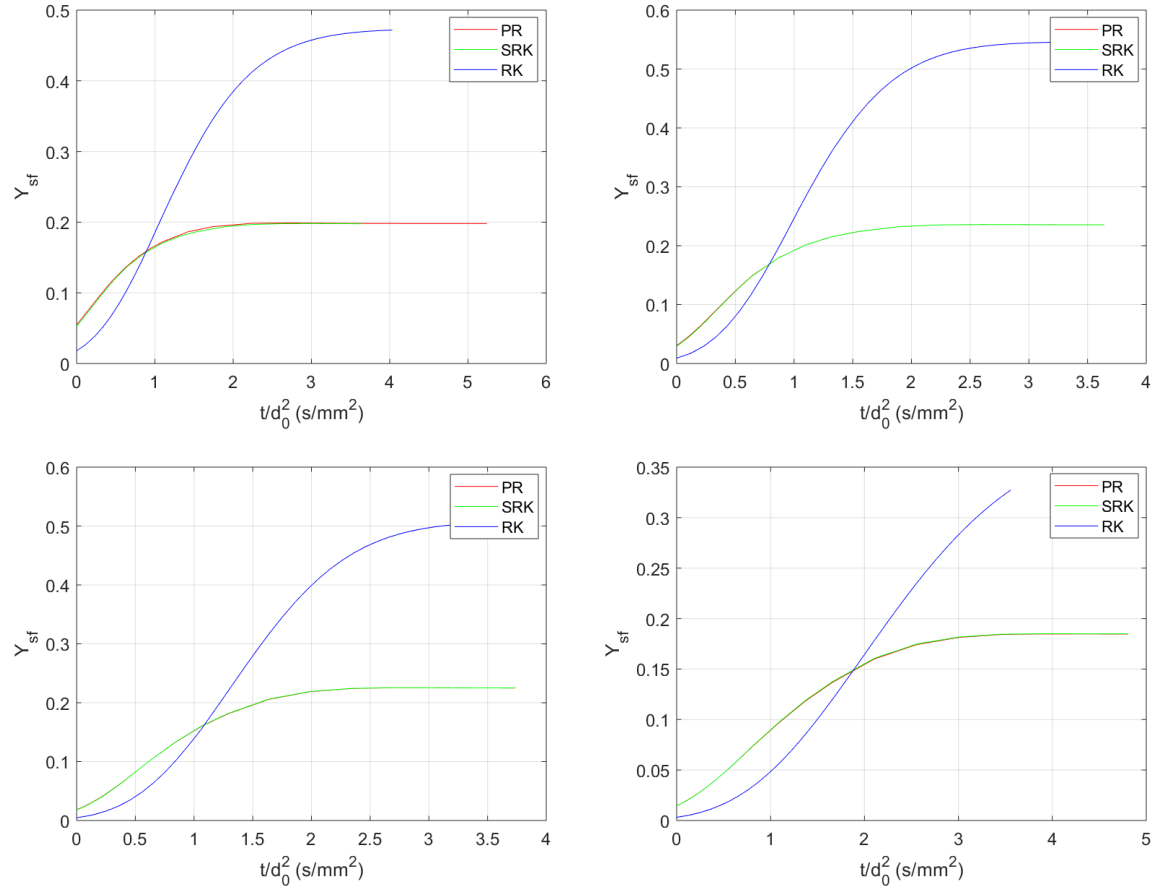

Figure A.5: Top-left: Mass fraction at the surface of the droplet for the Subashki's test case at 5 atm; Top-right: Mass fraction at the surface of the droplet for the Subashki's test case at 10 atm; Bottom-left: Mass fraction at the surface of the droplet for the Subashki's test case at 20 atm; Bottom-right: Mass fraction at the surface of the droplet for the Subashki's test case at 30 atm

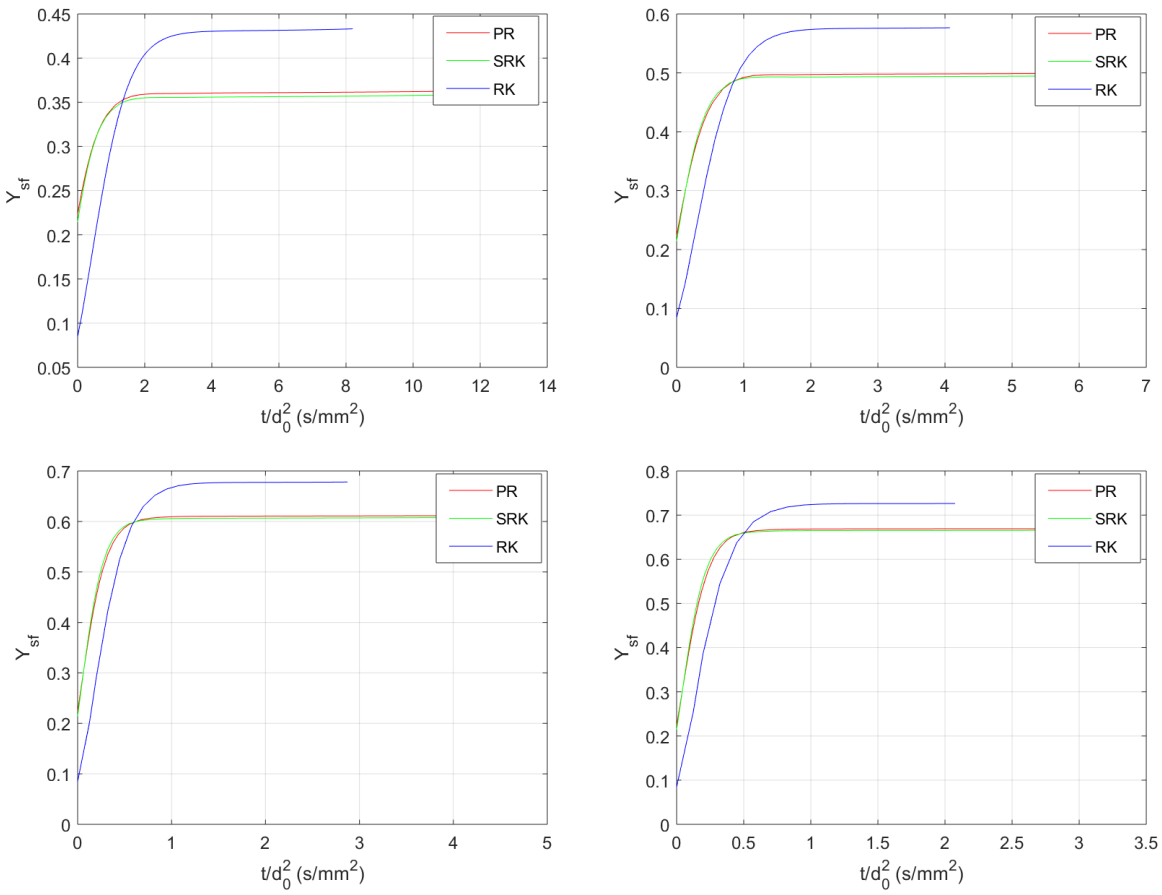

Figure A.6: Top-left: Mass fraction at the surface of the droplet for the Ebrahimian's test case at 473 K; Top-right: Mass fraction at the surface of the droplet for the Ebrahimian's test case at 623 K; Bottom-left: Mass fraction at the surface of the droplet for the Ebrahimian's test case at 823 K; Bottom-right: Mass fraction at the surface of the droplet for the Ebrahimian's test case at 973 K

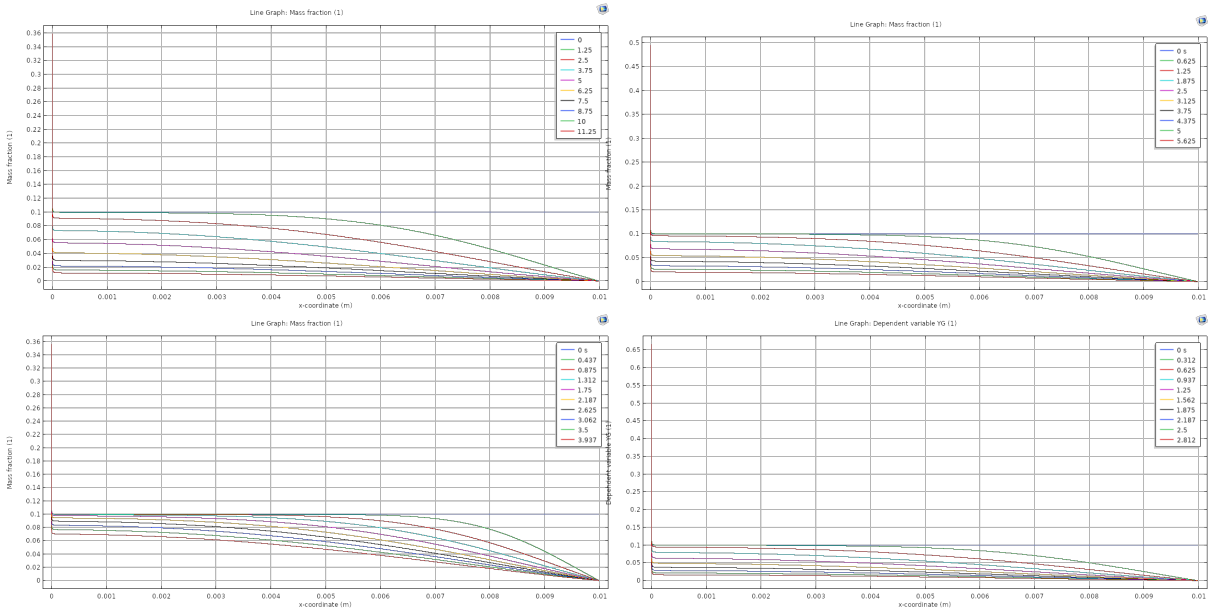

Figure A.7: Top-left: Mass fraction profile of the gaseous part at 473 K of Ebrahimian's test case; Top-right: Mass fraction profile of the gaseous part at 623 K of Ebrahimian's test case; Bottom-left: Mass fraction profile of the gaseous part at 823 K of Ebrahimian's test case; Bottom-right: Mass fraction profile of the gaseous part at 973 K of Ebrahimian's test case

Figure A.6 and A.7 shows the mass fraction at the droplet surface and gaseous part of the fuel for the Ebrahimian's test case.

A.6. 0D models

Various quantities for the 0-D model were plotted for different equation of states for the Case-4 (20 bar) of Sanchez's test case.

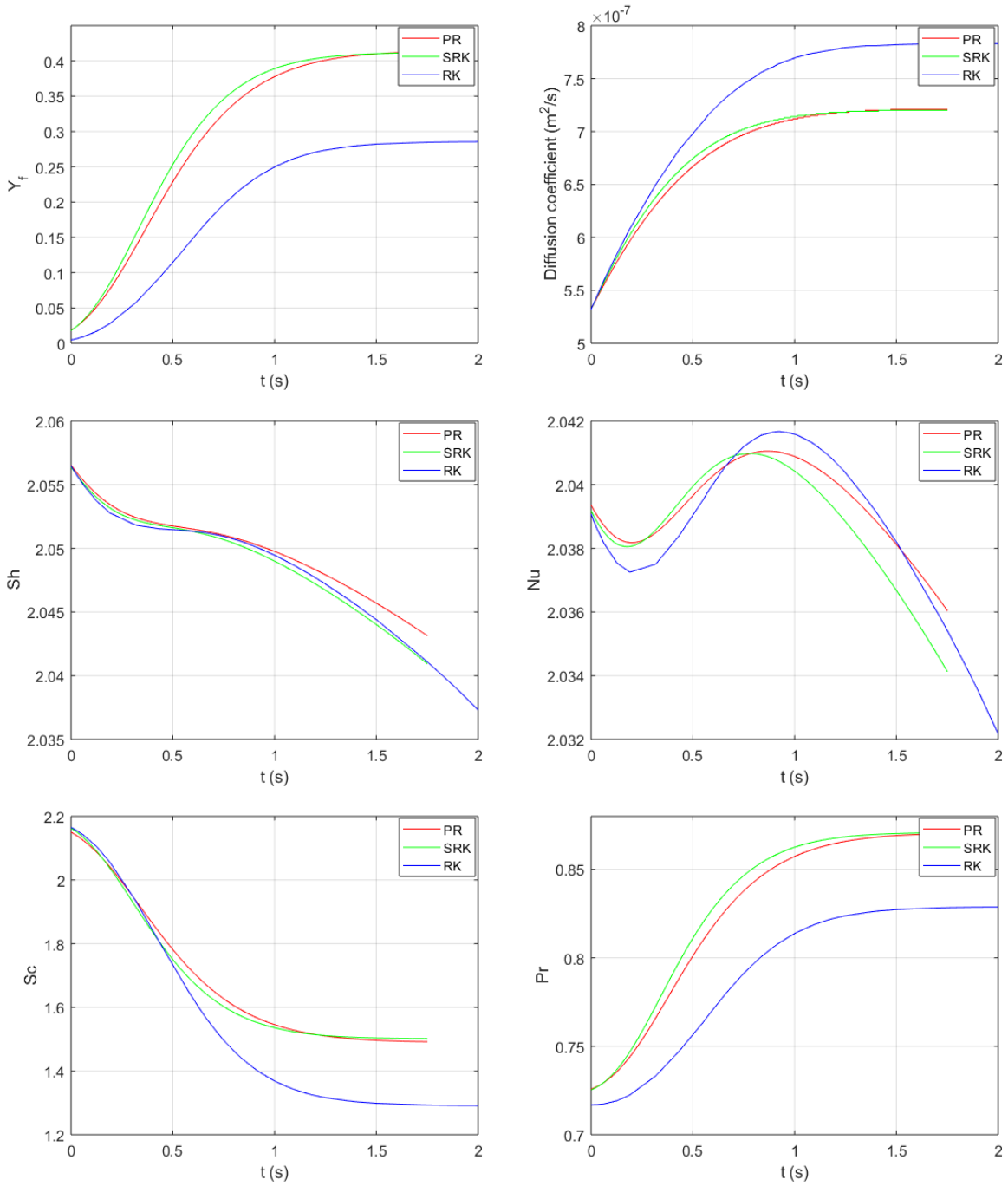

Figure A.8: Top-left: Mass fraction n-heptane at the surface; Top-right: Diffusion coefficient of n-heptane in nitrogen; Middle-left: Sherwood number; Middle-right: Nusselt number; Bottom-left: Schmidt number; Bottom-right: Prandtl number; Sanchez's test case-4

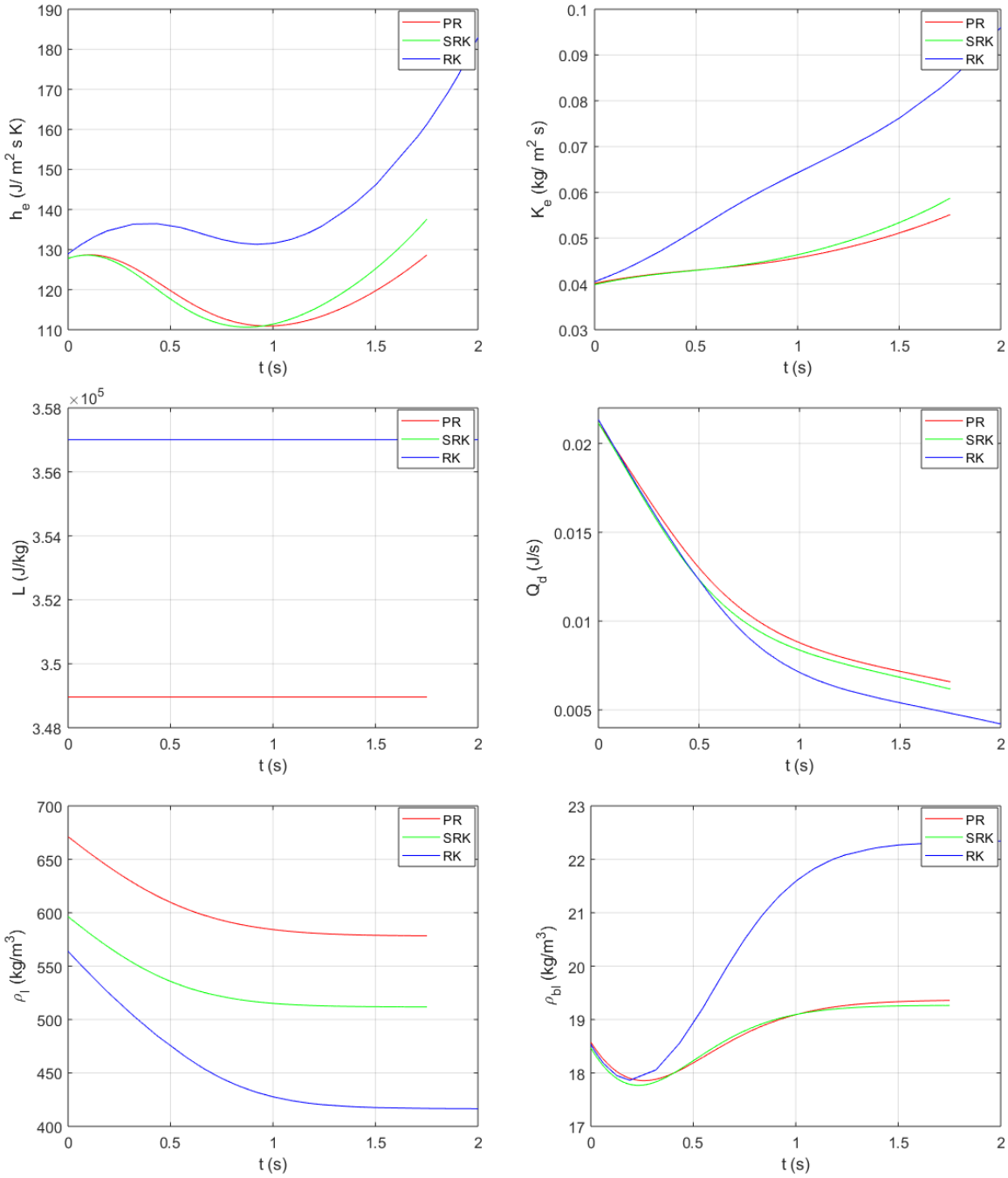

Figure A.9: Top-left: Heat transfer coefficient; Top-right: Mass transfer coefficient; Middle-left: Latent heat of vaporization; Middle-right: Heat transfer rate; Bottom-left: Density of the liquid n-heptane; Bottom-right: Density of the vapor at the boundary layer; Sanchez's test case-4

A.7. 1D

Various quantities for the 1-D model were plotted for different equation of states for the Case-4 (973 K) of Ebrahimian's test case.

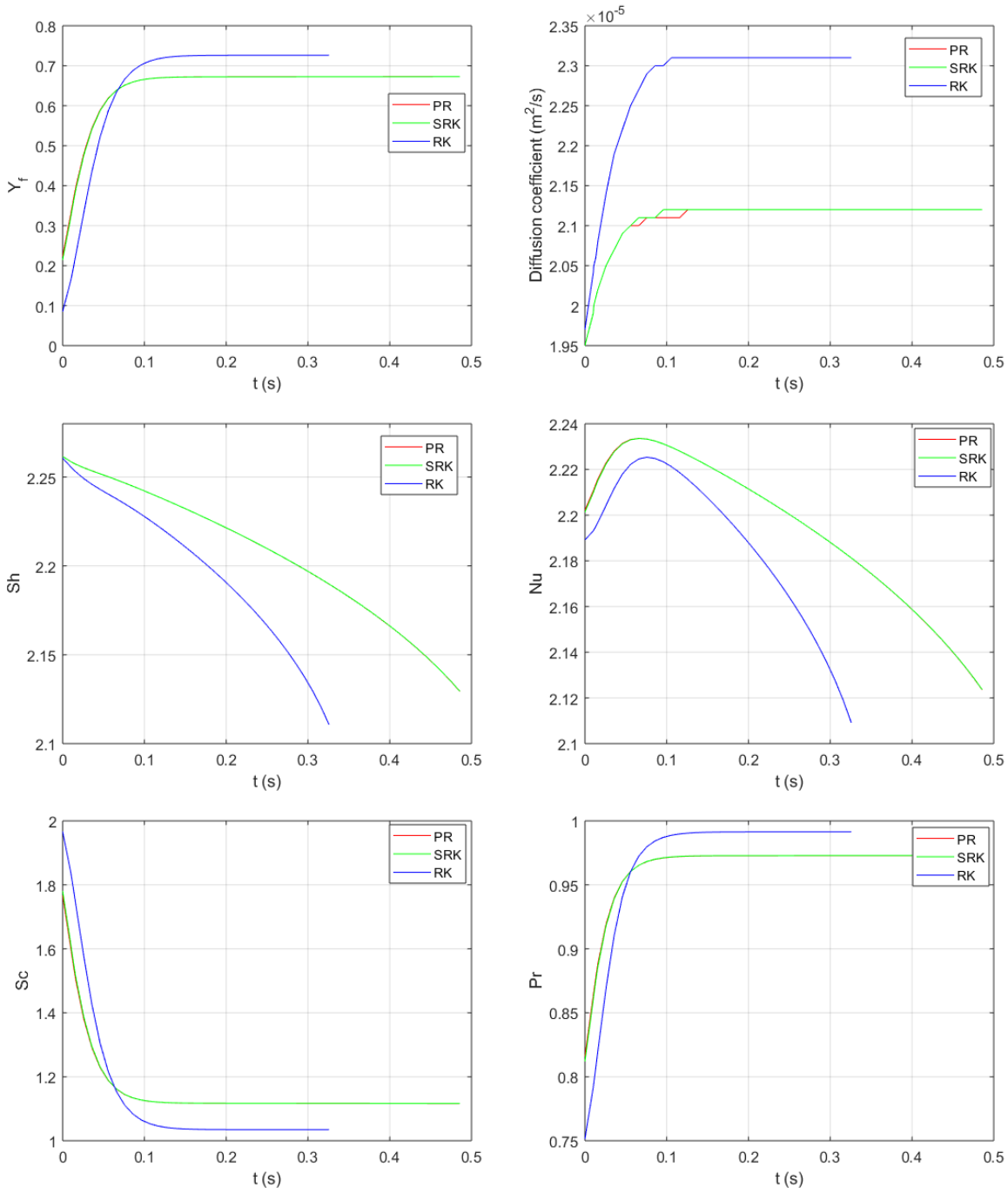

Figure A.10: Top-left: Mass fraction of n-heptane at the surface of the droplet; Top-right: Diffusion coefficient of n-heptane in nitrogen; Middle-left: Sherwood number; Middle-right: Nusselt number; Bottom-left: Schmidt number; Bottom-right: Prandtl number; Ebrahimian's test case-4

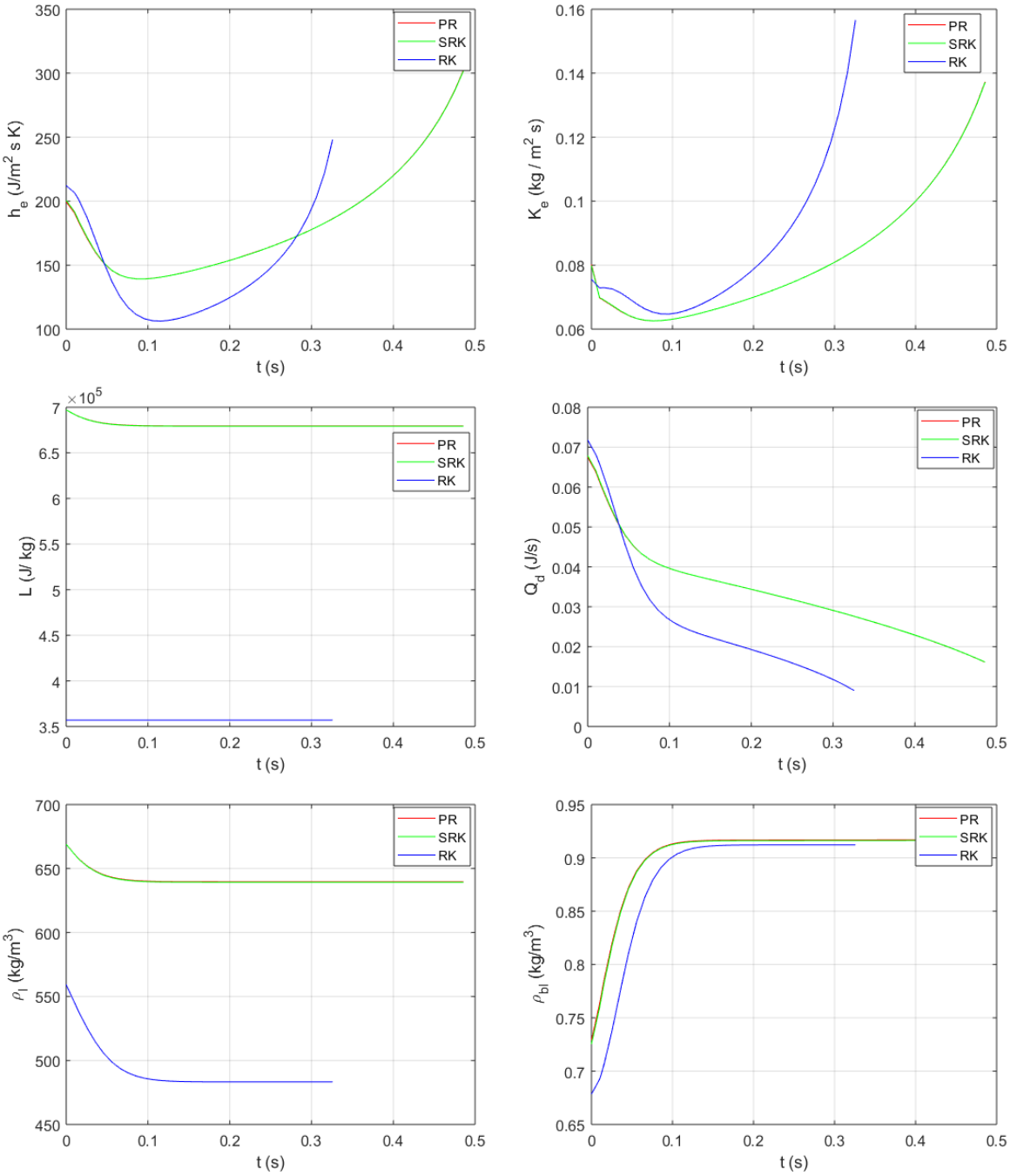

Figure A.11: Top-left: Heat transfer coefficient; Top-right: Mass transfer coefficient; Middle-left: Latent heat of vaporization; Middle-right: Heat transfer rate; Bottom-left: Density of liquid n-heptane; Bottom-right: Density of vapor at the boundary layer; Ebrahimian's test case-4

A.8. Gogos correction

There is an interesting study by Zhang et al. [2009] (Figure: A.12). They investigated the sources of discrepancies between the experimental data between Nomura and Yang. They pointed out the previously stated reasons of conduction between the fiber and the droplet and also attributed the initial movement of the droplet from the generator to the chamber. The authors employed an average velocity to model this phenomenon and found that the average velocity models correlate well with the experimental data of Nomura. The results from the Gogos model used here is a full axisymmetric model without the correction for the velocity.

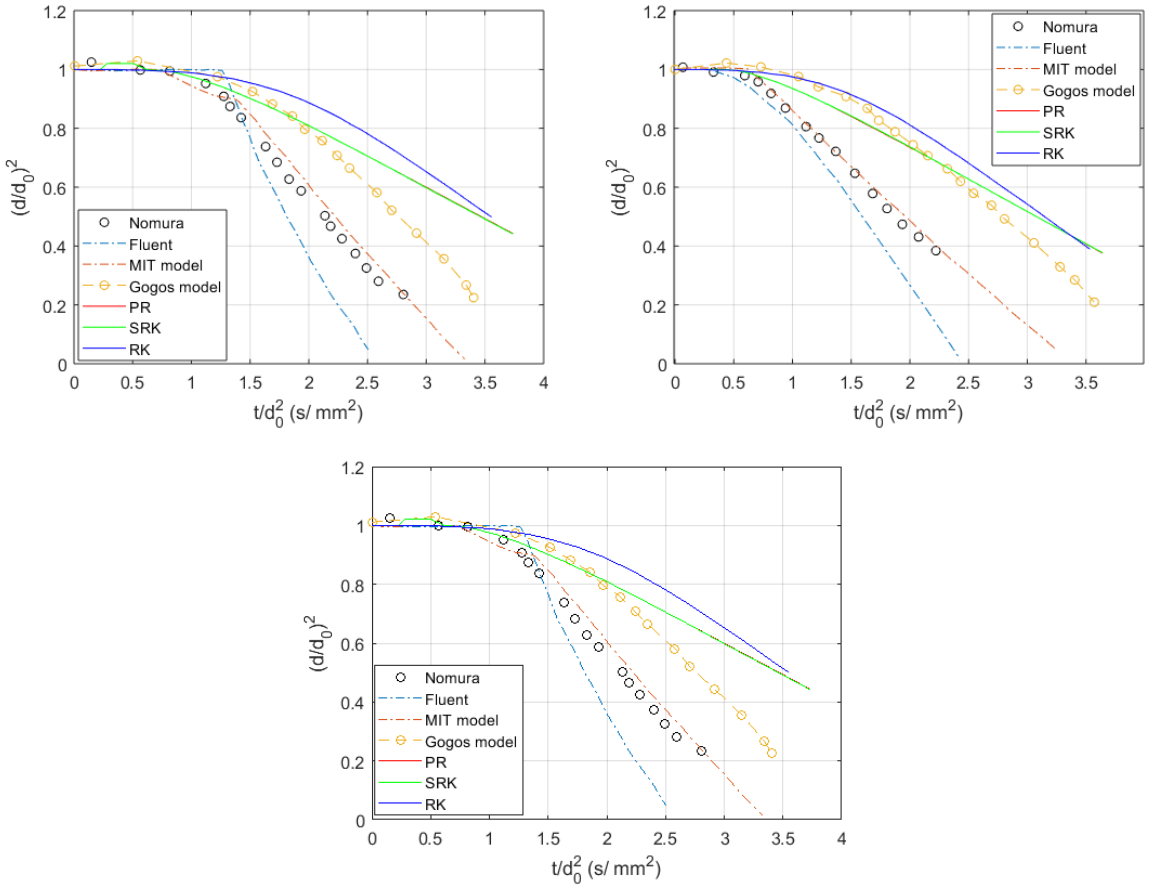

Figure A.12: Top-left: Comparisons of different evaporation modules of n-heptane in nitrogen at 5 atm and 556 K; Top-right: Comparisons of different evaporation modules of n-heptane in nitrogen at 10 atm and 669 K; Bottom: Comparisons of different evaporation modules of n-heptane in nitrogen at 20 atm and 656 K

A.9. Time Step Selection

Time-stepping is an important issue to be studied in COMSOL as it deviates from conventional solvers. In COMSOL, there are four classes of time-stepping,

- Free
- Strict
- Intermediate
- Manual

In the free setting, the solver is free to choose the timesteps for which the modeled. Consecutively, the required solution is obtained from interpolation of the computed solutions. In the strict setting, the solver is forced to solve for the requested timestep but it does have the option to introduce additional timesteps as to respect the tolerance settings. In the intermediate setting, the solver can choose one additional timestep between the requested timesteps. All the above choose the timesteps depending on the timestepping solver error but the last setting, the manual one disables the timestepping error option and solves the model at requested timesteps.

The BDF in this study has a variable order ranging from 1 to 5. For first few timesteps, the step size is doubled and order is raised from 1 to 5 until the local error test is failed and if the local error test fails again then the stepsize is reduced. If the timestep of constant order q has passed the local error test for q+1 steps then the BDF considers increasing the order.

A.10. Modules in COMSOL Multiphysics

The screenshot of the laminar flow, heat transfer and transport of concentrated species module used in this study. The mass fractions 1,2,3 and so on in figure A.14 are used to enforce the equality of fugacity. The highlighted part in figure A.14 corresponds to droplet. The figure A.15 shows the weak contribution setting used for the phase-field module in this study.

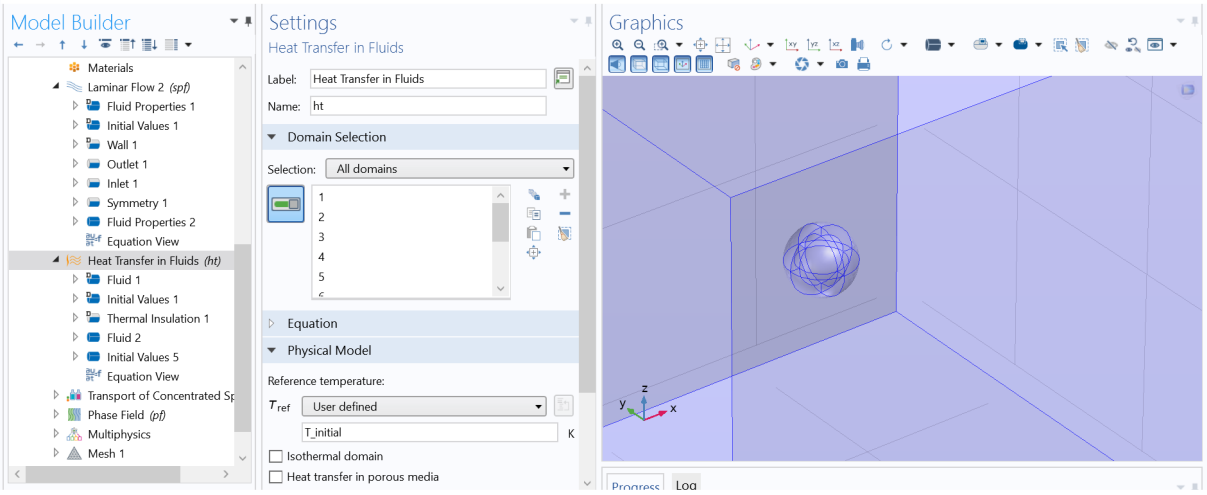

Figure A.13: Laminar flow and heat transfer in fluids in COMSOL Multiphysics

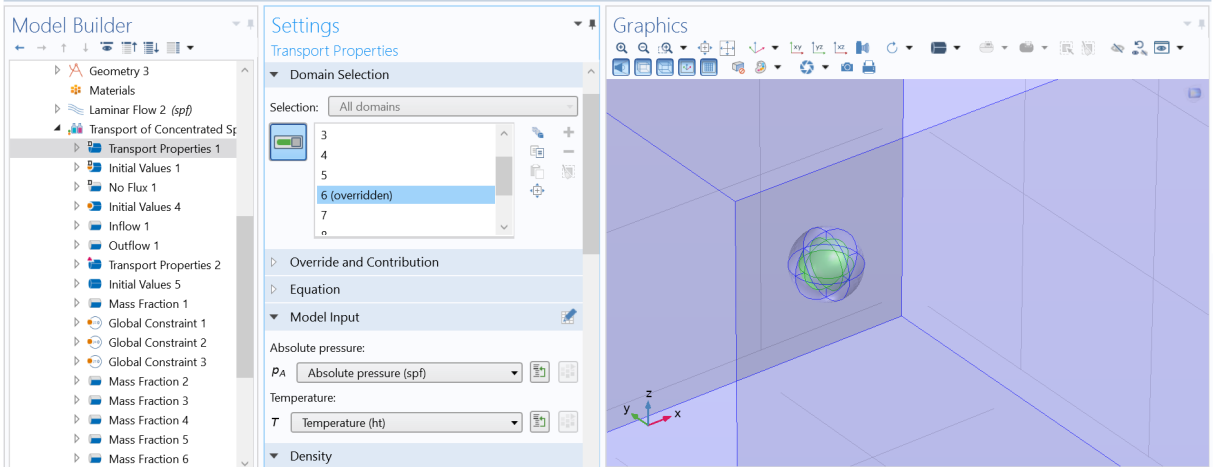

Figure A.14: Transport of concentrated species module in COMSOL Multiphysics

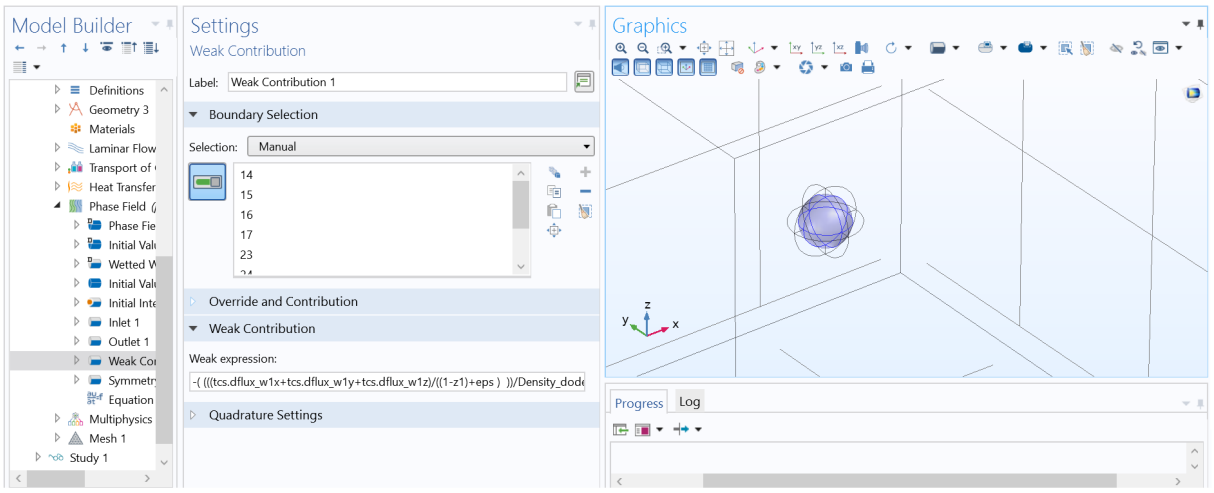

Figure A.15: Phase-field module in COMSOL Multiphysics

A.11. Mass fraction plots for the 3-D model

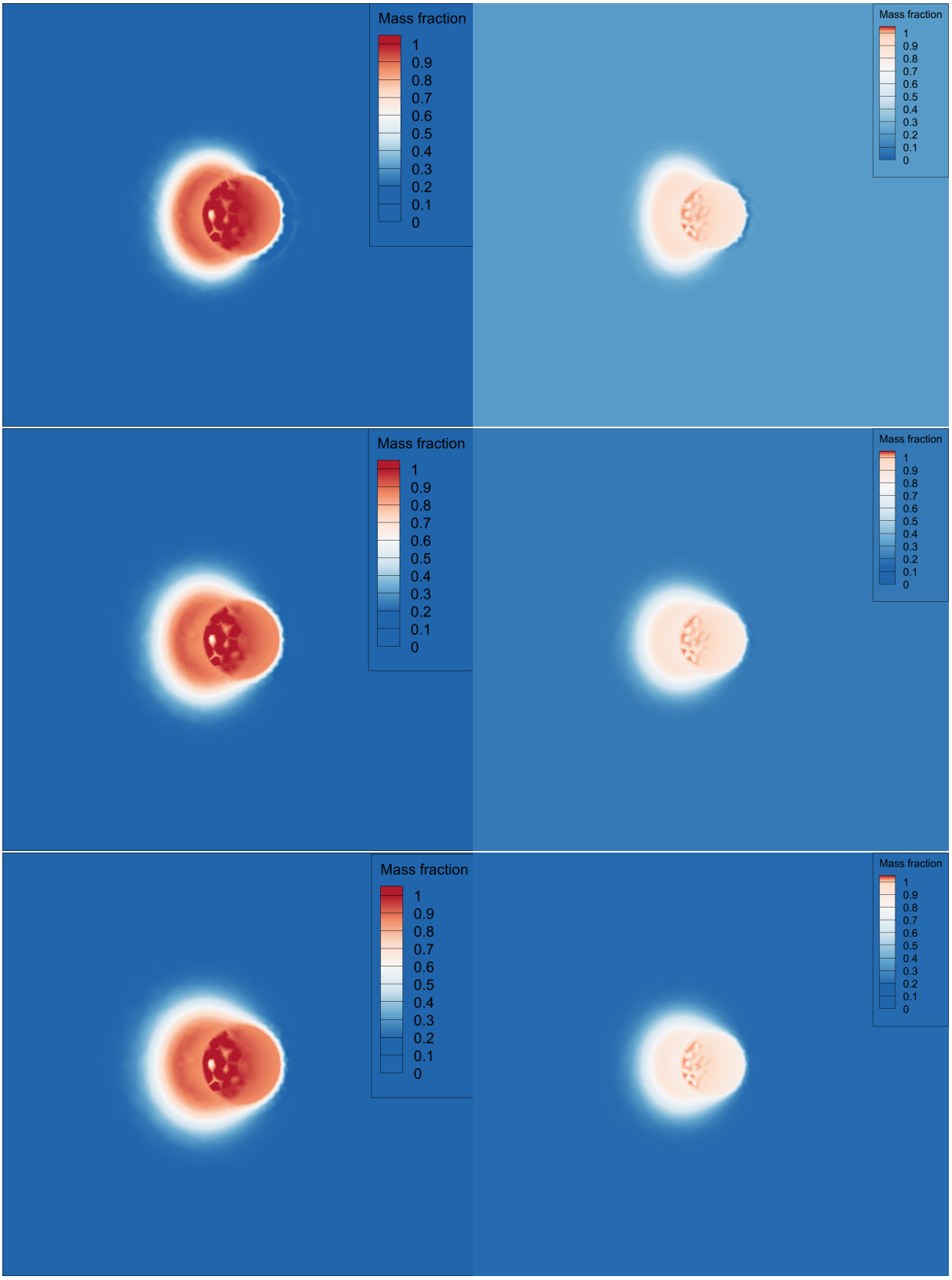

Figure A.16: Distribution of mass fraction for level set (left) and phase-field model (right) from case 1 to case 3 (top to bottom) at t = 0.1 ms

A.12. Effects of mesh size on phase-field quantities

The figures A.17 and A.18 corresponds to the plots of a generic 2-D phase-field model at various mesh resolution. The former corresponds to the fine mesh only in the droplet region whereas the the latter one represents fine mesh even on the ambient region. The phase-field variable is too dispersed in the former while forming a confined shape in the latter. Hence, in contrast to the conventional thinking that the interfacial modeling in PFM not only depends on the fine mesh in the interface but rather on the whole field.

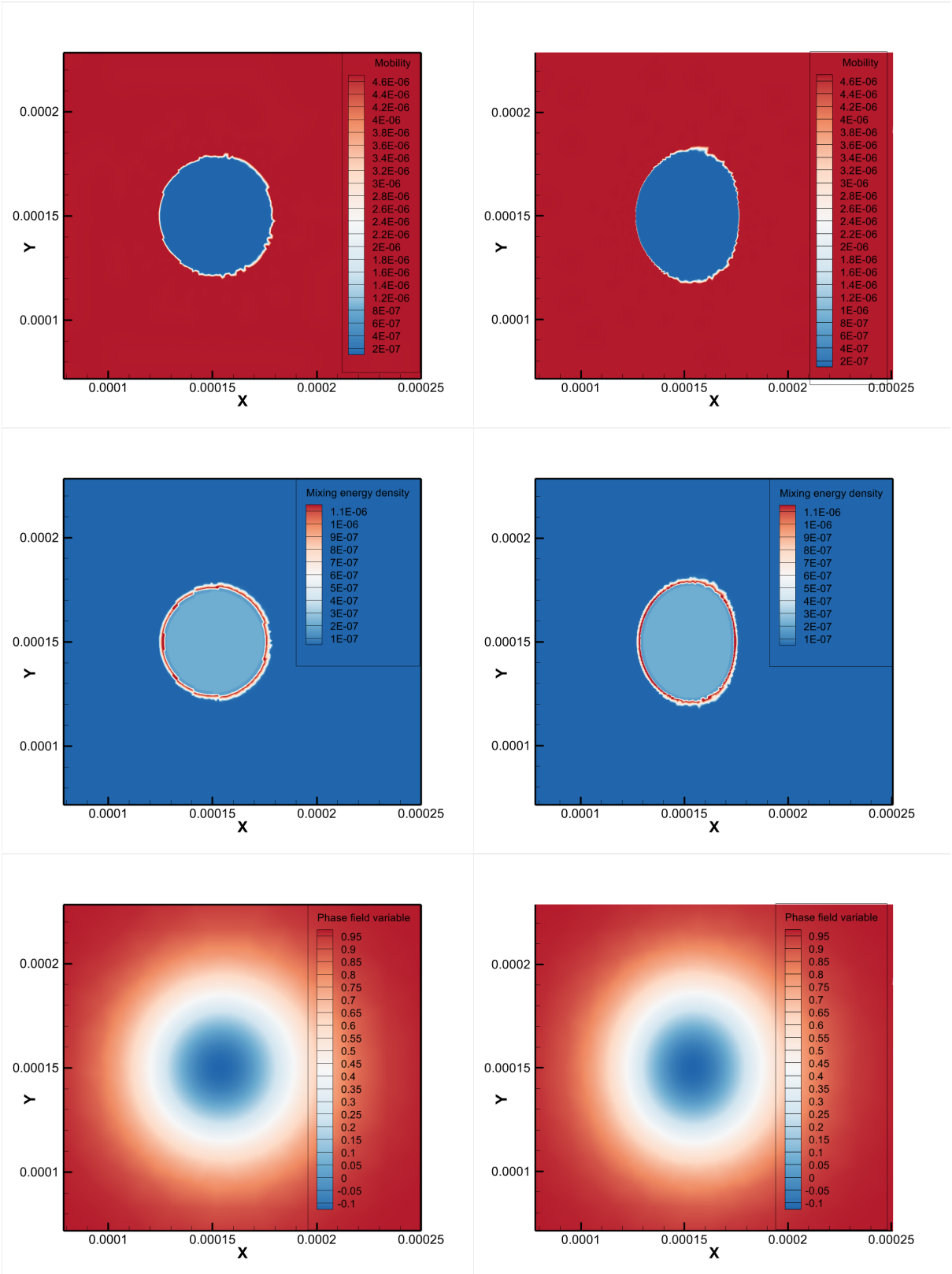

Figure A.17: Left: The plots of various phase-field quantities with maximum size in the droplet domain set at 1e-6 m; Right: The plots of various phase-field quantities with maximum size in the droplet domain set at 3e-7 m

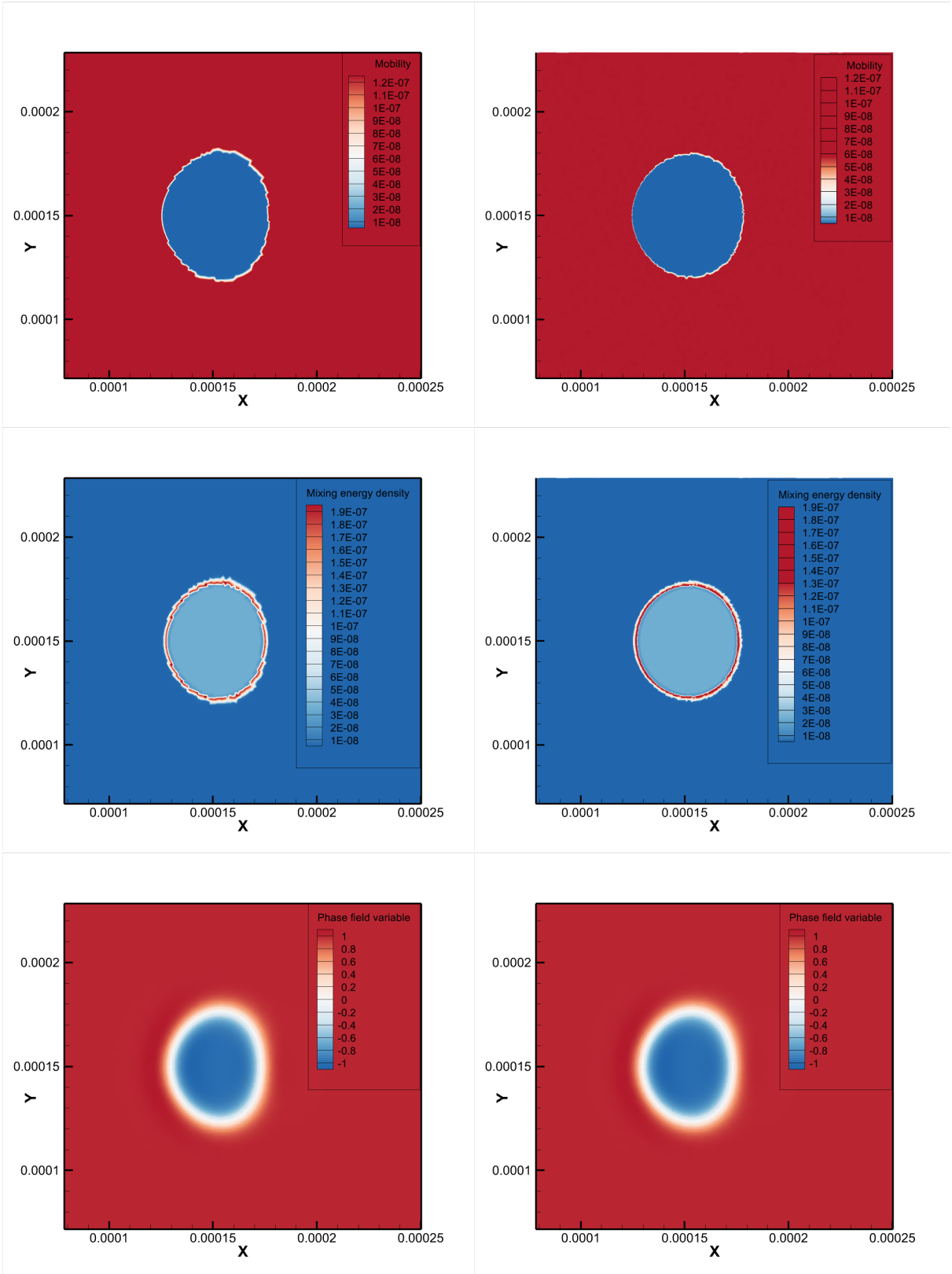

Figure A.18: Left: The plots of various phase-field quantities with maximum size in the ambient field set at 3e-6 m; Right: The plots of various phase-field quantities with maximum size in the ambient field set at 2.01e-6 m; with mesh size in the droplet corresponding to the above plots respectively

A.13. LSM vs PFM

The figure A.19 illustrates the effects of non-local effects against a LSM with the same mesh resolution. The fluxes doesn't to vary much against each other. Although, the shape of the droplet varies. It would be interesting to study the droplet at various temperatures along with a proper surface tension module for both PFM and LSM.

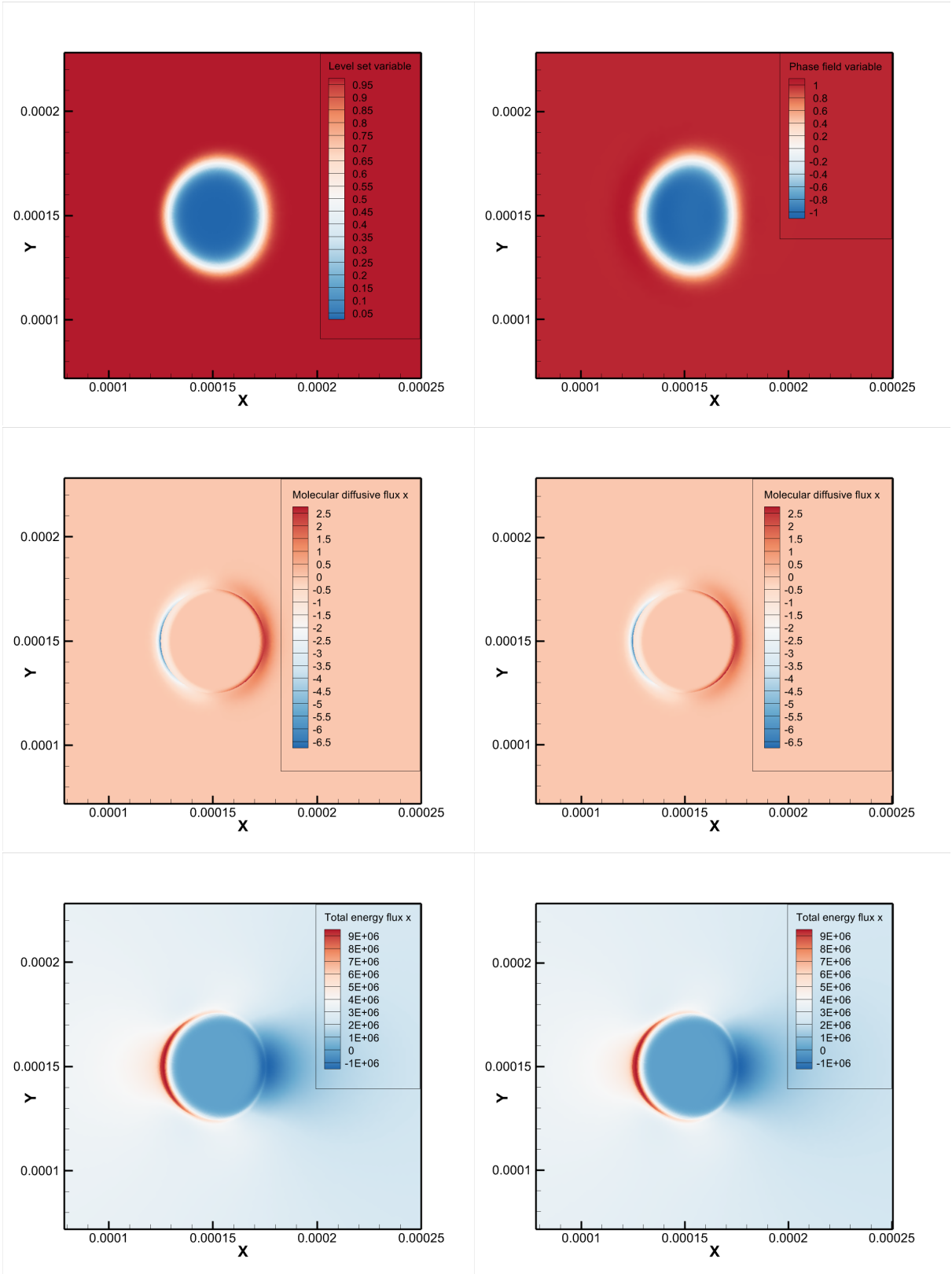

Figure A.19: Left: The plots of various interfacial quantities in level set(left) and phase-field (right) with the mesh specifications set at 3e-7 m in the ambient region and at 2.01e-6 m in the droplet region